POLITECNICO
MILANO 1863

SCUOLA DI INGEGNERIA INDUSTRIALE
E DELL'INFORMAZIONE

Analysis of disposal manoeuvres design in the Laplace plane for Highly Elliptical Orbits

Tesi di Laurea Magistrale in
Space Engineering

Author: **André Luis Dos Santos Hengemuhle**

Student ID: 939723
Advisor: Camilla Colombo
Co-advisors: Xiaodong Lu
Academic Year: 2022-23

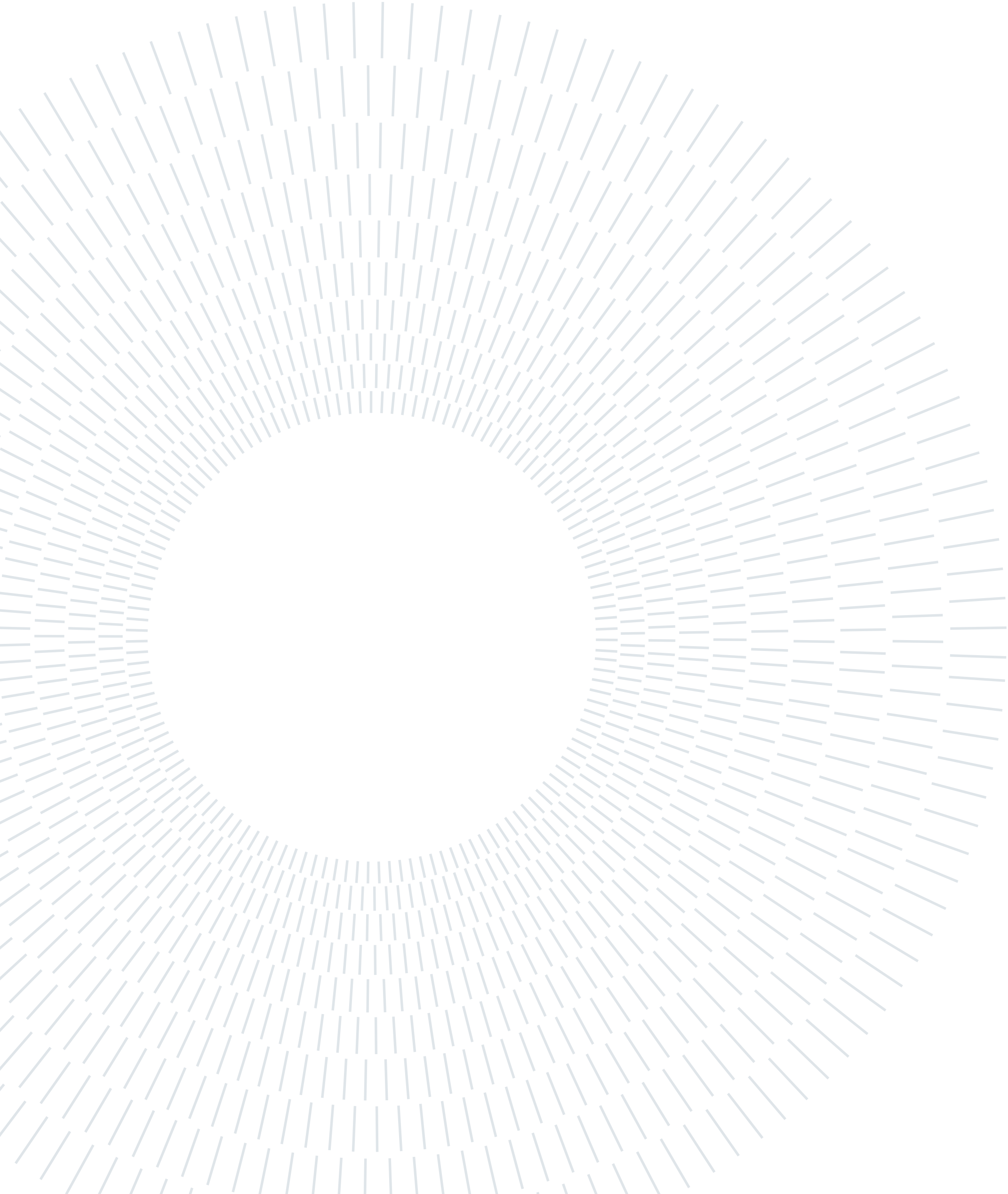

Copyright© December 2023 by André Luis Dos Santos Hengemuhle. All rights reserved. This content is original, written by the Author, André Luis Dos Santos Hengemuhle. All the non-originals information, taken from previous works, are specified and recorded in the Bibliography.

When referring to this work, full bibliographic details must be given, i.e. André Luis Dos Santos Hengemuhle, “Analysis of disposal manoeuvres design in the Laplace plane for Highly Elliptical Orbits”. 2023, Politecnico di Milano, Faculty of Industrial Engineering, Department of Aerospace Science and Technologies, Master in Space Engineering, Supervisor: Camilla Colombo, Co-supervisor: Xiaodong Lu Printed in Italy

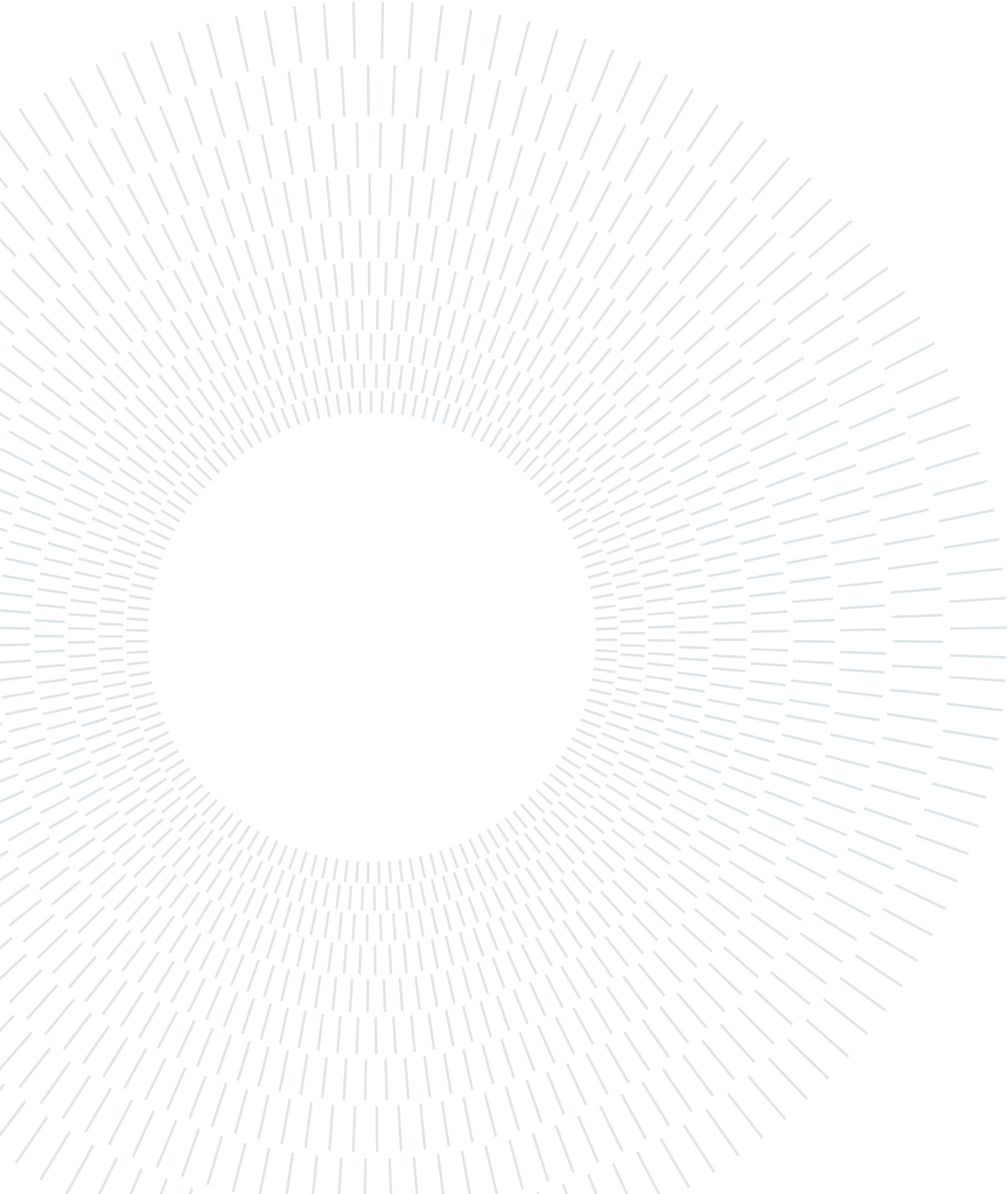

A Claudia

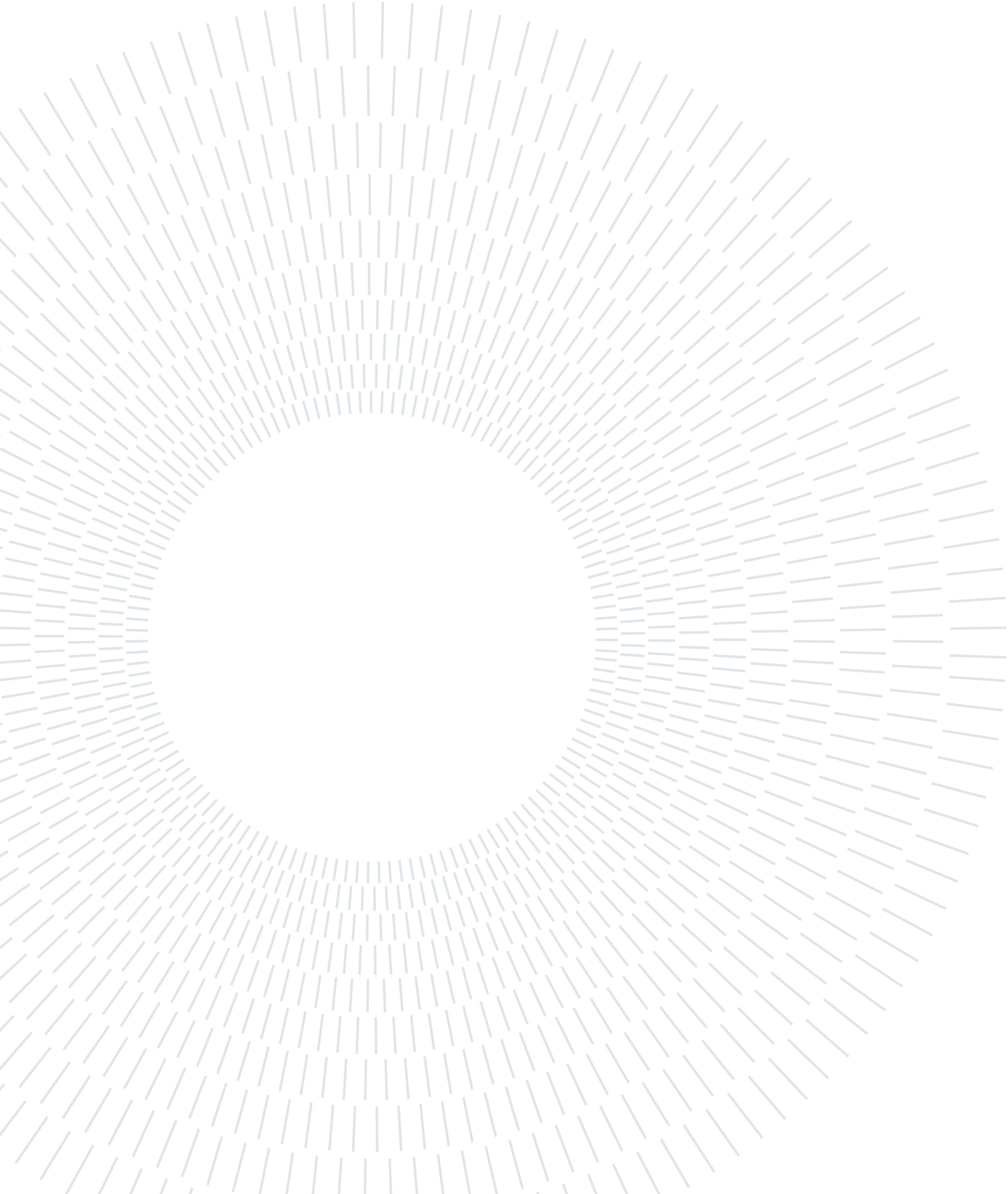

Abstract

In the last years, the problem of space debris has assumed great relevance and strict guidelines were identified to stop the process and try to revert it. Two possible end-of-life strategies are identified: the satellite re-entry into the atmosphere to cause its disruption; and the transfer to a graveyard orbit. This thesis tackles the problem of the manoeuvre optimisation strategy for the re-entry of a Highly Elliptical Orbit (HEO) Satellite.

In this thesis, the dynamics of the satellite are studied with a Triple-Averaged (TA) model obtained by averaging over the fast angles and the node, describing the dynamics dependent only on a single orbital element and the time t, due to the variation of third-bodies' ephemerides. The TA perturbation potentials accounted to accurately describe the orbital evolution are the zonal J_2 effect due to Earth's oblateness and the third-body gravitational attraction of both the Sun and the Moon. The validity of the TA model is analysed by comparison with the high-fidelity long-term evolution described by the Double-Averaged (DA) model, working in particular with the Laplace frame, whose formulation is here presented in several case scenarios, due to its variation in time caused by the oscillation of the Moon's orbital elements.

Then, disposal strategies exploiting the low computational costs are analysed, searching for a method that allows the onboard processor to plan disposal actions autonomously. In particular, a strategy that exploits both the triple-averaged dynamics and the phase space formulation with time-varying third-body orbital elements is proposed, dropping the assumption of constant Hamiltonian but still operating within a simplified analytic environment. This method is capable of adjusting the manoeuvres design within the TA propagation to tackle the added time dependence with respect to simplified cases where the ephemerides variations are simply neglected. Moreover, a hybrid approach is proposed in this thesis, trying to combine the positive aspects of both the semi-analytical and analytical methods, applying part of the phase space exploitation strategy inside a non-simplified framework. Those methods are compared to the global optimisation to assess their accuracy.

This thesis was part of the COMPASS project: "Control for orbit manoeuvring by surfing through orbit perturbations" (Grant agreement No 679086). This project is European

Research Council (ERC) funded project under the European Union's Horizon 2020 research.

Keywords: Orbital perturbations; Long-term Evolution; End-of-life disposal; Optimal manoeuvres

Abstract in lingua italiana

Negli ultimi anni, il problema dei detriti spaziali ha assunto grande rilevanza e sono state identificate linee guida rigorose per fermare il processo e cercare di invertirlo. Sono identificate due possibili strategie di fine vita: il rientro del satellite nell'atmosfera per causarne la distruzione; e il trasferimento in un'orbita cimitero. Questa tesi affronta il problema dell'ottimizzazione della strategia di manovra per il rientro di un Satellite in orbita altamente ellittica (HEO, da Highly Elliptical Orbit).

In questo lavoro, vengono studiate le dinamiche del satellite con un modello ottenuto filtrando gli effetti sul breve periodo e poi eliminando anche la dipendenza dal nodo, fornendo una descrizione della dinamica del sistema dipendente solamente da un elemento orbitale e dal tempo t, a causa della variazione delle efemeridi dei terzi corpi. Tra i potenziali così filtrati, l'effetto J_2 dovuto alla non perfetta sfericità della Terra e l'attrazione gravitazionale dei sia del Sole che della Luna sono di fondamentale importanza per descrivere accuratamente l'evoluzione orbitale.

La validità del modello proposto per l'analisi della dinamica è qui analizzata, confrontandola con l'evoluzione a lungo termine descritta da un altro modello in cui il filtro sul nodo non è stato effettuato. Questa comparazione verrà effettuata lavorando in particolare con il sistema di riferimento di Laplace, la cui formulazione viene qui presentata in diversi scenari, considerata la peculiare variazione nel tempo causata dall'oscillazione degli elementi orbitali della Luna.

Successivamente, vengono analizzate strategie per il rientro atmosferico che sfruttano i bassi costi computazionali dei modelli per lo studio della dinamica sopra descritti, cercando un metodo che consenta al processore di bordo di pianificare autonomamente azioni per il corretto rientro in atmosfera. In particolare, viene qui proposta una strategia che implementa sia le dinamiche filtrate nel nodo che la formulazione dello spazio delle fasi, considerano elementi orbitali di terzi corpi variabili nel tempo e quindi abbandonando la semplificazione della Hamiltoniana costante. Tutto ciò operando comunque all'interno di un ambiente analitico semplificato. Questo metodo è in grado di adattare il design delle manovre all'interno del modello filtrato affrontando la dipendenza temporale. Infine, in questa tesi viene proposto un approccio ibrido che cerca di combinare gli aspetti positivi sia dei metodi semi-analitici che analitici, applicando in parte la strategia basata sullo sfruttamento dello spazio delle fasi, ma applicata all’interno di un quadro in cui le semplificazioni del sistema vengono rigettate. Questi metodi sono infine confrontati con la classica ottimizzazione globale per valutarne l’ accuratezza.

Questa tesi è parte del progetto COMPASS: “Control for orbit manoeuvring by surfing through orbit perturbations”(Grant agreement No 679086). Questo progetto è un progetto finanziato dall’European Research Council (ERC) nell’ambito della ricerca European Unions Horizon 2020.

Parole chiave: Perturbazioni orbitali; Evoluzione a lungo termine; Smaltimento a fine vita; Manovre ottimali

Contents

Abstract iii

Abstract in lingua italiana v

Contents vii

List of Figures xi

List of Tables xiii

List of Symbols xv

1 Introduction **1**
- 1.1 Problem statement and motivation . . . 1
- 1.2 State of the art . . . 3
- 1.3 Scope of the thesis and contributions . . . 6
- 1.4 Thesis outline . . . 7

2 Mathematical background **9**
- 2.1 The N-body problem . . . 9
- 2.2 The two-body problem . . . 9
- 2.3 Reference frames . . . 11
  - 2.3.1 Perifocal to inertial frame . . . 12
  - 2.3.2 Ecliptic to Inertial frame . . . 12
  - 2.3.3 Perifocal to Frenet (TNH) frame . . . 13
- 2.4 The perturbed equations of motion . . . 13
  - 2.4.1 The Lagrange planetary equations . . . 14
  - 2.4.2 The Gauss planetary equations . . . 15

3 Orbital Perturbations **17**

3.1 Gravitational perturbations . . . 17
  3.1.1 Single averaged planet asphericity . . . 20
  3.1.2 Triple averaged planet asphericity . . . 22
3.2 Third-body perturbation . . . 23
  3.2.1 Single Average . . . 28
  3.2.2 Double average . . . 32
  3.2.3 Triple average . . . 35
3.3 Hamiltonian formulation and phase space . . . 39
  3.3.1 Hamiltonian formulation . . . 39
  3.3.2 Phase space . . . 41

4 Model validation 45
4.1 Sun & Moon models . . . 45
  4.1.1 Sun model . . . 45
  4.1.2 Moon model . . . 46
4.2 Spacecraft orbital propagation . . . 47
  4.2.1 Ecliptic frame . . . 47
  4.2.2 Equatorial frame . . . 48
4.3 Laplace frame . . . 49
  4.3.1 Definition of the Laplace frame . . . 50
  4.3.2 Orbital propagation in Laplace frame . . . 52

5 Disposal manoeuvre strategy 63
5.1 Modelling . . . 64
  5.1.1 Gauss equations for impulsive manoeuvre . . . 64
  5.1.2 Constraints . . . 66
  5.1.3 Cost function . . . 67
5.2 optimisation strategies . . . 68
  5.2.1 Phase space $-\Delta\Theta$ maximization strategy . . . 69
  5.2.2 Hybrid optimisation . . . 74
  5.2.3 Global optimisation . . . 74

6 Case study 77
6.1 Disposal optimisation mission definition . . . 77
  6.1.1 INTEGRAL mission . . . 77
  6.1.2 optimisation framework . . . 78
6.2 Results . . . 79
  6.2.1 Global optimisation results . . . 79

6.2.2 Analytical $\max\left(-\Delta\Theta\right)$ strategy results 81
6.2.3 Hybrid strategy results 90

7 Conclusion **93**

Bibliography **95**

A Appendix A **101**
A.1 Integration of the TA terms for $\overline{\overline{\overline{\mathcal{R}}}}_{3b,3}$ 101
A.2 Integration of the TA terms for $\overline{\overline{\overline{\mathcal{R}}}}_{3b,4}$ 102

B Acknowledgements **111**

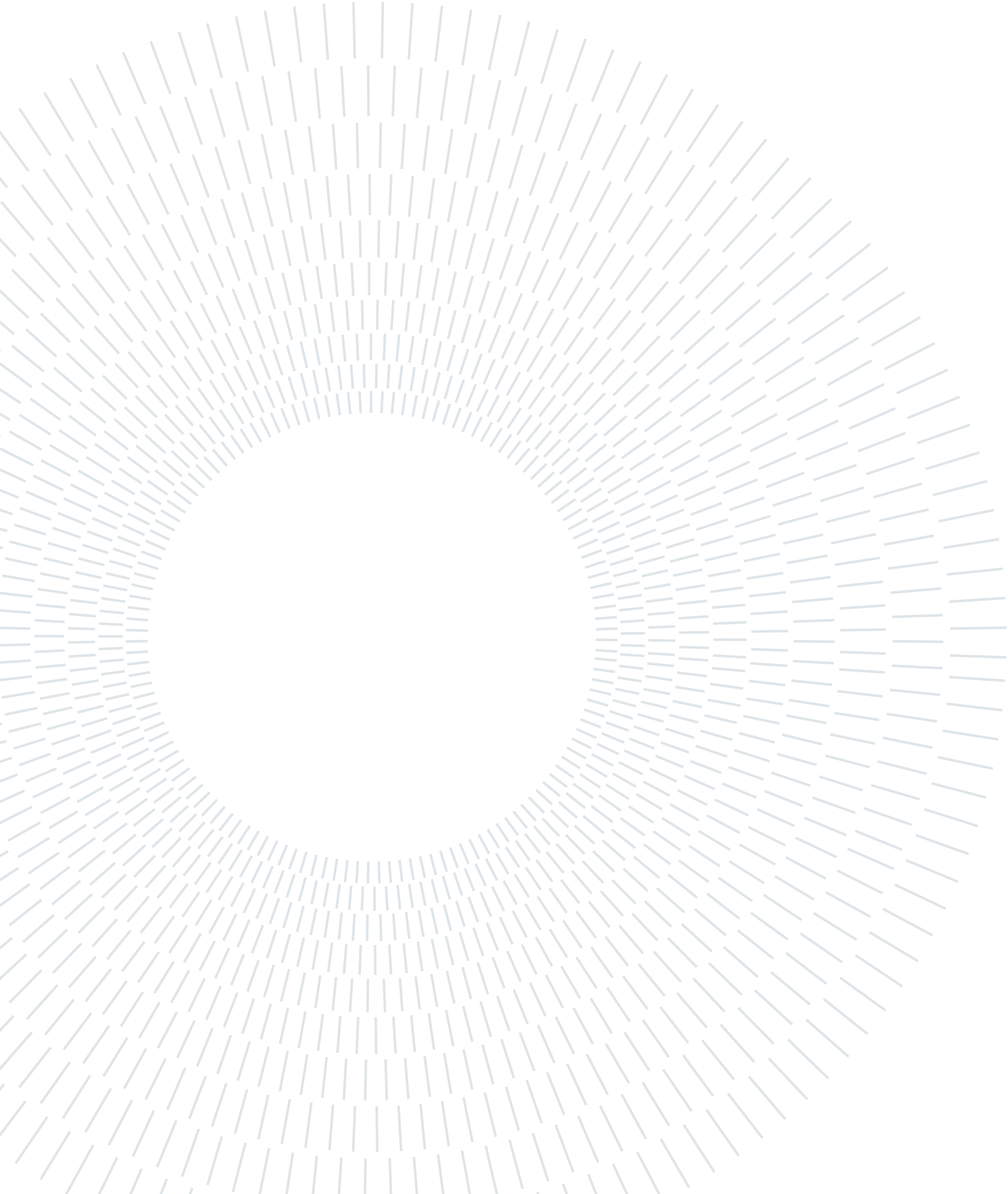

List of Figures

1.1 Number of objects on orbit, classified by their orbit. 2

3.1 Geometry of the perturbed two-body problem. 24
3.2 Phase space with $\Theta = 0.1$, libration regime. 42
3.3 Phase space with $\Theta = 0.7$, stationary regime. 42

4.1 Sun ephemerides evolution in 100 years, ecliptic frame. 45
4.2 Moon ephemerides evolution in 100 years, ecliptic frame. 46
4.3 INTEGRAL orbital elements evolution in ecliptic frame 48
4.4 INTEGRAL orbital elements evolution in equatorial frame 49
4.5 INTEGRAL orbital elements evolution in fixed L_1 frame 53
4.6 INTEGRAL orbital elements evolution in fixed L_2 frame 55
4.7 INTEGRAL orbital elements evolution in rotating L_3 frame 56
4.8 INTEGRAL orbital elements evolution in the rotating L_3 frame, using DA and TA with rotating potential $\overline{\overline{\overline{\mathcal{R}}}}_{rot}$. 57
4.9 Accuracy of the rotating Laplace frame integration method. 58
4.10 INTEGRAL orbital elements evolution in fixed average Laplace frame (case 4) 59
4.11 INTEGRAL orbital elements evolution in fixed Laplace frame (case 5) . . . 60

5.1 Manoeuvre parameters $\{\Delta v, \alpha, \beta\}$ in $\{\hat{\mathbf{T}}, \hat{\mathbf{N}}, \hat{\mathbf{H}}\}$ frame 64
5.2 Modification of the phase space topology with a decrement of the Kozai parameter Θ 70

6.1 optimised sets of manoeuvre paramaters for each manoeuvring point t_m. Found with global optimisation using DA in ecliptic frame. 80
6.2 $h_{p,min}$ evolution applying the optimised manoeuvres from the global optimisation, DA ecliptic frame 81
6.3 optimised sets of manoeuvre paramaters found with Analytical autonomous $\mathcal{H}$ optimisation. 82

6.4 $h_{p,min}$ evolution applying the optimised manoeuvres from the Analytical autonomous $\mathcal{H}$ with TA. 83

6.5 optimised sets of manoeuvre paramaters found with Analytical time-varying $\mathcal{H}$ optimisation. 85

6.6 $h_{p,min}$ evolution applying the optimised manoeuvres from the Analytical time-varying $\mathcal{H}$. 86

6.7 optimised set of manoeuvre paramaters found with Analytical time-varying $\mathcal{H}$ optimisation, L_3 frame with TA $\overline{\overline{\overline{R}}}_{rot}$. 87

6.8 Analytical autonomous $\mathcal{H}$ solution propagated with TA considering time-varying third-bodies' orbital elements. 88

6.9 Analytic time-varying $\mathcal{H}$ optimisation check with DA. 89

6.10 optimised impulse magnitude Δv found with Hybrid optimisation, re-entry checked. 91

6.11 optimised set of manoeuvring angles $\{\alpha, \beta, \theta\}$ found with Hybrid optimisation. 92

List of Tables

3.1 Legendre polynomials $P_n\left(\cos S\right)$ from order 0 to 4. 26
3.2 Dependency of various terms on the orbital elements. 28
3.3 Delaunay variables definition. 40

4.1 INTEGRAL mission orbital elements on 22/03/2013, ecliptic frame. 47
4.2 INTEGRAL mission orbital elements on 22/03/2013, equatorial frame. . . 48
4.3 Fixed mean Moon orbital elements $\{\bar{i}_{\leftmoon}, \overline{\varpi}_{\leftmoon}\}$, referred to the equatorial frame. 59
4.4 Fixed mean Moon orbital elements $\left\{\overline{a}_{\leftmoon}, \overline{e}_{\leftmoon}, \bar{i}_{\leftmoon}, \overline{\Omega}_{\leftmoon} . \overline{\varpi}_{\leftmoon}\right\}$, referred to the equatorial frame. 60

5.1 Lower and upper bounds of the optimisation variables. 67
5.2 Weighting and reference factors fixed values. 68

6.1 INTEGRAL mission orbital elements on 22/03/2013, various frames. . . . 78
6.2 Lower and upper bounds of optimisation variables. 79
6.3 Best set of manoeuvre parameters. Found with global optimisation using DA in ecliptic frame. 81
6.4 Best set of manoeuvre parameters found with Analytical optimisation with autonomous $\mathcal{H}$. 84
6.5 Best set of manoeuvre parameters found with Analytical optimisation with time-dependent $\mathcal{H}$. 87
6.6 Best set of manoeuvre parameters found with Hybrid optimisation. 91

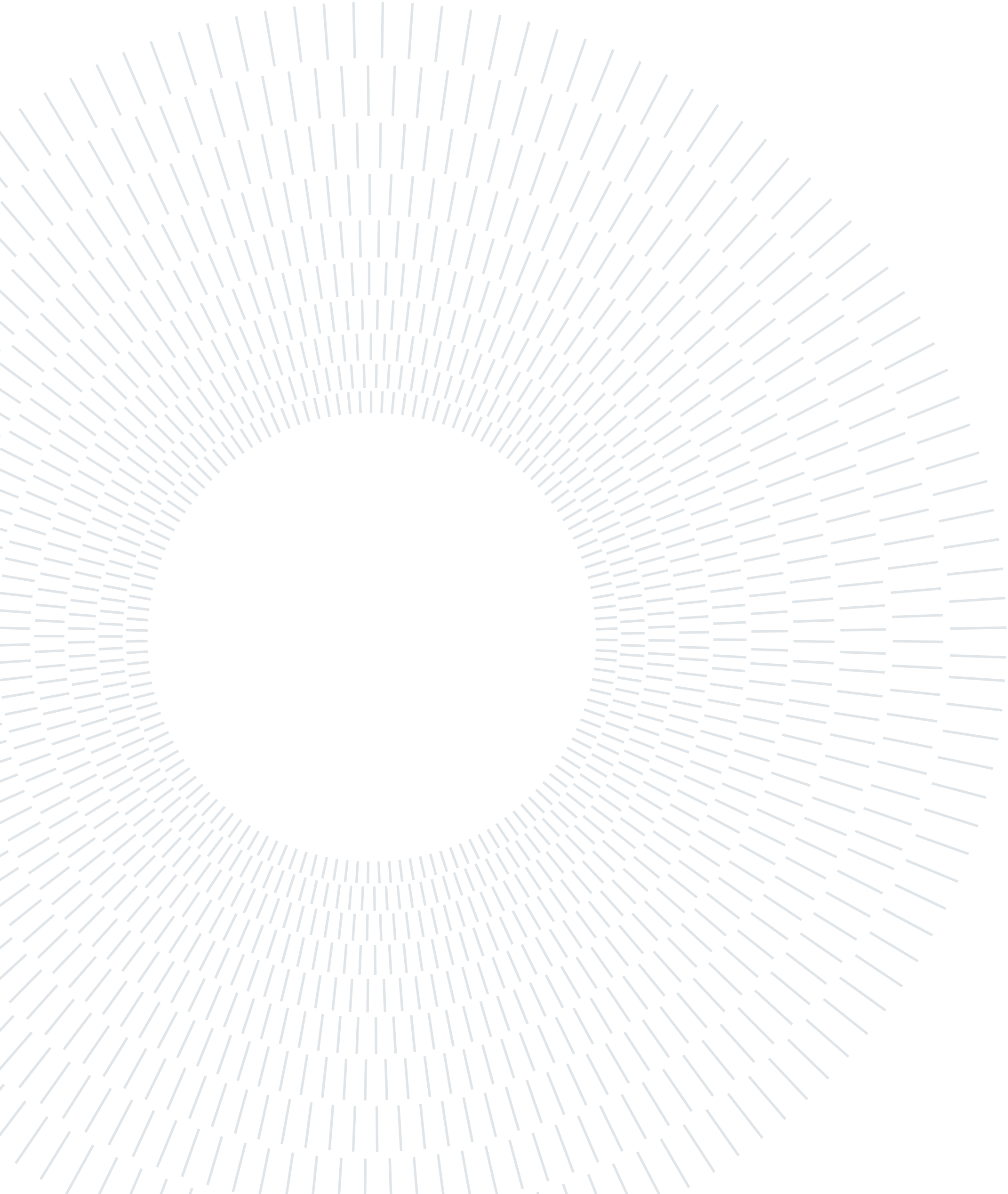

List of Symbols

Variable	**Description**	**SI unit**
a	Semi-major axis	km
e	Eccentricity	-
i	Inclination	rad
Ω	Right ascension of the ascending node	rad
ω	Argument of pericentre	rad
θ	True anomaly	rad
M	Mean anomaly	rad
n	Mean anomaly	rad/s
J_2	Coefficient of the Earth's oblateness	1082.628×10^{-6}
G	Universal gravitational constant	6.67×10^{-20} km^3/kg/s^2
μ	Earth's gravitational parameter	398,600 km^3/s^2
$\boldsymbol{r}$	Position vector	km/s
$\boldsymbol{v}$	Velocity vector	km/s
$\boldsymbol{\omega}$	Angular velocity vector	rad/s
$\mathcal{R}$	Disturbing potential	km^2/s^2
$\mathcal{H}$	Hamiltonian	km^2/s^2
$R_\oplus$	Earth's mean equatorial radius	6378.16 km
Δv	Impulse magnitude	km/s
α	In-plane firing angle	rad
β	Out-of-plane firing angle	rad
Θ	Kozai parameter	-
$\mathbf{p}$	Perturbation acceleration	km/s^2
m	Mass	kg
$\mathbf{R}$	Rotation matrix	-

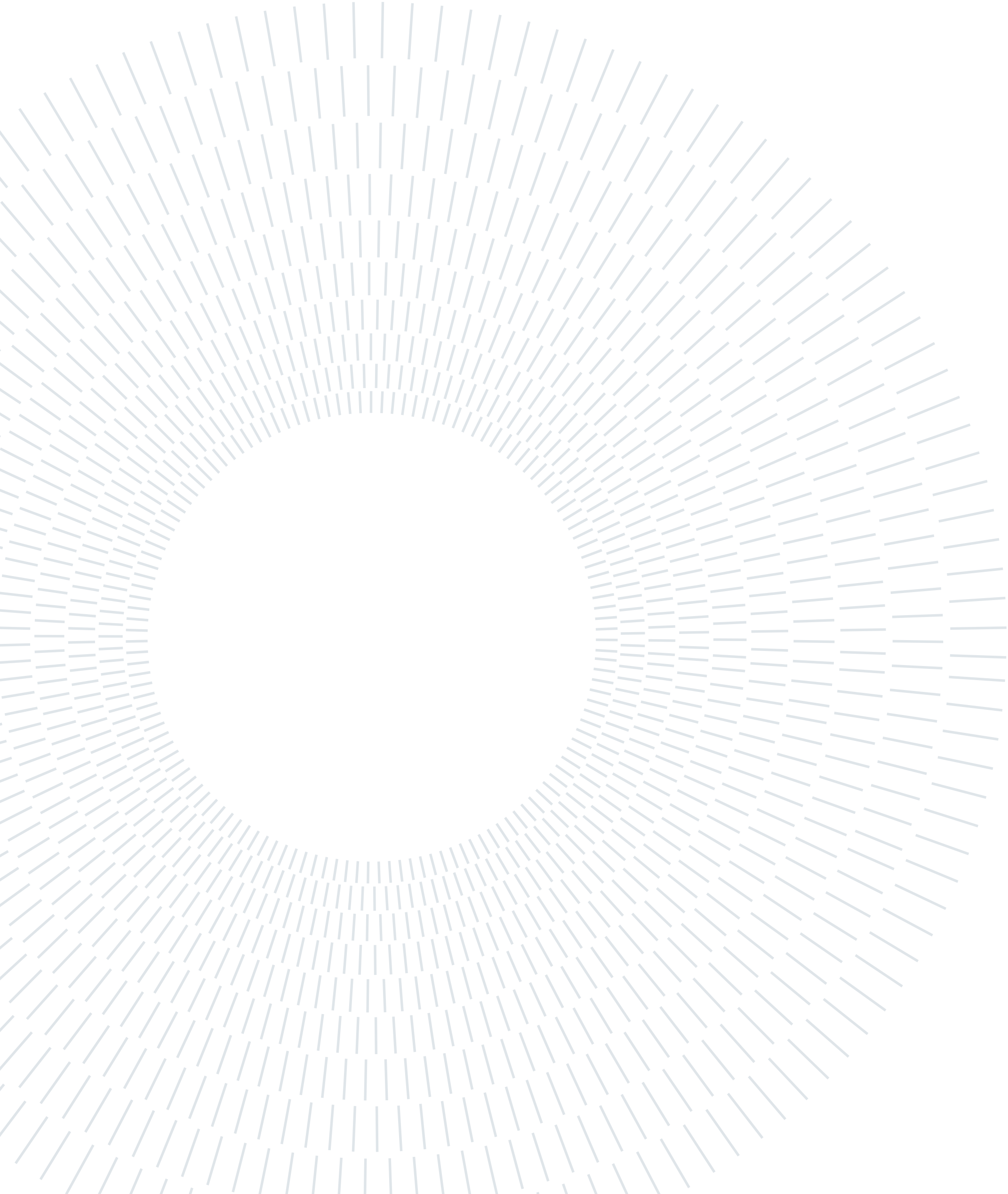

1| Introduction

> *"The eye that surveys the universe is the universe's own eye."*
> — Jostein Gaarder, *Maya*

1.1. Problem statement and motivation

The dawn of the space age started in 1957, when the Soviet Union launched Sputnik, the first-ever satellite. Since then, the Earth orbit has been flooded with tonnes of rockets and satellites sent into orbit. Initially, there was no need to plan a disposal at the end of their operations, the space was totally free, but numbers have continuously increased, to the point where collisions have become a serious threat not only to the operativeness of a satellite but to the sustainability of the space itself.

One of the earliest investigations on the congestion of the Earth's orbit was carried out in 1978 by Kessler and Palais [1]. They highlighted that the rising number of objects in space increases the risk of an impact. Moreover, collisions generate numerous fragments, some of which possess the potential to further fragment other satellites upon collision. This effect perpetuates a cycle of increasing debris, leading to an exponential rise in space objects over time and ultimately forming a debris belt around the Earth. This phenomenon in low Earth orbit (LEO) takes the name of *Kessler syndrome*.
Kessler further analysed the concept of collisional cascading of objects in orbit in [2], where it is pointed out that the space debris environment is unstable. For this reason, the complete implementation of existing mitigation guidelines is necessary. Future payloads and rocket bodies in orbit must plan their end-of-life (EoL) disposal. Moreover, there might be a necessity to retrieve certain objects already present in orbit.

Figure 1.1, taken from the latest ESA's space environment report [3], depicts the amount of identified on-orbit objects classified by their type of orbit. The majority of satellites have been launched into Low Earth Orbit (LEO), However, in recent years, the number of objects has also increased in other orbit categories. It is then evident that space debris

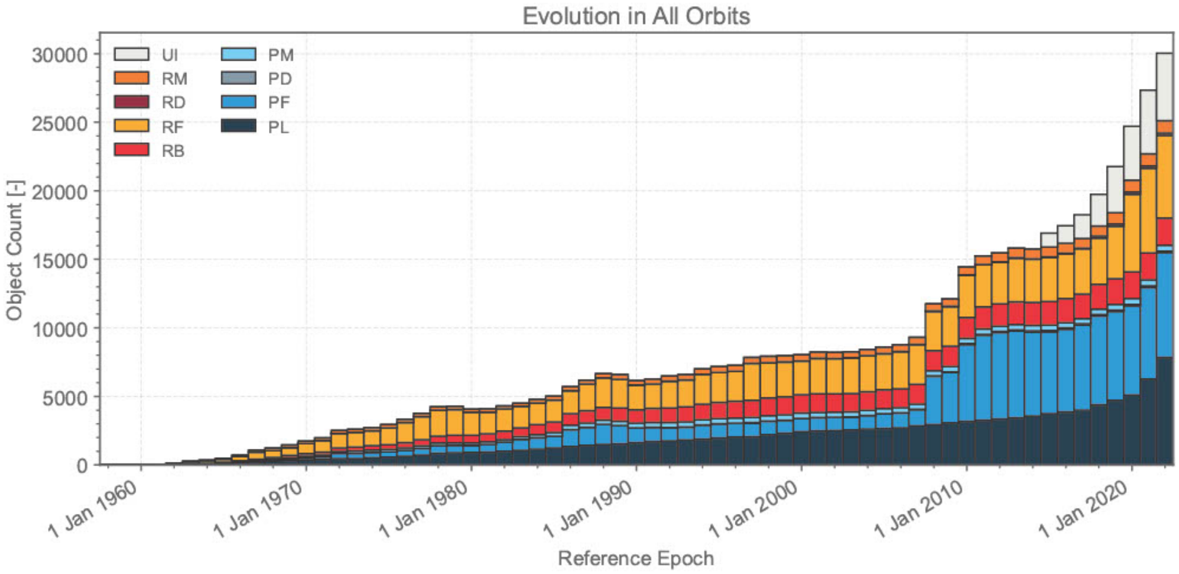

Figure 1.1: Asserted number of objects on orbit, classified by their orbit (taken from [3]).

is not an issue solely for the LEO satellites, but for the whole space environment as more satellites are launched.

From the same report, the estimated number of debris objects in orbit in the different size ranges is:

- $34,000$ object greaten than 10 cm.
- $900,000$ objects from 1 cm to 10 cm.
- 128 million objects from 1 mm to 1 cm.

Given the situation, the Inter-Agency Space Debris Coordination Committee (IADC), founded in 1993, issued guidelines for the mitigation of space debris, preventing its exponential growth before it becomes an irreversible process [4].
Those regulations state that payloads or rocket bodies found within the protected region of LEO must adhere to a maximum permanence of 25 years after becoming inoperative, whether exhibiting a permanent or periodic presence. The recommended approach within this framework involves utilizing aerodynamic drag to facilitate atmospheric reentry.
Conversely, no specific regulations are currently established for spacecraft orbiting in Medium Earth Orbit (MEO) or Highly Elliptical Orbit (HEO), the expansive nature of these zones remains largely unregulated. Nevertheless, due to their susceptibility to third-body perturbations, decommissioned satellites in HEO might eventually intersect with the protected LEO zone over an extended period. Hence, this study focuses on disposal solutions designed specifically for satellites in HEO.

The region provide a strategic advantage for astrophysics, astronomy missions like INTEGRAL [5], and Earth-focused missions like Molniya orbits. These orbits offer a unique perspective for observing both Earth and the Universe. Due to their high eccentricity, by orbiting Earth in HEOs, spacecraft remain at altitudes mostly beyond the Earth's radiation belt, minimizing interference from radiation effects. This characteristic ensures prolonged periods of uninterrupted scientific observation with minimal background noise caused by Earth's radiation.

Given the unique characteristics of these orbits, the most effective method for their disposal involves atmospheric reentry. As these orbits traverse between low and high altitudes, they are notably influenced by the primary gravitational pull due to the oblateness of the main attractor (such as Earth) and the gravitational influence of other celestial bodies, resulting in significant effects on their trajectory. Those oscillations can be exploited by means of an eccentricity. This is the problem that will be faced in this work.
This thesis was part of the COMPASS project: "Control for orbit manoeuvring by surfing through orbit perturbations" (Grant agreement No 679086). This project is European Research Council (ERC) funded project under the European Union's Horizon 2020 research

1.2. State of the art

Pioneering work in the field of third body effect was carried out by Mikhail Lidov (1926-1993) and Yoshihide Kozai (1925-2018). Independently from each other, they both contributed to the mathematical description and asserted models to face the subject. Lidov [6] was able to develop a mathematical model to describe the third-body perturbation effect produced by either the Sun or the Moon. Taking into account a wide class of orbits, he showed that if the inclination is sufficiently high, an eccentric orbit undergoes wide oscillation in both eccentricity and inclination.

Almost simultaneously, Kozai [7] studied the orbit evolution of an asteroid in the Sun-Jupiter system. He developed a model by using Delaunay's variables and exploiting the Hamiltonian perturbation theory. This way, he was able to condense the problem into a single-degree-of-freedom (DoF) and studied the secular evolution of the asteroid considering a highly inclined orbit, under the assumption of a circular orbit. For the first time, the results were represented in the Hamiltonian phase space. Both the studies converged to the same fundamental results, that is the appearance of the libration regime for orbits characterized by certain values of the so-called Kozai parameter, while the outcomes are now called the Lidov-Kozai effect.
In 1970, Kaufman investigated the influence of the Sun on a satellite in orbit about a

planet [8]. To reduce the time consumption of the numerical integration, an averaging of the disturbing function over the period of the satellite was carried out, thereby eliminating the short-period terms. The results assessed the single-averaged (SA) disturbing function of the Sun for the study of a planetary orbiter using the Lagrangian equations. In a later work, Kaufman and Dasenbrock expanded the model to account also high orbiters, up to the eighth order of the potential [9].

Since then, the interest in the third body perturbation effects has largely grown. The focus on deep space missions and the necessity to precisely determine the evolution of an orbit brought an increasing contribution to the subject. Two main application of the perturbed third-body problem has played a major role in the following studies: the use of the perturbations to establish a frozen orbit; and their exploitation for EoLdisposal. The latter problem is becoming even more prominent nowadays due to the growing interest in the space debris issue. Implementing specific mitigation measures and codes of conduct remains at least somewhat controversial. Their adoption as the formal policy will invariably raise mission costs, but today almost everyone recognizes that there is a problem [10]. In this fashion, implementing natural disposal by exploiting third-body perturbation substantially attenuates the impact on the mission cost.

Concerning frozen orbits exploitation, Delsate et al. [11] studied the stability of orbits considering The third body potential truncated at the second order, with a double-averaged (DA) process that leads to a single-DoF Hamiltonian. Moreover, it highlighted the effect of J_2 protection from instabilities. A later work from Tresaco et al. [12] considered the inclination of the Sun to the reference plane. In a further refinement of the study, the terms up to J_6 were accounted for together with the tesseral ones.
In 2001, Scheeres et al. analysed possible mission strategies to Europa using a simplified form of the dynamics using a DA model [13]. Later on, Lara and San Juan analysed frozen orbits using a specific reference frame always pointing toward Jupiter's direction. [14] Carvalho et al. [15] used a single averaged model to study orbits around Ganymede, Titan and Enceladus. Regarding Moon frozen orbits, Folta and Quinn [16] studied lunar orbits accounting for the Earth as third-body perturbater. Abad et al. in a later work exploited a synodic frame rotating with the Earth, assumed to move on a circular orbit about the Moon [17].

The other framework apart from designing frozen orbits, is focused on models aiming to develop good strategies exploiting third-body perturbation for EoLdisposal, in such a way as to significantly reduce the amount of propellant needed for de-orbiting. Recently, Lévy et al [18] developed the Semi-analytical Tool for Orbit propagation at Mars (STORM), which removes the short periodic contribution by means of averaging the conservative and dissipative perturbations The model is developed in Mars equatorial frame and takes into account drag, SRP, J_2 and Sun perturbations.

Regarding Earth, several studies have been carried out for different scenarios. While nowadays the LEO disposal strategies are trivial, for other orbit types the problem is more complex.
Concerning MEO, several studies focus on Galileo constellation simulations. In 2010, Deleflie et al. applied an averaged semi-analytical model to propagate a large number of orbits [19]. It accounts up to the 5th order term of Earth's oblateness and lunisolar effects up to the 3rd order. The results highlighted that MEO satellites can undergo a large eccentricity growth over long time scales, identifying areas where disposal orbits shall not be located.
Another study from Radtke et al. [20] focused on determining which strategy is preferable between graveyard disposal and atmospheric re-entry. For the latter, resonant effects between the perturbations were exploited, leading to an eccentricity build-up to drive the satellite inside the atmosphere.
In a later paper, focusing solely on Galileo, Gondelach et al. [21] further studied the reentry disposal strategy, using a multiobjective optimisation. The two parameters to optimise are the impulsive cost Δv and the time-to-reentry. A semi-analytical orbit propagator was implemented, using a double-average model. The analysis highlights the preferable initial values of Ω and ω to maximize the eccentricity growth and obtain a successful reentry.
In the same framework, Daquin et al. [22] carried out an in-depth study on the effects of lunisolar resonance. The crucial role played by the inclination of the Laplace plane i_L was highlighted. The expansion of the Hamiltonian was performed with a further polynomial expansion in Poincaré variables around the centre of resonance. The results show how stable and unstable manifolds induce transport and dictate objects' lifetimes.
Another work from Pellegrino et al. [23] regarding MEO satellites, further analysed the dynamic secular eccentricity growth in this region for Earth reentry. Here the solar radiation pressure contribution was also considered, taking into account satellites with two different area-to-mass (A/m) ratios. A DA is applied and its accuracy is studied in the presence of the SRP effect.

Another framework of study is represented by GEO satellites. Rosengren et al. [24] studied the exploitation of the Laplace plane as a stable graveyard disposal orbit for satellites in this region of space. The only issue is represented by the cost of moving a satellite to an inclined orbit, which can be expensive.
Gkolias and Colombo [25] studied disposal options of satellites about the geosynchronous altitude. The study shows that at this altitude the Lidov-Kozai dynamic is predominant.

Results are obtained using a semi-analytical propagator, exploiting SA.
Another work on the GEO environment by Carvalho et al. [26], explores the possibility of using a solar sail to help clean the environment, due to the relevance of the SRP contribution with large area-to-mass ratio. In this work, differently from past studies, the Sun is considered on an elliptical and inclined orbit, with a formulation based on a SA model.
A different kind of work was developed by Pinardell Pons and Noomen [27]. Instead of focusing on the EoLdisposal manoeuvre, here the focus is on determining optimal launch conditions with Ariane 5 for succeeding in a fast re-entry of launch debris.

Regarding HEO, the region studied in this work, several studies have been carried out simulating missions such as INTEGRAL (International Gamma-Ray Astrophysics Laboratory). In 2013, Colombo et al. [28] analysed two different strategies. The first one, used also in aforementioned papers, relies on lowering the perigee altitude using an eccentricity grow-up. The second strategy consists of a weak capture trajectory at the Moon, computed assuming the Circular Restricted Three-Body Problem (CR3BP) approximation. In this case, what is sought is an apogee altitude increment, paired with a decrement of the orbit inclination to exploit lunar perturbation.
In a following work, in 2019, Colombo [29] further studied the evolution of INTEGRAL-type orbits to identify the best-suited solution between the re-entry and the graveyard orbit, depending on the satellite's conditions. Finally, recent works by Asperti [30] and Scala [31] were carried out analysing the possibility of a fully-analytical optimisation design of the disposal by exploiting the Hamiltonian formulation. The idea lies in the elimination of the node dependence from the double-averaged model and assuming the third-body orbital elements as fixed, thus removing the time dependence. This allowed to reduce the satellite's dynamics to a single-DoF problem.

1.3. Scope of the thesis and contributions

This work focuses on the design of efficient disposal manoeuvres for a HEO satellite, for which past works mainly employed global optimisers. It shall be noted that, despite being an extremely accurate method for the estimation of the optimal disposal manoeuvre, they are computationally expensive. For this reason, the design cannot be carried out from the satellites' onboard microprocessors, thus requiring an allocation of resources for the ground station monitoring, even after the operative life of the satellite has ended.
To overcome this limitation, an analytical design algorithm is sought. The optimisation strategy's analysis relies on a theory that simplifies the dynamics of the HEO satellite.

This is achieved by eliminating the node in the perturbing potentials.
The ultimate goal is to provide a sufficiently accurate model to properly design and plan the disposal manoeuvre, with a sensible reduction of computational costs with respect to the classic methods. This would allow the satellite to autonomously plan its End-of-Life (EoL) disposal, without needing support from the ground segment. This would make space more accessible even to private companies.

For these reasons, this thesis further analyses the possibility of implementing an analytical disposal optimisation strategy. This task is tackled considering various case scenarios of the Laplace frame. Within those cases, also a rotating frame is used for the dynamical representation of the problem.
Differently from past works, the implementation of a time-varying frame requires dropping the assumption of constant third-bodies' orbital elements, made to obtain a single- DoF formulation of the problem. Thereafter, a new type of analytic optimisation design will be proposed and tested in this work.
Moreover, another method is proposed trying to combine the goods of both the analytical method and the semi-analytical. This latter task will be carried out seeking a solution independent of the frame employed for the study of the dynamics.

1.4. Thesis outline

After the introduction, this work is organized as follows:
In Chapter 2, the fundamentals of the perturbed two-body problem are presented to provide the necessary knowledge for the rest of the work. Also, the Gauss and Lagrange planetary equations are reported, needed for the propagation of the long-term dynamics of the orbital elements.

In Chapter 3 the formulation of the perturbing potentials is detailed, since they are needed for the dynamics representation of the problem. Moreover, their averaging procedure will be described, consisting of the filtering of the fast angles and then the node elimination. The perturbations considered are the Earth's oblateness, where only the zonal J_2 term is retained, and the lunisolar third-body perturbations.
Finally, the Hamiltonian formulation and the phase space representation are outlined. The Hamiltonian in particular will be crucial for the definition of the analytical optimisation strategy.

In Chapter 4 the averaged models of the dynamics are tested and compared, to assess their accuracy. Subsequently, the Laplace frames are defined, along with the eventual assumption made for their implementation. The propagation is therefore carried out also in those frames, and the results are compared to the ecliptic and equatorial frames.

In Chapter 5 the manoeuvre design algorithms are presented. Regarding the analytic strategy, two methods are described: the first simplifies the third-bodies' ephemerides by eliminating the time dependence; the second considers those variations. Moreover, the hybrid method is detailed, combining the analytical optimisation of the manoeuvring angles with the local optimisation of the velocity impulse.

In Chapter 6 the numerical results for the case study are presented. utilizing the INTEGRAL satellite as a bench test for the application of the proposed optimisation strategies. The optimisation is performed within each Laplace frame previously defined, for comparison. Subsequently, the optimised manoeuvring sets are tested with a reliable long-term dynamic propagation, aiming to verify the achievement of the re-entry.

Finally, Chapter 7 concludes the thesis work, describing the results obtained and possible future developments

2 Mathematical background

2.1. The N-body problem

Given N bodies represented as point masses, each subjected to the gravitational pull of the others, it is possible to express the force acting on every single body by using Newton's universal law of gravity as follows:

$$\mathbf{F}_i = -Gm_i \sum_{i \neq j}^{k} \frac{m_j}{r_{ij}^3} \mathbf{r}_{ji} \tag{2.1}$$

Where G is the universal gravitational parameter, m_i is the mass of the body subjected to the force we are considering, m_j is the mass of the j-th attractor pulling the main body, $\mathbf{r}_{ji}$ is the position vector of body i with respect to j while r_{ij} is the magnitude of the vector. Dividing each side by m_i and exploiting Newton's second law, the dynamics of the i-th body in an inertial frame becomes:

$$\ddot{\mathbf{r}}_i = -G \sum_{i \neq j}^{k} \frac{m_j}{r_{ij}^3} \mathbf{r}_{ji} \tag{2.2}$$

With $\ddot{\mathbf{r}}_i$ being the acceleration vector of the i-th body. Eq. (2.2) generally does not have a closed-form solution, but if we consider only two bodies, then the problem is integrable.

2.2. The two-body problem

This is a specific case of the N-body problem, for which a solution is retrievable. For simplicity, let $\mathbf{r}_{ij} \equiv \mathbf{r}$. The body m_1 is acted upon only by the force of gravitational attraction toward m_2 and vice versa. This forces of gravitational attraction acts along the line joining the centre of mass (CoM) of m_1 and m_2 and the absolute acceleration of the masses is given by:

$$\begin{aligned}\ddot{\mathbf{r}}_1 &= G\frac{m_2}{r^3}\mathbf{r} \\ \ddot{\mathbf{r}}_2 &= -G\frac{m_1}{r^3}\mathbf{r}\end{aligned} \tag{2.3}$$

The relative acceleration vector, recalling that $\mathbf{r} = \mathbf{r}_2 - \mathbf{r}_1$, is then:

$$\ddot{\mathbf{r}} = -G\frac{m_1 + m_2}{r^3}\mathbf{r} = -\frac{\mu}{r^3}\mathbf{r} \tag{2.4}$$

with $\mu = G(m_1 + m_2)$. A further assumption can here be made, if the secondary mass $m_2 \ll m_1$ then the CoM of the system can be considered coincident with m_1. In such a case the inertial position vector of the secondary mass is represented by the relative position vector $\mathbf{r}$. This is the typical case scenario of a satellite orbiting around a planet, with an infinitesimal mass with respect to the main body.

$$\mu = G(m_1 + m_2) \approx Gm_1 \tag{2.5}$$

Eq. (2.5) can be substituted in Eq. (2.4), and μ becomes a property of the main attractor, called the main body's gravitational parameter.
The 6 integrals of motion can be expressed in terms of orbital elements: semi-major axis a; the eccentricity of the orbit e; inclination i; the right ascension of the ascending node (RAAN) Ω; the argument of periapsis ω; the true anomaly θ. The shape of the orbit is determined by the values of a and e, while the angles i, Ω and ω define the orientation of the orbit in the considered reference frame. Then the trajectory of the spacecraft is determined by the value of θ, with the following expression:

$$r = \frac{a(1 - e^2)}{1 + e\cos\theta} \tag{2.6}$$

with θ changing in time between the interval $[0, 2\pi]$. To express the relation between the true anomaly and the time, first, let's define the mean anomaly M and its relation with the time:

$$M = \int_{tp}^{t} n dt = n(t - t_p) \tag{2.7}$$

with t_p being the time of the pericentre passage and is fixed. M represents the the azimuth position of a fictitious body moving on a circular orbit ($e = 0$) with with constant angular velocity n (defined as $n = \sqrt{\mu/a^3}$), characterised by the same a and t_p of the considered orbit. For a circular orbit, the mean anomaly M and the true anomaly θ are identical. Now, we can express M through another auxiliary variable E called Eccentric anomaly:

$$M = E - e \sin E \tag{2.8}$$

The eccentric anomaly E is defined by circumscribing the ellipse with a concentric auxiliary circle having a radius equal to the semimajor axis a of the ellipse. From the point on the ellipse identified by the true anomaly θ we pass a perpendicular to the apse line, intersecting the auxiliary circle. the latter point identifies an angle at the auxiliary circle origin that is the eccentric anomaly E. Finally, the relation between E and θ is given by:

$$\tan\frac{\theta}{2} = \frac{\sqrt{1-e}}{\sqrt{1+e}} \tan\frac{E}{2} \tag{2.9}$$

Using Eq. (2.8) and Eq. (2.9) it is possible to retrieve the relation between θ and t, with Eq. (2.6) the relation between the satellite position and the time.

2.3. Reference frames

In the following discussion, different reference frames are discussed. It is then useful to explain the rotation between one frame to the other, which is obtained by exploiting the rotation matrices:

$$\begin{gathered}
\mathbf{R}_1(\alpha) = \begin{bmatrix} 1 & 0 & 0 \\ 0 & \cos\alpha & \sin\alpha \\ 0 & -\sin\alpha & \cos\alpha \end{bmatrix} \\
\mathbf{R}_2(\alpha) = \begin{bmatrix} \cos\alpha & 0 & -\sin\alpha \\ 0 & 1 & 0 \\ \sin\alpha & 0 & \cos\alpha \end{bmatrix} \\
\mathbf{R}_3(\alpha) = \begin{bmatrix} \cos\alpha & \sin\alpha & 0 \\ -\sin\alpha & \cos\alpha & 0 \\ 0 & 0 & 1 \end{bmatrix}
\end{gathered} \tag{2.10}$$

Where $\mathbf{R}_i(\alpha)$ is the rotation matrix around the i-th axis of the generic Euler angle α

2.3.1. Perifocal to inertial frame

The perifocal frame is defined in the orbital plane and centred at the main attractor, it is identified with the set $\{\hat{\mathbf{P}},\hat{\mathbf{Q}},\hat{\mathbf{R}}\}$. $\hat{\mathbf{P}}$ is the versor pointing in the pericentre direction, $\hat{\mathbf{R}}$ aligned with the angular momentum direction and $\hat{\mathbf{Q}}$ completes the reference frame, identifying a direction pointing towards the semi-latus rectum. On the other hand, the inertial reference frame is based on the Earth, which represents its centre and is defined in the equatorial frame and is represented with the set $\{\hat{\mathbf{I}},\hat{\mathbf{J}},\hat{\mathbf{K}}\}$. $\hat{\mathbf{I}}$ is fixed and pointed in the direction of the vernal equinox (identified by the intersection between the Ecliptic and the Equatorial planes), also called the gamma point, $\hat{\mathbf{K}}$ is directed towards the North Pole and $\hat{\mathbf{J}}$ completes the orthogonal tern. This Earth-based frame is usually referred to as the Earth-Centred-Inertial (ECI) frame. The rotation from perifocal to an inertial frame is completed with three subsequent rotations about the set of Euler angles $\{\omega, i, \Omega\}$, with ω and Ω being rotations around $\hat{\mathbf{R}}$, while i rotation is performed around $\hat{\mathbf{P}}$. Note that since the rotation is counter-clockwise, the Euler angle rotations are taken negative. A generic vector rotation is therefore defined as:

$$\mathbf{v}_I = \mathbf{R}_3(-\Omega)\mathbf{R}_1(-i)\mathbf{R}_3(-\omega)\mathbf{v}_{PF} \tag{2.11}$$

While the inverse rotation is simply defined by the transpose of the rotation matrix, hence:

$$\mathbf{v}_{PF} = \mathbf{R}_3(\omega)\mathbf{R}_1(i)\mathbf{R}_3(\Omega)\mathbf{v}_I \tag{2.12}$$

2.3.2. Ecliptic to Inertial frame

The Ecliptic reference frame is based on the orbital plane of the Earth around the Sun, it is represented with the set $\{\hat{\mathbf{X}}_{ec},\hat{\mathbf{Y}}_{ec},\hat{\mathbf{Z}}_{ec}\}$. $\hat{\mathbf{X}}_{ec}$ is pointed towards the vernal equinox, while $\hat{\mathbf{Z}}_{ec}$ here is orthogonal to the Earth's orbit, with $\hat{\mathbf{Y}}_{ec}$ completing the triad. Recalling the definition of the ECI frame, we can note that $\hat{\mathbf{X}}_{ec}$ and $\hat{\mathbf{I}}$ are identified in the same way, hence $\hat{\mathbf{X}}_{ec}$ coincides with $\hat{\mathbf{I}}$. The main differentiation between the two frames is that differently from $\hat{\mathbf{Y}}_{ec}$, in ECI frame $\hat{\mathbf{K}}$ lies on the North Pole direction. Once defined the tilt angle ϵ between the two versors, we can switch from one frame to the other with one single rotation as follows, considering the rotation of a generic vector:

$$\mathbf{v}_{ec} = \mathbf{R}_1(\epsilon)\mathbf{v}_{eq} \tag{2.13}$$

$$\mathbf{v}_{eq} = \mathbf{R}_1(-\epsilon)\mathbf{v}_{ec} \tag{2.14}$$

2.3.3. Perifocal to Frenet (*TNH*) frame

Another important reference frame is the so-called Frenet *TNH* reference frame which, differently from the previous ones, is centred on the satellite and is represented with the set $\{\hat{\mathbf{T}}, \hat{\mathbf{N}}, \hat{\mathbf{H}}\}$, from where it takes the name. $\hat{\mathbf{T}}$ is directed towards the velocity direction, hence changing orientation in time, $\hat{\mathbf{H}}$ is normal to the orbital plane and $\hat{\mathbf{N}}$ completes the set. To better understand this, the frame representation is represented together with the perifocal one in Fig(...). It is clear from the picture that, to define the rotation, two angles are needed. One being θ and the other defined as ϕ_{FPA} being the flight path angle, and computed as follows:

$$\tan\phi_{FPA} = \frac{e\sin\theta}{1 + e\cos\theta} \tag{2.15}$$

Once this angle is known, a generic vector can be represented in the *tnh* starting from the perifocal frame $\{\hat{\mathbf{P}}, \hat{\mathbf{Q}}, \hat{\mathbf{R}}$, by applying a rotation around the third axis $\hat{\mathbf{R}}$ (and vice versa around axis $\hat{\mathbf{H}}$): Once this angle is known, a generic vector can be represented in the *tnh* starting from the perifocal frame $\{\hat{\mathbf{P}}$,$\hat{\mathbf{Q}}$,$\hat{\mathbf{R}}$, by applying a rotation around the third axis $\hat{\mathbf{R}}$ (and vice versa around axis $\hat{\mathbf{H}}$):

$$\mathbf{v}_{TNH} = \mathbf{R}_3(\frac{\pi}{2} + \theta - \phi_{FPA})\mathbf{v}_{PF} \tag{2.16}$$

$$\mathbf{v}_{PF} = \mathbf{R}_3(\phi_{FPA} - \frac{\pi}{2} - \theta)\mathbf{v}_{TNH} \tag{2.17}$$

2.4. The perturbed equations of motion

The equations of motion previously discussed (Eq. 2.4) are based on the assumption that the only forces acting on the two considered bodies are their reciprocal attraction due to their spherically symmetric gravitational field. This is not the case and we have commonly a numerous amount of perturbations acting on the bodies, such as atmospheric drag, Solar Radiation Pressure (SRP), gravitational interaction with other celestial bodies like the Moon and Sun for an orbiter around the Earth, but also a perturbation due to the nonsphericity of the main attractor and the impulsive thrust of a manoeuvre.

Commonly the magnitude of those perturbative accelerations is smaller than the main body's spherically symmetric gravitational attraction, but that's not always the case. For example, at low altitudes, the acceleration due to the atmospheric drag is big enough to de-orbit a satellite, while at high altitudes it can be considered negligible. The dependence on the altitude is not the same for all the perturbative terms here mentioned, the SRP for example does not depend at all on it. The equations of motion considering the effects of those perturbations can be written as:

$$\ddot{\mathbf{r}} = -\frac{\mu}{r^3}\mathbf{r} + \mathbf{p} \tag{2.18}$$

With **p** being the net perturbative acceleration from all the different sources other than the spherically symmetric gravitational forces between the two considered bodies. Those perturbations could be exploited wisely in the mission design for various reasons, one being the de-orbit of a satellite. Generally, even if non-negligible, the magnitude of those secondary accelerations is smaller than the main effect accounted for in the simple two-body problem. Since in such a case a fully analytical solution is not feasible, a numerical integration is needed. To ease the computation it is better to switch from the cartesian coordinates to the orbital elements, which tend to oscillate around their 2-body values. In the case of cartesian coordinates instead, the position and velocity vector undergo a large variation, greatly increasing the computational cost of the integration. The two most used schemes to integrate the perturbed two-body problem are the Lagrangian and the Gauss equations.

2.4.1. The Lagrange planetary equations

Whenever the perturbative forces acting on the satellite are conservative, the Lagrange planetary equations represent a well-suited method to perform the numerical integration. These equations are expressed in terms of the conservative disturbing functions $\mathcal{R}$ (See Karttunen [32], Vallado [33], El'iasberg [34] for reference):

$$
\begin{aligned}
\frac{da}{dt} &= \frac{2}{na}\frac{\partial \mathcal{R}}{\partial M} \\
\frac{de}{dt} &= \frac{1}{na^2e}\left(\left(1-e^2\right)\frac{\partial \mathcal{R}}{\partial M} - \sqrt{1-e^2}\frac{\partial \mathcal{R}}{\partial \omega}\right) \\
\frac{di}{dt} &= \frac{1}{na^2\sin i\sqrt{1-e^2}}\left(\cos i\frac{\partial \mathcal{R}}{\partial \omega} - \frac{\partial \mathcal{R}}{\partial \Omega}\right) \\
\frac{d\Omega}{dt} &= \frac{1}{na^2\sin i\sqrt{1-e^2}}\frac{\partial \mathcal{R}}{\partial i} \\
\frac{d\omega}{dt} &= -\frac{1}{na^2\sin i\sqrt{1-e^2}}\cos i\frac{\partial \mathcal{R}}{\partial i} + \frac{\sqrt{1-e^2}}{na^2e}\frac{\partial \mathcal{R}}{\partial e} \\
\frac{dM}{dt} &= n - \frac{1-e^2}{na^2e}\frac{\partial \mathcal{R}}{\partial e} - \frac{2}{na}\frac{\partial \mathcal{R}}{\partial a}
\end{aligned}
\tag{2.19}
$$

the conservative force term $\mathcal{R}$ can be written as the sum of the various single conservative forces in action:

$$
\mathcal{R} = \sum_{i}^{N_p}\mathcal{R}_i \tag{2.20}
$$

with N_p being the number of the perturbation terms considered.

2.4.2. The Gauss planetary equations

Whenever the disturbing forces are non-conservative, the Lagrange equations are no longer applicable. In such a case, a solution can be found by using the Gauss planetary equations, which depend on the perturbative acceleration vector $\mathbf{p}$ induced by the disturbing forces. Using as reference frame an $\{\hat{r}, \hat{s}, \hat{w}\}$ set where the $\hat{r}$ is the radial component at any point in the point, $\hat{w}$ is directed along the perpendicular to the orbital plane and $\hat{s}$ completes the frame, it is possible to decompose $\mathbf{p}$ in its three components p_r, p_s, p_w and it is then possible to express the set of equations as follows (see Curtis [35] for reference):

$$
\begin{aligned}
\frac{da}{dt} &= rp_s \\
\frac{de}{dt} &= \frac{h}{\mu}\sin\theta p_r + \frac{1}{\mu h}\left(\left(h^2+\mu r\right)\cos\theta + \mu e r\right)p_s \\
\frac{d\theta}{dt} &= \frac{h}{r^2} + \frac{1}{eh}\left(\frac{h^2}{\mu}\cos\theta p_r - \left(r+\frac{h^2}{\mu}\right)\sin\theta p_s\right) \\
\frac{d\Omega}{dt} &= \frac{r}{h\sin i}\sin u p_w \\
\frac{di}{dt} &= -\frac{r}{h}\cos u p_w \\
\frac{d\omega}{dt} &= -\frac{1}{eh}\left(\frac{h^2}{mu}\cos\theta p_r - \left(r+\frac{h^2}{\mu}\right)\sin\theta p_s\right) - \frac{r\sin u}{h\tan i}p_w
\end{aligned}
\tag{2.21}
$$

where $h = \sqrt{\mu a\left(1-e^2\right)}$ is the orbital angular momentum, r is the magnitude from the main body centre, μ is the main body's planetary gravitational parameter and $u = \omega + \theta$ is the argument of latitude.

3 Orbital Perturbations

3.1. Gravitational perturbations

The Earth and other celestial bodies are not perfect spheres, but rather oblate spheroids. The centrifugal forces exerted by the rotation around the spin axis cause an equatorial bulge, consequently, the gravitational field varies both with the latitude and the radius. Following the description from Vallado [33] and Blitzer[36], the mathematical description of the Earth's irregular gravitational potential relies on spherical harmonic expansion, using the Legendre polynomials. This geopotential can be expressed by highlighting two different separated contributions, one independent of the longitude called *zonal* harmonic and one dependent on it, called *tesseral* harmonic:

$$V = -\frac{\mu}{r}\left[1 - \sum_{l=2}^{\infty} J_l \left(\frac{R_\oplus}{r}\right)^l P_l\left(\sin\phi\right) + \sum_{l=2}^{\infty}\sum_{m=1}^{l}\left(\frac{R_\oplus}{r}\right)^l P_{lm}\left(\sin\phi\right) J_{lm} \cos m\left(\lambda - \lambda_{lm}\right)\right] \tag{3.1}$$

where

- μ is the Earth's gravitational parameter.
- r is the satellite geocentric distance.
- $R_\oplus$ is the mean equatorial radius of the Earth.
- P_{lm} is the associated Legendre polynomial of degree l and order m.
- J_{lm} and λ_{lm} are constants depending on the planet's mass distribution, in the zonal harmonic term $m = 0$, hence $J_l = -J_{l0}$ (the minus sign is purely conventional).
- λ is the geographic longitude
- ϕ is the geographic latitude

In this thesis, only the zonal harmonics would be considered and since the disturbing function is the negative of the disturbing potential, the potential expression is reduced to:

$$R = -\frac{\mu}{r}\sum_{l=2}^{\infty} J_l \left(\frac{R_\oplus}{r}\right)^l P_l \sin\phi \tag{3.2}$$

Additionally, only the dominant term J_2 will be taken into account since this is a reasonable assumption in the case of a HEO satellite, which is the focus of this work. This yields to:

$$R = -\frac{\mu J_2 R_\oplus^2}{2r^3}(3\sin^2\phi - 1) \tag{3.3}$$

For orbits in the vicinity of the Earth, additional terms would be needed to achieve a faithful description.

R_{J_2} in a generic frame

The position of a satellite in a cartesian coordinate system can be expressed, in a generic frame, starting from the orbital elements. The formulation is given by Eq. (2.11), which can be rewritten considering that $\mathbf{r}_{PF} = \mathbf{R}_3(-\theta)\,[r, 0, 0]^T$, yielding to the following:

$$\begin{bmatrix} x \\ y \\ z \end{bmatrix}_{gf} = \mathbf{R}_3(-\Omega)\mathbf{R}_1(-i)\mathbf{R}_3(-\omega-\theta)\begin{bmatrix} r \\ 0 \\ 0 \end{bmatrix} \tag{3.4}$$

where the orbital elements and the result coordinates are referred to the generic frame considered.

Hereafter the vector in the generic frame can be rotated to the equatorial frame with a rotation sequence, here reported as follows:

$$\begin{bmatrix} x \\ y \\ z \end{bmatrix}_{eq} = \mathbf{R}_1(\alpha)\mathbf{R}_2(\beta)\mathbf{R}_3(\gamma)\begin{bmatrix} x \\ y \\ z \end{bmatrix}_{gf} = \mathbf{R}_{gf2eq}\mathbf{R}_3(-\Omega)\mathbf{R}_1(-i)\mathbf{R}_3(-\omega-\theta)\begin{bmatrix} r \\ 0 \\ 0 \end{bmatrix} \tag{3.5}$$

with the angles $\{\alpha, \beta, \gamma\}$ dependent on the orientation of the chosen frame with respect to the equatorial one, while $\mathbf{R}_{gf2eq}$ is the resultant rotation matrix.

Recalling Eq. (3.3), the sinus of the latitude of a satellite is computed from:

$$\begin{aligned} \sin\phi = \frac{z_{eq}}{r} = \frac{xR_{gf2eq}^{(3,1)} + yR_{gf2eq}^{(3,2)} + zR_{gf2eq}^{(3,3)}}{r} = \\ = \cos\left(\omega+\theta\right)\left(R_{gf2eq}^{(3,1)}\cos\Omega + R_{gf2eq}^{(3,2)}\sin\Omega\right) + \Big[R_{gf2eq}^{(3,3)}\sin i + ... \\ + \cos i\left(R_{gf2eq}^{(3,2)}\cos\Omega - R_{gf2eq}^{(3,1)}\sin\Omega\right)\Big]\sin\left(\omega+\theta\right) \end{aligned} \tag{3.6}$$

where {x, y, z} are the coordinates in the generic frame and $R_{gf2eq}^{(i,j)}$ corresponds to the element in the i-th row, j-th column of the rotational matrix.

The expression of the potential in a generic frame is retrieved by inserting Eq. (3.6) into Eq. (3.3), leading to:

$$\begin{aligned} \mathcal{R}_{J_2} = -\frac{\mu J_2 R_\oplus^2 \left(1+e\cos\theta\right)^3}{2a^3\left(1-e^2\right)^3}\Bigg\{-1+3\Big[\cos\left(\omega+\theta\right)\Big(R_{gf2eq}^{(3,1)}\cos\Omega + ... \\ +R_{gf2eq}^{(3,2)}\sin\Omega\Big) + \Big(R_{gf2eq}^{(3,3)}\sin i + \cos i\Big(R_{gf2eq}^{(3,2)}\cos\Omega + ... \\ -R_{gf2eq}^{(3,1)}\sin\Omega\Big)\Big)\sin\left(\omega+\theta\right)\Big]^2\Bigg\} \end{aligned} \tag{3.7}$$

Ecliptic frame

In the case of ecliptic frame the rotational matrix reduces to $R_1\left(-\epsilon\right)$, hence Eq. (3.6) is simplified to:

$$\begin{aligned} \sin\phi = \frac{z_{eq}}{r} = \frac{z\cos\epsilon + y\sin\epsilon}{r} = \\ = \cos\left(\omega+\theta\right)\sin\epsilon\sin\Omega + \left(\cos i\cos\Omega\sin\epsilon + \cos\epsilon\sin i\right)\sin\left(\omega+\theta\right) \end{aligned} \tag{3.8}$$

Inserting the latter in the potential expressed in Eq. (3.3) the result is:

$$\begin{aligned} \mathcal{R}_{J_2} = -\frac{J_2\mu R_\oplus^2\left(1+e\cos\theta\right)^3}{2a^3\left(1-e^2\right)^3}\Bigg\{-1+3\Big[\cos\left(\omega+\theta\right)\sin\epsilon\sin\Omega + ... \\ + \left(\cos i\cos\Omega\sin\epsilon + \cos\epsilon\sin i\right)\sin\left(\omega+\theta\right)\Big]^2\Bigg\} \end{aligned} \tag{3.9}$$

Equatorial frame

Considering the equatorial reference frame, the rotational matrix becomes simply the identity matrix, leading to:

$$\sin\phi = \frac{z_{eq}}{r} = \sin i \sin\left(\omega + \theta\right) \tag{3.10}$$

which brings to the following expression of the potential:

$$\mathcal{R}_{J_2} = -\frac{J_2 \mu R_{\oplus}^2 \left(1 + e\cos\theta\right)^3 \left(-1 + 3\sin^2 i \sin^2\left(\omega + \theta\right)\right)}{2a^3\left(1 - e^2\right)^3} \tag{3.11}$$

3.1.1. Single averaged planet asphericity

In the present work, an averaged model of the potentials is used to lower the computational costs. This method allows to cancel out the short-term effect due to the true anomaly variation along the orbit. This cancellation is not a problem since the focus is on the long-term dynamics of the satellite.

The averaging is performed over one orbital period, with all the orbital elements being considered constant apart from the true anomaly.

The following computations were performed analytically using Mathematica ® software, starting from the integration of the general expression reported in Eq. (3.7) over the satellite's mean anomaly M as follows:

$$\overline{\mathcal{R}}_{J_2} = \frac{1}{2\pi}\int_0^{2\pi} \mathcal{R} dM \tag{3.12}$$

where dM can be expressed in terms of $d\theta$ as:

$$dM = \frac{\left(1 - e^2\right)^{3/2}}{\left(1 + e\cos\theta\right)^2} d\theta \tag{3.13}$$

Inserting Eq. 3.13 into Eq. 3.12 and computing it is possible to obtain the SA expression of the zonal J_2 perturbation potential:

$$
\begin{aligned}
\overline{\mathcal{R}}_{J_2} = \frac{1}{2\pi}\int_0^{2\pi} \mathcal{R}_{J_2} dM = -\frac{J_2 \mu R_\oplus^2}{16 a^3 \left(1-e^2\right)^{3/2}} \Bigg[& -8 + 9\left(R_{31}^2 + R_{32}^2 + \frac{2}{3}R_{33}^2 + \right) + \ldots \\
& + 3\left(R_{31}^2 + R_{32}^2 - 2R_{33}^2\right)\cos 2i + \ldots \\
& + 6\left(R_{31} - R_{32}\right)\left(R_{31} + R_{32}\right)\cos 2\Omega \sin^2 i + \ldots \\
& + 12\Bigg(R_{33}\sin 2i \left(R_{32}\cos\Omega - R_{31}\sin\Omega\right) + \ldots \\
& + R_{31}R_{32}\sin^2 i \sin 2\Omega \Bigg)\Bigg]
\end{aligned}
\tag{3.14}
$$

where for simplicity, the notation for the elements of the rotation matrix $\mathbf{R}_{gf2eq}$ is simplified as: $R_{gf2eq}^{(i,j)} \equiv R_{ij}$.

Note that Eq. 3.14 does not depend on the third body's fast angle. Since the double averaging technique will be performed along the third body true anomaly (as it will be shown in Section 3.2.2), this means that the SA and DA expressions of the zonal J_2 perturbing potential are equal. Namely:

$$
\overline{\overline{\mathcal{R}}}_{J_2} = \frac{1}{2\pi}\int_0^{2\pi} \overline{\mathcal{R}}_{J_2} dM_{3b} = \overline{\mathcal{R}}_{J_2}
\tag{3.15}
$$

Hereafter, it is possible to pass directly to the triple-averaging computation.

Ecliptic frame

The latter result, in the context of a satellite whose orbital elements are expressed in the ecliptic frame, can be rewritten as:

$$
\begin{aligned}
\overline{\mathcal{R}}_{J_2} = & \frac{J_2 \mu R_\oplus^2}{32 a^3 (1-e^2)^{3/2}} \Big[(1 + 3\cos 2\epsilon)(1 + 3\cos 2i) + \ldots \\
& + 12\cos 2\Omega \sin^2\epsilon \sin^2 i - 12\cos\Omega \sin 2\epsilon \sin 2i \Big]
\end{aligned}
\tag{3.16}
$$

Equatorial frame

And again, in the special scenario in which the satellite orbital elements are already considered in the equatorial frame, the averaged geopotential reduces to:

$$\overline{\mathcal{R}}_{J_2} = \frac{J_2 \mu R_\oplus^2 \left(1 + 3\cos 2i\right)}{8a^3(1-e^2)^{3/2}} \tag{3.17}$$

3.1.2. Triple averaged planet asphericity

As it will be discussed in Section 3.3.2, some requirements are needed to allow a simplified single-DoF system dynamics such that a 2D representation is possible.

- independence on the fast angle M (obtained via SA).
- independence on the node Ω.

The requirement of independence on the fast angle M has already been achieved through the SA procedure, while for the second requirement, the node elimination is needed.
For this reason, further simplifications are needed. Regarding the node dependence, as proposed by Gkolias [25] and analised by Asperti [30], an additional averaging procedure is carried out.
The Triple Average (TA) requires an integration over the satellite right ascension of the ascending node Ω. In this way, the potential will not depend anymore on the satellite node.

The triple averaging procedure expression is therefore computed as:

$$\overline{\overline{\overline{\mathcal{R}}}}_{J_2} = \frac{1}{2\pi}\int_0^{2\pi} \overline{\overline{\mathcal{R}}}_{J_2} d\Omega \tag{3.18}$$

Applying this averaging procedure to the general expression of the DA potential in Eq. 3.14, and remembering from Eq. (3.15) that the DA is equal to the SA one for the J_2 perturbation, the TA expression of the J_2 perturbing potential is obtained as reported:

$$\begin{aligned}\overline{\overline{\overline{\mathcal{R}}}}_{J_2} = \frac{1}{2\pi}\int_0^{2\pi} \mathcal{R}_{J_2} d\Omega = -\frac{J_2 \mu R_\oplus^2}{16a^3(1-e^2)^{3/2}}\Bigg[-8 + 9\left(R_{31}^2 + R_{32}^2 + \frac{2}{3}R_{33}^2\right) + \ldots \\ + 3\left(R_{31}^2 + R_{32}^2 - 2R_{33}^2\right)\cos 2i\Bigg]\end{aligned} \tag{3.19}$$

Ecliptic frame

If the ecliptic frame is considered, the expression in Eq. 3.19, reduces to:

$$\overline{\overline{\overline{\mathcal{R}}}}_{J_2} = \frac{J_2 \mu R_\oplus^2 \left(1 + 3\cos 2\epsilon\right)\left(1 + 3\cos 2i\right)}{32a^3(1-e^2)^{3/2}} \tag{3.20}$$

Equatorial frame

The equatorial frame on the other hand represents a particular case for the TA expression of the zonal perturbation potential. In this frame, the expression of the SA from Eq. (3.17) does not depend on the satellite node, hence the expression is unchanged with respect to both the DA and the SA potentials:

$$\overline{\overline{\overline{\mathcal{R}}}}_{J_2} = \overline{\mathcal{R}}_{J_2} = \frac{J_2 \mu R_\oplus^2 \left(1 + 3\cos 2i\right)}{8a^3(1-e^2)^{3/2}} \tag{3.21}$$

3.2. Third-body perturbation

Considering a system of three bodies with Earth being the main attractor, a satellite orbiting around Earth and the third body being a perturber, it is possible to express the equation of motion in an inertial reference system centred at the centre of mass (CoM). Considering the forces acting on the satellite, as described by Vallado [33], it is possible to write:

$$\ddot{\mathbf{r}}_S = -\frac{Gm_\oplus}{r_{\oplus S}^3}\mathbf{r}_{\oplus S} + \frac{Gm_{3b}}{r_{S3b}^3}\mathbf{r}_{S3b} \tag{3.22}$$

With $\mathbf{r}_S$ being the position vector of the satellite from the centre of mass, $\mathbf{r}_{\oplus S}$ the position vector of the satellite with respect to the Earth, $\mathbf{r}_{S3b}$ the position vector of the third body with respect to the satellite, $m_\oplus$ representing the Earth's mass, and m_{3b} the third body's mass. The geometry of the problem is reported in Fig. 3.1

Since $\mathbf{r}_S = \mathbf{r}_\oplus + \mathbf{r}_{\oplus S}$, its differentiation leads to:

$$\ddot{\mathbf{r}}_S = \ddot{\mathbf{r}}_\oplus + \ddot{\mathbf{r}}_{\oplus S} \tag{3.23}$$

with $\mathbf{r}_\oplus$ being the position vector of the Earth from the centre of mass.
Assuming that the satellite mass is negligible compared to the other two bodies, the motion of the Earth depends only on the pull exerted by the third body. Applying

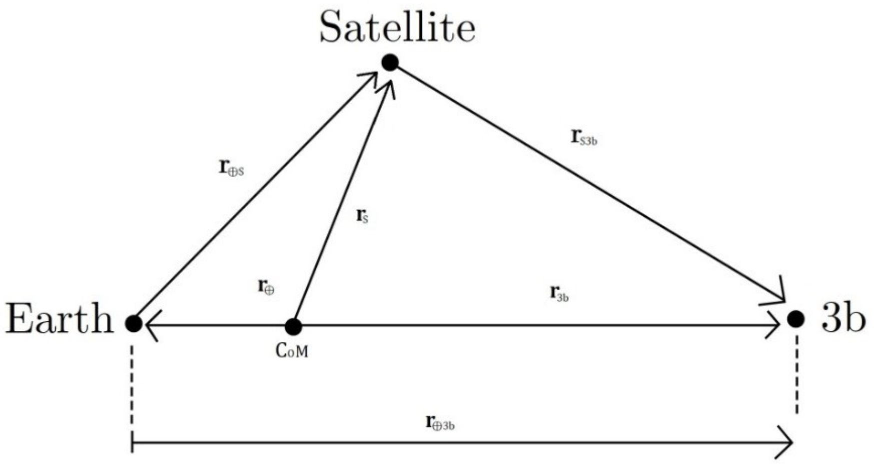

Figure 3.1: Geometry of the perturbed two-body problem.

Newton's gravity law:

$$\ddot{\mathbf{r}}_\oplus = \frac{Gm_3}{r^3_{\oplus 3b}} \mathbf{r}_{\oplus 3b} \tag{3.24}$$

with $\mathbf{r}_{\oplus 3b}$ being the position vector of the third body with respect to the Earth. Inserting Eqs. (3.23) and (3.24) into Eq.(3.22) and calling respectively $\mu_{3b} = Gm_{3b}$ and $\mu = Gm_\oplus$ leads to:

$$\ddot{\mathbf{r}}_{\oplus S} = -\frac{\mu}{r^3_{\oplus S}} \mathbf{r}_{\oplus S} + \mu_{3b} \left(\frac{\mathbf{r}_{S3b}}{r^3_{S3b}} - \frac{\mathbf{r}_{\oplus 3b}}{r^3_{\oplus 3b}} \right) \tag{3.25}$$

In the latter equation, it is possible to identify two distinct terms, one being the 2-body solution found in Eq. (2.4) and the other representing the perturbation contribution of the third-body:

$$\mathbf{a}_{3b} = \mu_{3b} \left(\frac{\mathbf{r}_{S3b}}{r^3_{S3b}} - \frac{\mathbf{r}_{\oplus 3b}}{r^3_{\oplus 3b}} \right) \tag{3.26}$$

Now, recalling that $\mathbf{r}_{S3b} = \mathbf{r}_{\oplus 3b} - \mathbf{r}_{\oplus S}$, it can be shown [37] that $\mathbf{a}_{3b}$ admits a potential in the following form:

$$\mathcal{R}_{3b} = \mu_{3b} \left(\frac{1}{\|\mathbf{r}_{\oplus 3b} - \mathbf{r}_{\oplus S}\|} - \frac{\mathbf{r}_{\oplus S} \cdot \mathbf{r}_{\oplus 3b}}{r^3_{\oplus 3b}} \right)$$

To simplify the notation, since all the position vectors are given with respect to the Earth, in the following work $r_{\oplus S} \equiv r$ and $r_{\oplus 3b} \equiv r_{3b}$, hence rewriting:

$$\mathcal{R}_{3b} = \mu_{3b} \left(\frac{1}{\|\mathbf{r}_{3b} - \mathbf{r}\|} - \frac{\mathbf{r} \cdot \mathbf{r}_{3b}}{r_{3b}^3} \right) \tag{3.27}$$

Following the procedure from Kaufman [8], by using the cosine law and considering the geometry of the problem, the term $\|\mathbf{r}_{3b} - \mathbf{r}\|$ can be rewritten as:

$$\|\mathbf{r}_{3b} - \mathbf{r}\| = \left(r^2 + r_{3b}^2 - 2 r r_{3b} \cos S \right)^{1/2} \tag{3.28}$$

with S being the angle between $\mathbf{r}$ and $\mathbf{r}_{3b}$. Therefore the term in Eq. (3.27) becomes:

$$\frac{1}{\|\mathbf{r}_{3b} - \mathbf{r}\|} = \frac{1}{r_{3b}} \left[1 - 2 \frac{r}{r_{3b}} \cos S + \left(\frac{r}{r_{3b}} \right)^2 \right]^{-1/2} \tag{3.29}$$

Regarding instead the second term of Eq. (3.27), it can be expressed as:

$$\frac{\mathbf{r} \cdot \mathbf{r}_{3b}}{r_{3b}^3} = \frac{r r_{3b} \cos S}{r_{3b}^3} = \frac{1}{r_{3b}} \frac{r}{r_{3b}} \cos S \tag{3.30}$$

Plugging Eqs. (3.29) and (3.30) in Eq. (3.27) the third body potential is rewritten as follows:

$$\mathcal{R}_{3b} = \frac{\mu_{3b}}{r_{3b}} \left\{ \left[1 - 2 \frac{r}{r_{3b}} \cos S + \left(\frac{r}{r_{3b}} \right)^2 \right]^{-1/2} - \frac{r}{r_{3b}} \cos S \right\} \tag{3.31}$$

At this point, the potential $\mathcal{R}_{3b}$ can be expanded in McLaurin series using Legendre Polynomials. The result of this operation is here reported:

$$\mathcal{R}_{3b} = \frac{\mu_{3b}}{r_{3b}} \left[\sum_{n=0}^{\infty} \left(\frac{r}{r_{3b}} \right)^n P_n \left(\cos S \right) - \frac{r}{r_{3b}} P_1 \cos S \right] \tag{3.32}$$

The first four orders of the Legendre Polynomials $P_n \left(\cos S \right)$ are reported in Table (3.1).

n	$P_n(\cos S)$
0	1
1	$\cos S$
2	$1/2\,(3\cos^2 S - 1)$
3	$1/2\,(5\cos^3 S - 3\cos S)$
4	$1/8\,(35\cos^4 S - 30\cos^2 S + 3)$

Table 3.1: Legendre polynomials $P_n(\cos S)$ from order 0 to 4.

Note that in Eq. (3.32) the term $n = 1$ and the right term cancel each other, while the term $n = 0$ is useless since it does not depend on r. In fact, the equation of motion depends on the gradient of $\mathcal{R}_{3b}$, meaning that the contribution of the zero term to the motion is null. Hence the final expression of the third-body potential:

$$\mathcal{R}_{3b} = \frac{\mu_{3b}}{r_{3b}} \sum_{n=2}^{\infty} \left(\frac{r}{r_{3b}}\right)^n P_n(\cos S) \tag{3.33}$$

In this work, as suggested in Colombo et al. [38] and done in previous studies [31] [30], only terms up to the fourth order will be considered since those are sufficient to accurately model the orbital evolution of a spacecraft in HEO.

The expressions of $\mathcal{R}_{3b,2}$, $\mathcal{R}_{3b,3}$ and $\mathcal{R}_{3b,4}$ are then retrieved:

$$\mathcal{R}_{3b,2} = \frac{1}{2}\frac{\mu_{3b}}{r_{3b}} \left(\frac{r}{r_{3b}}\right)^2 \left(3\cos^2 S - 1\right) \tag{3.34}$$

$$\mathcal{R}_{3b,3} = \frac{1}{2}\frac{\mu_{3b}}{r_{3b}} \left(\frac{r}{r_{3b}}\right)^3 \left(5\cos^3 S - 3\cos S\right) \tag{3.35}$$

$$\mathcal{R}_{3b,4} = \frac{1}{8}\frac{\mu_{3b}}{r_{3b}} \left(\frac{r}{r_{3b}}\right)^4 \left(35\cos^4 S - 30\cos^2 S + 3\right) \tag{3.36}$$

The term $\cos S$ needs to be specified. Its definition is:

$$\cos S = \frac{\mathbf{r} \cdot \mathbf{r}_{3b}}{r r_{3b}} = \hat{\mathbf{r}} \cdot \hat{\mathbf{r}}_{3b} \tag{3.37}$$

For the continuation of the work, Eq. (3.37) shall be expressed in terms of orbital elements.

Firstly, the vector in the perifocal frame is expressed in the perifocal frame $\{\hat{\mathbf{P}}, \hat{\mathbf{Q}}, \hat{\mathbf{R}}\}$ (see Section 2.3.1):

$$\mathbf{r} = r\cos\theta\ \hat{\mathbf{P}} + r\sin\theta\ \hat{\mathbf{Q}} \tag{3.38}$$

Dividing by the magnitude, a unitary vector is obtained:

$$\hat{\mathbf{r}} = \cos\theta\ \hat{\mathbf{P}} + \sin\theta\ \hat{\mathbf{Q}} \tag{3.39}$$

Following the method in Kaufman [8], inserting Eq. (3.39) into Eq. (3.37) gives:

$$\cos S = \hat{\mathbf{r}} \cdot \hat{\mathbf{r}}_{3b} = \left(\hat{\mathbf{P}} \cdot \hat{\mathbf{r}}_{3b}\right)\cos\theta + \left(\hat{\mathbf{Q}} \cdot \hat{\mathbf{r}}_{3b}\right)\sin\theta = A_{3b}\cos\theta + B_{3b}\sin\theta \tag{3.40}$$

Defining A_{3b} and B_{3b} as:

$$\begin{aligned} A_{3b} &= \hat{\mathbf{P}} \cdot \hat{\mathbf{r}}_{3b} \\ B_{3b} &= \hat{\mathbf{Q}} \cdot \hat{\mathbf{r}}_{3b} \end{aligned} \tag{3.41}$$

The same reasoning can be applied to $\hat{\mathbf{r}}_{3b}$, hence by decomposing it into its perifocal components, Eq. (3.40) can be rewritten as:

$$\begin{aligned} \cos S = &\left[\left(\hat{\mathbf{P}} \cdot \hat{\mathbf{P}}_{3b}\right)\cos\theta_{3b} + \left(\hat{\mathbf{P}} \cdot \hat{\mathbf{Q}}_{3b}\right)\sin\theta_{3b}\right]\cos\theta + ... \\ &+ \left[\left(\hat{\mathbf{Q}} \cdot \hat{\mathbf{P}}_{3b}\right)\cos\theta_{3b} + \left(\hat{\mathbf{Q}} \cdot \hat{\mathbf{Q}}_{3b}\right)\sin\theta_{3b}\right]\sin\theta \end{aligned} \tag{3.42}$$

Defining the following terms:

$$\begin{aligned} \alpha &= \hat{\mathbf{P}} \cdot \hat{\mathbf{P}}_{3b} \\ \beta &= \hat{\mathbf{Q}} \cdot \hat{\mathbf{Q}}_{3b} \\ \gamma &= \hat{\mathbf{P}} \cdot \hat{\mathbf{Q}}_{3b} \\ \xi &= \hat{\mathbf{Q}} \cdot \hat{\mathbf{P}}_{3b} \end{aligned} \tag{3.43}$$

Finally, it is possible to write:

$$\cos S = (\alpha \cos \theta_{3b} + \gamma \sin \theta_{3b}) \cos \theta + (\xi \cos \theta_{3b} + \beta \sin \theta_{3b}) \sin \theta \tag{3.44}$$

The dependency of A_{3b}, B_{3b}, α, β, γ and ξ on the orbital elements of either the satellite and the third body are reported in Table 3.2

Term	Dependency
A_{3b}, B_{3b}	$\{i,\ \Omega,\ \omega,\ i_{3b},\ \Omega_{3b},\ \omega_{3b},\ \theta_{3b}\}$
α, β, γ, ξ	$\{i,\ \Omega,\ \omega,\ i_{3b},\ \Omega_{3b},\ \omega_{3b}\}$

Table 3.2: Dependency of various terms on the orbital elements.

The explicit dependency on θ_{3b} in Eq. (3.44) will be useful later on for the double averaging procedure in Section 3.2.2.

The third-body potential from Eq. (3.33) in its full complexity depends on all the orbital elements of both the spacecraft and the third body perturber:

$$\mathcal{R}_{3b} = \mathcal{R}_{3b}\left(a, e, i, \Omega, \omega, \theta, a_{3b}, e_{3b}, i_{3b}, \Omega_{3b}, \omega_{3b}, \theta_{3b}\right) \tag{3.45}$$

To access the phase space and simultaneously speed up the computation of the orbital evolution of a satellite, some averaging procedures of the third body disturbing function are carried out using Mathematica® software.

3.2.1. Single Average

Since the short-term variations are not of interest in studying the long-term dynamics of a satellite, the first averaging aims at cancelling the highest frequency harmonic of the orbital elements evolution, which is associated with the position of the satellite along its orbit. This is done by averaging over the satellite's mean anomaly M.
Note that in this procedure, since the focus is the long-term behaviour, the orbital elements are considered constants throughout the averaging operation.
The Single Average (SA) is hence retrieved from:

$$\overline{\mathcal{R}}_{3b} = \frac{1}{2\pi} \int_0^{2\pi} \mathcal{R}_{3b} dM \tag{3.46}$$

Recalling from Eq. (3.13) that dM can be expressed in terms of θ, the integral can be computed over the satellite's true anomaly θ.

To simplify the computation procedure, the integration is carried out independently for the second, third and fourth-order terms.

Second order term $\overline{\mathcal{R}}_{3b,2}$

Substituting Eq. (3.40) inside Eq. (3.34) the second order term of the third body potential is:

$$\mathcal{R}_{3b,2} = \frac{\mu_{3b}}{4}\frac{r^2}{r_{3b}^3}\left[-2 + 3\left(A_{3b}^2 + B_{3b}^2\right) + 3\left(A_{3b}^2 - B_{3b}^2\right)\cos 2\theta + 6A_{3b}^2 B_{3b}^2 \sin 2\theta\right] \tag{3.47}$$

The SA procedure considering only the second-order terms expression is given by inserting Eq. (3.47) into Eq. (3.56). Following the procedure from Kaufman [8]. recalling Eqs. (2.6), (3.13) the SA computation of the second order term is subdivided into several integrals by collecting the terms dependent on $\sin 2\theta$, $\cos 2\theta$. In this way, the software can easily retrieve the results:

$$\begin{aligned}\frac{1}{2\pi}\int_0^{2\pi} r^2 dM &= \frac{1}{2}a^2(2+3e^2)\\ \frac{1}{2\pi}\int_0^{2\pi} r^2 \cos 2\theta dM &= \frac{5}{2}a^2e^2\\ \frac{1}{2\pi}\int_0^{2\pi} r^2 \sin 2\theta dM &= 0\end{aligned} \tag{3.48}$$

The three terms are then substituted in Eq. (3.47) and the SA expression is:

$$\overline{\mathcal{R}}_{3b,2} = \frac{\mu_{3b}}{4}\frac{a^2}{r_{3b}^3}\left[(-2 - 3e^2 - 3B_{3b}^2(-1+e^2) + 3A_{3b}^2(1+4e^2)\right] \tag{3.49}$$

Third order term $\overline{\mathcal{R}}_{3b,3}$

The same procedure applied for the second order term is applied for the third order term, which is given by substituting Eq. (3.40) inside Eq. (3.35):

$$\begin{aligned}\mathcal{R}_{3b,3} =& \frac{\mu_{3b}}{8}\frac{r^3}{r_{3b}^4}\Big\{3A_{3b}(-4+5A_{3b}^2+5B_{3b}^2)\cos\theta+5A_{3b}(A_{3b}^2-3B_{3b}^2)\cos 3\theta+...\\ &-2B_{3b}\left[6-15A_{3b}^2-5B_{3b}^2+5(-3_{3b}^2+B_{3b}^2)\cos 2\theta\right]\sin\theta\Big\}\end{aligned} \tag{3.50}$$

The SA averaging to be applied is the following is given by insertin Eq. (3.50) into Eq. (3.56). And again, using Eqs. (2.6), (3.13), the computation is divided into the following terms:

$$\begin{aligned}&\frac{1}{2\pi}\int_0^{2\pi} r^3\cos\theta\; dM = -\frac{5}{8}a^3e(4+3e^2)\\ &\frac{1}{2\pi}\int_0^{2\pi} r^3\cos 3\theta\; dM = -\frac{35}{8}a^3e^3\\ &\frac{1}{2\pi}\int_0^{2\pi} r^3\sin\theta\; dM = 0\\ &\frac{1}{2\pi}\int_0^{2\pi} r^3\cos 2\theta\sin\theta\; dM = 0\end{aligned} \tag{3.51}$$

which substituted in Eq. (3.50), gives the SA expression:

$$\overline{\mathcal{R}}_{3b,3} = -\frac{5}{16}\frac{a^3}{r_{3b}^4}\mu_{3b}A_{3b}e\Big\{5A_{3b}^2(3+4e^2)-3\left[4+3e^2+5B_{3b}^2(-1+e^2)\right]\Big\} \tag{3.52}$$

Fourth order term $\overline{\mathcal{R}}_{3b,4}$

Same procedure once again, the fourth order term from Eq. (3.40) substituted in Eq. (3.36) gives:

$$\begin{aligned}
\mathcal{R}_{3b,4} =& \frac{\mu_{3b}}{64}\frac{r^4}{r_{3b}^5}\big[24 - 120A_{3b}^2 + 105A_{3b}^4 - 120B_{3b}^2 + 210A_{3b}^2B_{3b}^2 + ... \\
& + 105B_{3b}^4 + 20(-6A_{3b}^2 + 7A_{3b}^4 + 6B_{3b}^2 - 7B_{3b}^4)\cos 2\theta + ... \\
& + 35(A_{3b}^4 - 6A_{3b}^2B_{3b}^2 + B_{3b}^4)\cos 4\theta + ... \\
& + A_{3b}B_{3b}(-240 + 280A_{3b}^2 + 280B_{3b}^2)\sin 2\theta + ... \\
& + (140A_{3b}^3B_{3b} - 140A_{3b}B_{3b}^3)\sin 4\theta\big]
\end{aligned} \tag{3.53}$$

The fourth-order SA is then computed by inserting Eq. (3.53) into Eq. (3.56), and using Eqs. (2.6), (3.13). The averaging is here carried out in the following terms:

$$\begin{aligned}
\frac{1}{2\pi}\int_0^{2\pi} r^4 dM &= \frac{1}{8}a^4(8 + 40e^2 + 15e^4) \\
\frac{1}{2\pi}\int_0^{2\pi} r^4 \cos 2\theta \; dM &= \frac{21}{8}a^4e^2(2 + e^2) \\
\frac{1}{2\pi}\int_0^{2\pi} r^4 \cos 4\theta \; dM &= \frac{63}{8}a^4e^4 \\
\frac{1}{2\pi}\int_0^{2\pi} r^4 \sin 2\theta \; dM &= 0 \\
\frac{1}{2\pi}\int_0^{2\pi} r^3 \sin 4\theta \; dM &= 0
\end{aligned} \tag{3.54}$$

Hence the final expression of the fourth order SA third body potential is obtained:

$$\begin{aligned}
\overline{\mathcal{R}}_{3b,4} =& \frac{3}{64}\frac{a^4}{r_{3b}^5}\mu_{3b}\bigg\{8 + 40e^2 + 15e^4 + 35B_{3b}^4(-1 + e^2)^2 + ... \\
& + 10B_{3b}^2(-4 + e^2 + 3e^4) + 35A_{3b}^4(1 + 12e^2 + 8e^4) + ... \\
& - 10A_{3b}^2\left[4 + 41e^2 + 18e^4 + 7B_{3b}^2(-1 - 5e^2 + 6e^4)\right]\bigg\}
\end{aligned} \tag{3.55}$$

The resulting overall third body potential is given by the sum of the individual order terms computed separately:

$$\overline{\mathcal{R}}_{3b} = \sum_{i=2}^{4} \overline{\mathcal{R}}_{3b,i} \tag{3.56}$$

3.2.2. Double average

Since in this work scenario, the timescale of the orbital elements' long-time oscillation still dominates the shorter period of the third-body motion, a further averaging operation is carried out.

The Double Average (DA) consists of integrating the SA over the third body's mean anomaly M_{3b}, expressed in terms of θ_{3b}, in a similar fashion to the aforementioned SA. The general expression is therefore given by:

$$\overline{\overline{\mathcal{R}}}_{3b} = \frac{1}{2\pi} \int_0^{2\pi} \overline{\mathcal{R}}_{3b} dM_{3b} \tag{3.57}$$

As done previously, the integration is retrieved from each order term independently.

Second order term $\overline{\overline{\mathcal{R}}}_{3b,2}$

The expression for the second-order term DA is given by inserting Eq. (3.47) into Eq. (3.57). This time, since the dependence on the true anomaly θ_{3b} is embedded inside the terms A_{3b}, B_{3b} as depicted in Table 3.2, the expression from Eq. (3.44) is used to carry out the averaging computation, having $A_{3b} = \alpha \cos \theta_{3b} + \gamma \sin \theta_{3b}$ and $B_{3b} = \xi \cos \theta_{3b} + \beta \sin \theta_{3b}$. At this point recalling Eqs. (2.6), (3.13), the integration is carried out by collecting the following terms from Eq. (3.49):

$$\begin{aligned}
\frac{1}{2\pi} \int_0^{2\pi} \frac{1}{r_{3b}^3} dM_{3b} &= \frac{1}{a_{3b}^3 (1 - e_{3b}^2)^{3/2}} \\
\frac{1}{2\pi} \int_0^{2\pi} \frac{A_{3b}^2}{r_{3b}^3} dM_{3b} &= \frac{1}{2} \frac{\alpha^2 + \gamma^2}{a_{3b}^3 (1 - e_{3b}^2)^{3/2}} \\
\frac{1}{2\pi} \int_0^{2\pi} \frac{B_{3b}^2}{r_{3b}^3} dM_{3b} &= \frac{1}{2} \frac{\beta^2 + \xi^2}{a_{3b}^3 (1 - e_{3b}^2)^{3/2}}
\end{aligned} \tag{3.58}$$

The second order term of the DA is hence retrieved:

$$\overline{\overline{\mathcal{R}}}_{3b,2} = \frac{\mu_{3b}}{8} \frac{a^2}{a_{3b}^3 (1 - e_{3b}^2)^{3/2}} \left[-4 - 6e^2 + 3(\xi^2 + \beta^2)(1 - e^2) + 3(\alpha^2 + \gamma^2)(1 + 4e^2)\right] \tag{3.59}$$

Third order term $\overline{\overline{\mathcal{R}}}_{3b,3}$

Using the same procedure, the third-order term DA can be computed starting from its integration expression, inserting Eq. (3.50) into Eq. (3.57). At this point, using Eqs. (2.6), (3.13), and exploiting the dependency on θ_{3b} with Eq. (3.44) as done before, the integration is split collecting the following terms from Eq. (3.52):

$$\begin{aligned}
\frac{1}{2\pi}\int_0^{2\pi}\frac{A_{3b}^3}{r_{3b}^4}dM_{3b} &= \frac{3}{4}e_{3b}\frac{\alpha(\alpha^2+\gamma^2)}{a_{3b}^4(1-e_{3b}^2)^{5/2}}\\
\frac{1}{2\pi}\int_0^{2\pi}\frac{A_{3b}B_{3b}^2}{r_{3b}^4}dM_{3b} &= \frac{1}{4}e_{3b}\frac{\alpha(\beta^2+3\xi^2)+2\beta\xi\gamma}{a_{3b}^4(1-e_{3b}^2)^{5/2}}\\
\frac{1}{2\pi}\int_0^{2\pi}\frac{A_{3b}}{r_{3b}^4}dM_{3b} &= e_{3b}\frac{\alpha}{a_{3b}^4(1-e_{3b}^2)^{5/2}}
\end{aligned} \tag{3.60}$$

Which gives as the result the third order DA disturbing function:

$$\begin{gathered}
\overline{\overline{\mathcal{R}}}_{3b,3} = -\frac{15}{64}\frac{a^3}{a_{3b}^4(1-e_{3b}^2)^{5/2}}\mu_{3b}ee_{3b}\Big\{5\alpha^3(3+4e^2)-10\beta\xi\gamma(-1+e^2)+\\
\alpha\big[-4(4+3e^2)+5(\beta^2+3\xi^2)(1-e^2)+5\gamma^2(3+4e^2)\big]\Big\}
\end{gathered} \tag{3.61}$$

Note that $\overline{\overline{\mathcal{R}}}_{3b,3}$ has a linear dependece on the third-body eccentricity e_{3b}. This means that if the perturber orbit is circular, then the third-order term of the DA potential is null:

$$\overline{\overline{\mathcal{R}}}_{3b,3}\Big|_{e_{3b}=0} = 0 \tag{3.62}$$

Fourth order term $\overline{\overline{\mathcal{R}}}_{3b,4}$

Same procedure once again, starting from the integration given by combining Eq. (3.53) and Eq. (3.57). Using Eqs. (2.6), (3.13) and by expliciting the dependency on θ_{3b} with Eq. (3.44), the following terms are collected and then integrated from Eq. (3.55):

$$
\begin{aligned}
&\frac{1}{2\pi}\int_0^{2\pi}\frac{1}{r_{3b}^5}dM_{3b} = \frac{1}{2}\frac{2+3e_{3b}^2}{a_{3b}^5(1-e_{3b}^2)^{7/2}}\\
&\frac{1}{2\pi}\int_0^{2\pi}\frac{B_{3b}^4}{r_{3b}^5}dM_{3b} = \frac{3}{16}(\beta^2+\xi^2)\frac{\beta^2(2+e_{3b}^2)+\xi^2(2+5e_{3b}^2)}{a_{3b}^5(1-e_{3b}^2)^{7/2}}\\
&\frac{1}{2\pi}\int_0^{2\pi}\frac{B_{3b}^2}{r_{3b}^5}dM_{3b} = \frac{1}{8}\frac{\beta^2(4+3e_{3b}^2)+\xi^2(4+9e_{3b}^2)}{a_{3b}^5(1-e_{3b}^2)^{7/2}}\\
&\frac{1}{2\pi}\int_0^{2\pi}\frac{A_{3b}^4}{r_{3b}^5}dM_{3b} = \frac{3}{16}(\alpha^2+\gamma^2)\frac{\alpha^2(2+5e_{3b}^2)+\gamma^2(2+e_{3b}^2)}{a_{3b}^5(1-e_{3b}^2)^{7/2}}\\
&\frac{1}{2\pi}\int_0^{2\pi}\frac{A_{3b}^2}{r_{3b}^5}dM_{3b} = \frac{1}{8}\frac{\alpha^2(4+9e_{3b}^2)+\gamma^2(4+3e_{3b}^2)}{a_{3b}^5(1-e_{3b}^2)^{7/2}}\\
&\frac{1}{2\pi}\int_0^{2\pi}\frac{A_{3b}^2B_{3b}^2}{r_{3b}^5}dM_{3b} = \frac{1}{16}\frac{1}{a_{3b}^5(1-e_{3b}^2)^{7/2}}\Big\{-\alpha^2\big[\beta^2(2+3e_{3b}^2)+\dots\\
&\qquad +3\xi^2(2+5e_{3b}^2)\big]-4\alpha\beta\xi\gamma(2+3e_{3b}^2)+\dots\\
&\qquad -\gamma^2\big[3\beta^2(2+e_{3b}^2)+\xi^2(2+3e_{3b}^2)\big]\Big\}
\end{aligned}
\tag{3.63}
$$

which brings to the last considered term of the DA's third body disturbing function:

$$
\begin{aligned}
\overline{\overline{\mathcal{R}}}_{3b,4} =& \frac{3}{1024}\frac{a^4}{a_{3b}^5(1-e_{3b}^2)^{7/2}}\mu_{3b}\Big\{8(8+40e^2+15e^4)(2+3e_{3b}^2)+\dots\\
&+105(\beta^2+\xi^2)(-1+e^2)^2\big[\beta^2(2+e_{3b}^2)+\xi^2(2+5e_{3b}^2)\big]+\dots\\
&+20(-4+e^2+3e^4)\big[\beta^2(4+3e_{3b}^2)+\xi^2(4+9e_{3b}^2)\big]+\dots\\
&+105(1+12e^2+8e^4)(\alpha^2+\gamma^2)\big[\alpha^2(2+5e_{3b}^2)+\gamma^2(2+e_{3b}^2)\big]+\dots\\
&-20(4+41e^2+18e^4)\big[\alpha^2(4+9e_{3b}^2)+\gamma^2(4+3e_{3b}^2)\big]+\dots\\
&+70(-1-5e^2+6e^4)\big\{-\alpha^2\big[\beta^2(2+3e_{3b}^2)+3\xi^2(2+5e_{3b}^2)\big]+\dots\\
&-4\alpha\beta\xi\gamma(2+3e_{3b}^2)-\gamma^2\big[3\beta^2(2+e_{3b}^2)+\xi^2(2+3e_{3b}^2)\big]\big\}\Big\}
\end{aligned}
\tag{3.64}
$$

At this point, collecting all the terms up to the fourth order, the expression of the DA third-body potential is given by:

$$\overline{\overline{\overline{\mathcal{R}}}}_{3b} = \sum_{i=2}^{4} \overline{\overline{\overline{\mathcal{R}}}}_{3b,i} \tag{3.65}$$

3.2.3. Triple average

Following the same procedure used in Section 3.1.2, some conditions must be met. While the Hamiltonian independence on the fast angle M has been accomplished through the SA procedure, the potential obtained with the DA integration still exhibits a dependence on the node Ω. The Triple Average (TA) requires an integration over the satellite right ascension of the ascending node Ω. This will remove as a consequence the dependence on the third body Ω_{3b} as well, since the two are coupled. The general expression is:

$$\overline{\overline{\overline{R}}}_{3b,2} = \frac{1}{2\pi} \int_0^{2\pi} \overline{\overline{\mathcal{R}}}_{3b,2} d\Omega \tag{3.66}$$

In this way, the potential does not depend anymore on the satellite node but note that this does not mean being autonomous since the implicit time dependence of the third-body orbital elements is not faced in this operation.

Second order term $\overline{\overline{\overline{R}}}_{3b,2}$

Using Eqs. (2.6), (3.13) and by expliciting the dependency on θ_{3b} with Eq. (3.44), for the second order term the integration is carried out in those terms:

$$\begin{aligned}
\frac{1}{2\pi}\int_0^{2\pi} \xi^2 + \beta^2 d\Omega =& \frac{1}{32}\Big\{22 + 2\cos 2i + 3\cos\left(2(i - i_{3b})\right) + 2\cos 2i_{3b} + \ldots \\
&+ 3\cos\left(2(i + i_{3b})\right) - 4\left(1 + 3\cos 2i_{3b}\right)\cos 2\omega \sin^2 i\Big\} \\
\frac{1}{2\pi}\int_0^{2\pi} \alpha^2 + \beta^2 d\Omega =& \frac{1}{32}\Big\{22 + 2\cos 2i + 3\cos\left(2(i - i_{3b})\right) + 2\cos 2i_{3b} + \ldots \\
&+ 3\cos\left(2(i + i_{3b})\right) + 4\left(1 + 3\cos 2i_{3b}\right)\cos 2\omega \sin^2 i\Big\}
\end{aligned} \tag{3.67}$$

The second-order term of the TA potential is then retrieved:

$$\begin{aligned}
\overline{\overline{\overline{\mathcal{R}}}}_{3b,2} = \frac{\mu_{3b}}{128} \frac{a^2}{a_{3b}^3(1 - e_{3b}^2)^{3/2}} \left(1 + 3\cos 2i_{3b}\right) \Big[&(2 + 3e^2)(1 + 3\cos 2i) + \ldots \\
&+ 30e^2 \cos 2\omega \sin^2 i \Big]
\end{aligned} \tag{3.68}$$

Third order term $\overline{\overline{\overline{R}}}_{3b,3}$

For the third order, using Eqs. (2.6), (3.13) and by expliciting the dependency on θ_{3b} with Eq. (3.44):

$$
\begin{gathered}
\frac{1}{2\pi}\int_0^{2\pi}\alpha^3 d\Omega \\
\frac{1}{2\pi}\int_0^{2\pi}\beta\gamma\xi d\Omega \\
\frac{1}{2\pi}\int_0^{2\pi}\alpha d\Omega \\
\frac{1}{2\pi}\int_0^{2\pi}\alpha\beta^2 d\Omega \\
\frac{1}{2\pi}\int_0^{2\pi}\alpha\gamma^2 d\Omega \\
\frac{1}{2\pi}\int_0^{2\pi}\alpha\xi^2 d\Omega
\end{gathered}
\tag{3.69}
$$

The results of the integration are reported in Appendix A due to their complexity. Those can be then recollected into the expression of the third-order term of the TA potential:

$$
\begin{aligned}
\overline{\overline{\overline{\mathcal{R}}}}_{3b,3} = -\frac{15}{2048}\frac{a^3}{a_{3b}^4(1-e_{3b}^2)^{5/2}}\mu_{3b}ee_{3b}\sin i\Big[18+31e^2+\ldots \\
5(6+e^2)\cos 2i+70e^2\cos 2\omega\sin^2 i\Big]\Big(\sin i_{3b}+\ldots \\
5\sin 3i_{3b}\Big)\sin\omega\sin\omega_{3b}
\end{aligned}
\tag{3.70}
$$

Note that also this time is present a linear dependence on the third-body eccentricity e_{3b}. This means that once again if the perturber orbit is circular, the third-order term of the TA potential is null:

$$
\overline{\overline{\overline{\mathcal{R}}}}_{3b,3}\Bigg|_{e_{3b}=0} = 0 \tag{3.71}
$$

Fourth order term $\overline{\overline{\overline{R}}}_{3b,4}$

Lastrly, the fourth order term is computed from the general TA procedure. Using Eqs. (2.6), (3.13) and by expliciting the dependency on θ_{3b} with Eq. (3.44):

$$\begin{gathered}
\frac{1}{2\pi}\int_0^{2\pi} 1 d\Omega \\
\frac{1}{2\pi}\int_0^{2\pi} (\beta^2+\xi^2)\beta^2 d\Omega \\
\frac{1}{2\pi}\int_0^{2\pi} (\beta^2+\xi^2)\xi^2 d\Omega \\
\frac{1}{2\pi}\int_0^{2\pi} \beta^2 d\Omega \\
\frac{1}{2\pi}\int_0^{2\pi} \xi^2 d\Omega \\
\frac{1}{2\pi}\int_0^{2\pi} (\alpha^2+\gamma^2)\alpha^2 d\Omega \\
\frac{1}{2\pi}\int_0^{2\pi} (\alpha^2+\gamma^2)\gamma^2 d\Omega \\
\frac{1}{2\pi}\int_0^{2\pi} \alpha^2 d\Omega \\
\frac{1}{2\pi}\int_0^{2\pi} \gamma^2 d\Omega \\
\frac{1}{2\pi}\int_0^{2\pi} \alpha^2\beta^2 d\Omega \\
\frac{1}{2\pi}\int_0^{2\pi} \alpha^2\xi^2 d\Omega \\
\frac{1}{2\pi}\int_0^{2\pi} \alpha\beta\xi\gamma d\Omega \\
\frac{1}{2\pi}\int_0^{2\pi} \gamma^2\beta^2 d\Omega \\
\frac{1}{2\pi}\int_0^{2\pi} \gamma^2\xi^2 d\Omega
\end{gathered} \tag{3.72}$$

Again, due to the length and the number of the integration results, they are reported in Appendix A. Those operations lead to the final expression of the fourth-order term of the TA potential:

$$\begin{aligned}\overline{\overline{\overline{\mathcal{R}}}}_{3b,4} =& \frac{9}{4194304} \frac{a^4 \mu_{3b}}{a_{3b}^5 (1-e_{3b}^2)^{7/2}} \Bigg[(8+40e^2+15e^4)(9+20\cos 2i + 35 \cos 4i) + ... \\ &+ 560 e^2 (2+e^2)(5+7\cos 2i)\cos 2\omega \sin^2 i + ... \\ &+ 5880 e^4 \cos 4\omega \sin^4 i \Bigg] \Bigg[(2+3e_{3b}^2)(9+20\cos 2i_{3b} + 35 \cos 4i_{3b}) + ... \\ &+ 40 e_{3b}^2 (5+7\cos 2i_{3b}) \cos 2\omega_{3b} \sin^2 i_{3b} \Bigg]\end{aligned} \tag{3.73}$$

The final expression of the overall TA potential up to the fourth order is given by the sum of the individually integrated terms:

$$\overline{\overline{\overline{\mathcal{R}}}}_{3b} = \sum_{i=2}^{4} \overline{\overline{\overline{\mathcal{R}}}}_{3b,i} \tag{3.74}$$

Two considerations can be made:

- by eliminating the node Ω, as expected, also the dependence on the third-body Ω_{3b} is removed. This happens because, in the DA potential, the two variables are coupled. An appropriate reorganization of Eq. (3.65) can highlight this.
- as mentioned before, the implicit time dependence is still embedded in the third-body orbital elements. Looking at the TA potential terms, the set $\{a_{3b}, e_{3b}, i_{3b}, \omega_{3b}\}$ can vary as time progresses. In the Moon case, variations are noticeable in the Euler angles $\{i_{3b}, \omega_{3b}\}$.

Given the latter observation, in Asperti [30] and Scala [31], an additional simplification is added by considering the third-body orbital elements as constants, finally obtaining the result needed for the phase space representation.

In this work, however, an algorithm for the disposal manoeuvre will be investigated without making this final assumption. The final Hamiltonian will hence be a time-dependent function:

$$\mathcal{H} = \mathcal{H}\left(e, \omega, t\right) \tag{3.75}$$

3.3. Hamiltonian formulation and phase space

To express the dynamics in a planar phase space, which can be very insightful in the study of the end-of-life procedures for a satellite, the Hamiltonian formulation will be used as a compact formalism to model the dynamic evolution of the system under study. This requires the definition of the Hamiltonian $\mathcal{H}$, a scalar function that embeds that information.

3.3.1. Hamiltonian formulation

Following the description from Kartunnen, The Hamiltonian can be described as the Legendre transformation of the Lagrangian $\mathcal{L}$:

$$\mathcal{H} = \mathcal{H}\left(q_i, p_i, t\right) := \sum_{i=1}^{n} p_i \dot{q}_i - \mathcal{L}\left(q_1, .., q_n, \dot{q}_1, ..., \dot{q}_n, t\right) \tag{3.76}$$

where the parameters q_i represents the generalised coordinates, with n DoFs. From there, the following relations can be written:

$$\begin{aligned} \dot{q}_i &= \frac{\partial \mathcal{H}}{\partial p_i} \\ \dot{p}_i &= -\frac{\partial \mathcal{H}}{\partial q_i} \end{aligned} \tag{3.77}$$

It is also possible to demonstrate that the Hamiltonian is equal to the total energy of the system, which in the perturbed two-body problem considered in this thesis, becomes:

$$\mathcal{H} = \mathcal{K} - \mathcal{R} = -\frac{\mu}{2a} - \mathcal{R}_{J_2} - \mathcal{R}_{\odot} - \mathcal{R}_{☾} \tag{3.78}$$

where $\mathcal{R}_{\odot}$ and $\mathcal{R}_{☾}$ are respectively referred to the Sun and the Moon. The potential the perturbations considered are valid for a HEO scenario, taking into account the zonal gravitational perturbation J_2 and the third body perturbation potentials of both the Sun and Moon discussed in Sections 3.1 and 3.2.

For Eq. (3.77) to be valid, a canonical set of variables shall be used instead of the usual orbital elements $\{a, e, i, \Omega, \omega, \theta\}$. Delauney variables are widely adopted to this extent. They are reported in Table 3.3.

q_i		p_i	
L	$\sqrt{\mu a}$	l	M
G	$L\sqrt{1-e^2}$	g	ω
H	$G\cos i$	h	Ω

Table 3.3: Delaunay variables definition.

From Eq. (3.77), given a coupled pair of conjugate variables $\{q_i, p_i\}$, if the Hamiltonian $\mathcal{H}$ does not depend on one of them, the other is constant. Mathematically it reads as:

$$\begin{aligned} &\frac{\partial \mathcal{H}}{\partial p_i} \quad \rightarrow \quad \dot{q}_i = 0 \\ &\frac{\partial \mathcal{H}}{\partial q_i} \quad \rightarrow \quad \dot{p}_i = 0 \end{aligned} \tag{3.79}$$

The most interesting relations that follows from Eq. (3.79) and will be exploited are:

- When $\mathcal{H}$ does not depend on M, the semi-major axis a is constant.
- When $\mathcal{H}$ does not depend on Ω, the Delaunay variable H is constant, hence $\sqrt{\mu a\,(1-e^2)}\cos i = const.$

This is an important relation since it enables the possibility of exploiting the Hamiltonian formulation for a phase space representation. In fact, from the 6 DoFs highlighted in section 2.2, the problem can be reduced for a 2D representation with the following assumptions:

1. dependence on the mean anomaly M is dropped
2. dependence on the right ascension of the ascending node Ω is dropped

Recalling then Eq. (3.79) and Table (3.3), the two conditions lead respectively to:

1. from the first condition, the semi-major axis a is then constant.
2. the Delaunay variable H is constant. Considering also the first assumption, it is then possible to write:

$$\left(\frac{H}{L}\right)^2 = \left(1-e^2\right)\cos i = \Theta \tag{3.80}$$

   with Θ constant, being the Kozai parameter. [7].

Moreover, if the Hamiltonian is independent of time, $\mathcal{H}$ itself is constant.

Nonetheless, from Eq. (3.80), it is also possible to write the inclination i as a function of the eccentricity e, given the Kozai parameter conservation. The relation is:

$$i = \arccos\left(\sqrt{\frac{\Theta}{1-e^2}}\right) \tag{3.81}$$

therefore the Hamiltonian $\mathcal{H}$ can be represented as a function of only two variables: alternatively $\{e, \omega\}$ or $\{i, \omega\}$. Considering its conservation, the problem is reduced to a single DoF. This means that it is possible to represent the dynamics in a 2D map.

Given the possibilities offered by the Hamiltonian formulation, some remarks shall be pointed out:

- This theory relies on the absence of an explicit time-dependence of the Hamiltonian $\mathcal{H}$. This represents a simplification of the problem in the presence of the Moon as a third body, since its motion is characterised by a precession behaviour.
- The node elimination can introduce non-negligible errors in the orbit propagation. The results' fidelity with respect to more accurate methods must be checked.

However, in this thesis, an approach considering the Hamiltonian variation in time will be analysed.

3.3.2. Phase space

As aforementioned, the Hamiltonian formulation enables the possibility to express the dynamics in a simplified 2D phase space map, given some strong assumptions.

The evolution of the satellite is then represented with a single isoline of the Hamiltonian, representing the locus of all possible past and future states. In such a plot, the x and y axis are represented respectively by the eccentricity e and the argument of perigee ω.
A 3D representation in the $\{\omega, e, i\}$ space is also possible, recalling the relationship between the inclination i and e highlighted in Eq. (3.81),

Kozai Parameter

Once the boundary conditions represented by the perturbing effects are defined, only two variables will define the entire evolution of the satellite in this simplified framework:

- The semi-major axis a
- The Kozai parameter, defined in Eq. (3.80)

Once those are fixed, also the phase space topology is locked.
Following the theory developed by Kozai [7], in a single third-body perturber case, a limit value of the Kozai parameter $\Theta_{crit} = 0.6$ separates the stationary and libration regimes. In fact for a value below the critical one, a libration island is present, centred at $\omega = \pm\pi/2$. When multiple perturbers are present, the reasoning remains valid, but the value of Θ_{crit} varies depending on the scenario considered.

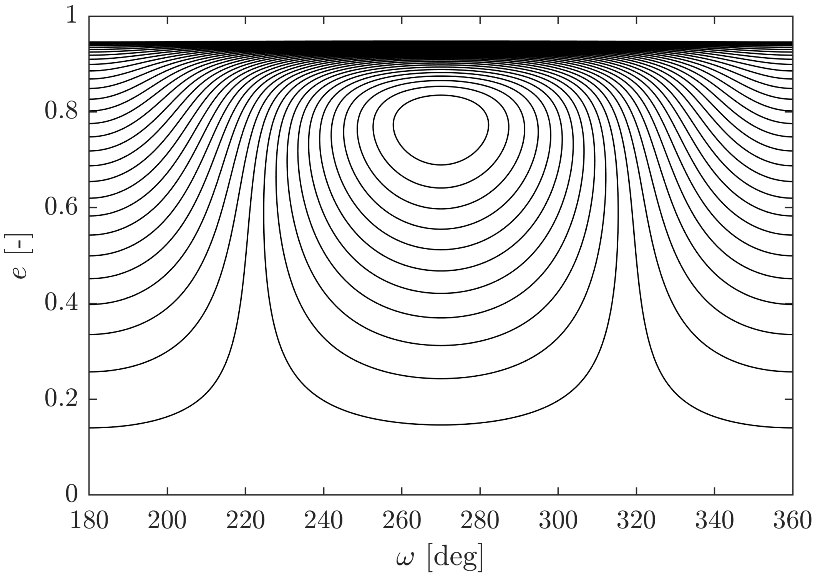

Figure 3.2: Phase space with $\Theta = 0.1$, libration regime.

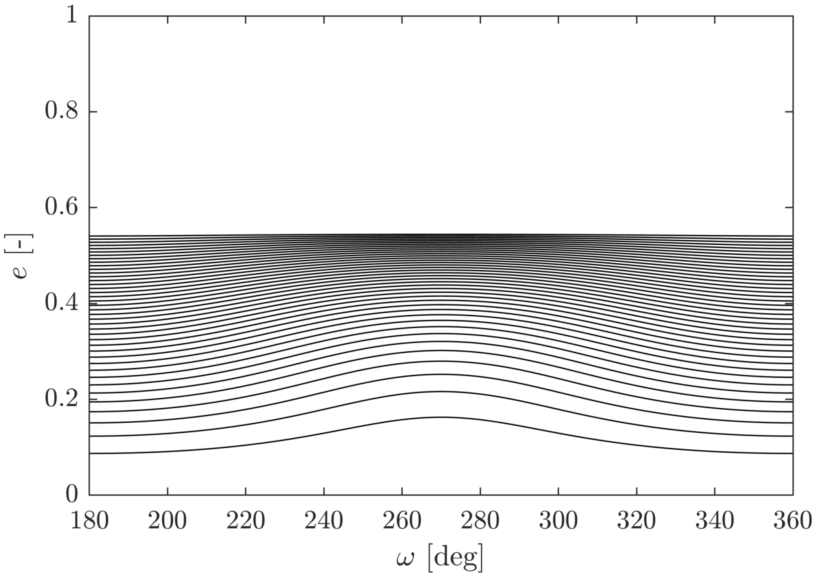

Figure 3.3: Phase space with $\Theta = 0.7$, stationary regime.

Another important complication is given by the J_2 perturbation, as highlighted by Delsate et al. [11], the zonal effect works as a stabilizer, contrasting the libration regime.

The libration regime can be exploited for manoeuvre planning, for example, to target either a re-entry or a graveyard orbit near the centre of the libration, where the maximum value of the eccentricity is reached.

Two examples of phase space representation are reported in Fig. 3.2 and Fig. 3.3, where the Kozai parameter is fixed respectively at $\Theta = 0.1$ and $\Theta = 0.7$. The Hamiltonian in those examples takes into account J_2 and the third body perturbations of both the Moon and the Sun. The semi-major axis is set as $a = 87,720$ km, considering the case of the INTEGRAL satellite that will be used in the models' validation in Chapter 4.

Maximum eccentricity

From Eq. 3.80, the maximum eccentricity that can be reached in the orbital evolution is limited by the following:

$$\cos i_{max} = \sqrt{\frac{\Theta}{1 - e_{max}^2}} = 1 \rightarrow e_{max} = \sqrt{1 - \Theta} \tag{3.82}$$

To target a re-entry by exploiting the phase space properties, a manoeuvre can be designed such that the Kozai parameter after the impulse admits a maximum eccentricity that is at least equal to the critical value:

$$e_{crit} = 1 - \frac{h_{p,tar} + R_{\oplus}}{a} = e_{max} = \sqrt{1 - \Theta} \tag{3.83}$$

with $R_{\oplus}$ being the Earth radius, while $h_{p,tar}$ is the target altitude for the re-entry. Note that also a can change after the impulse, modifying the topology of the phase space.

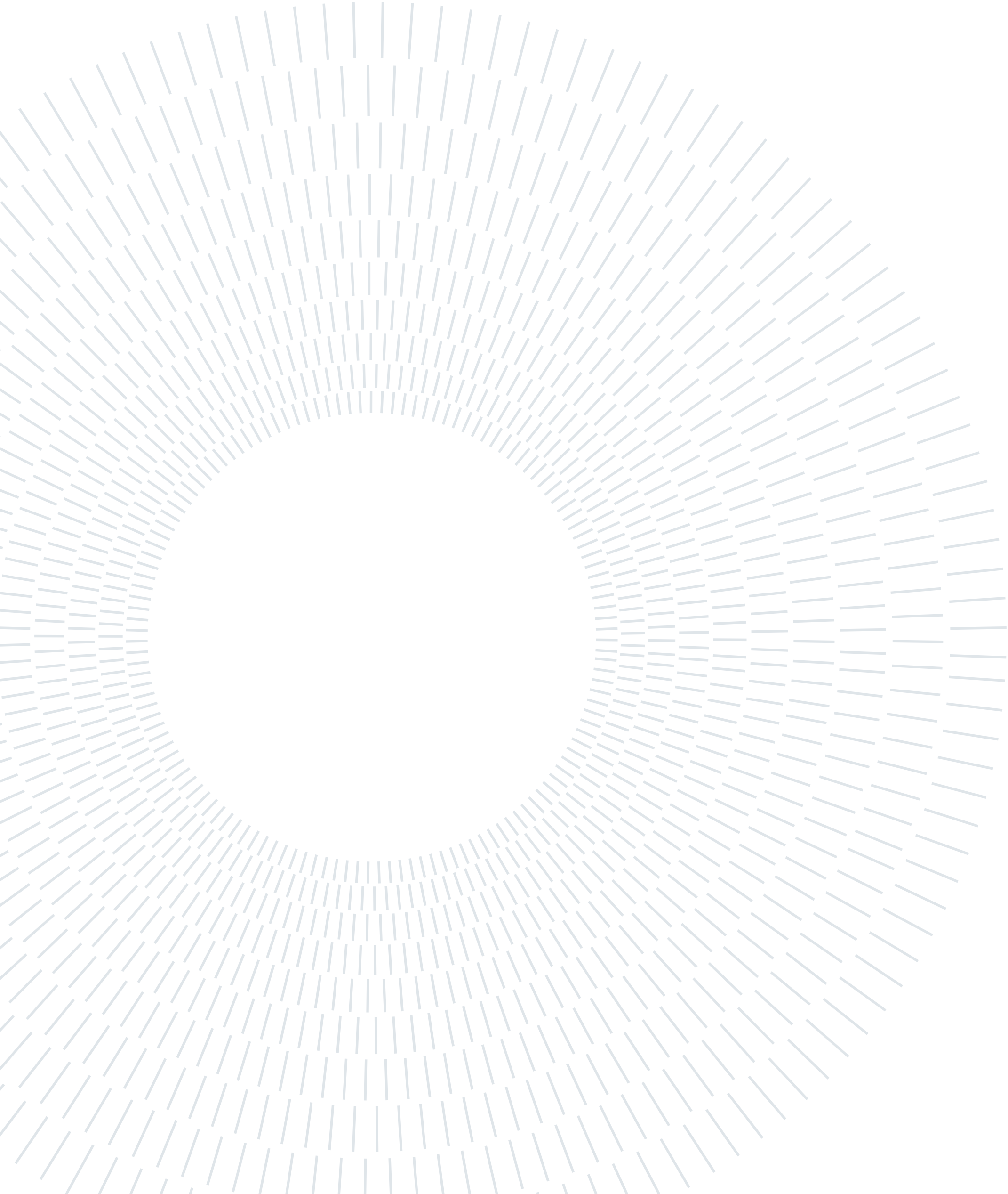

4 Model validation

4.1. Sun & Moon models

Firstly, the models used for the Sun and Moon orbital elements' evolution are presented since an accurate description is requested to characterize the third-body perturbations. Being this study focused on a spacecraft orbiting around the Earth in a HEO environment, the planetary attraction of these perturbers is non-negligible and is comparable in magnitude to the perturbation induced by the Earth's oblateness.
The two bodies' ephemerides evolution will be reported starting from 01/01/2000 until 01/01/2100, considering the ecliptic frame.

4.1.1. Sun model

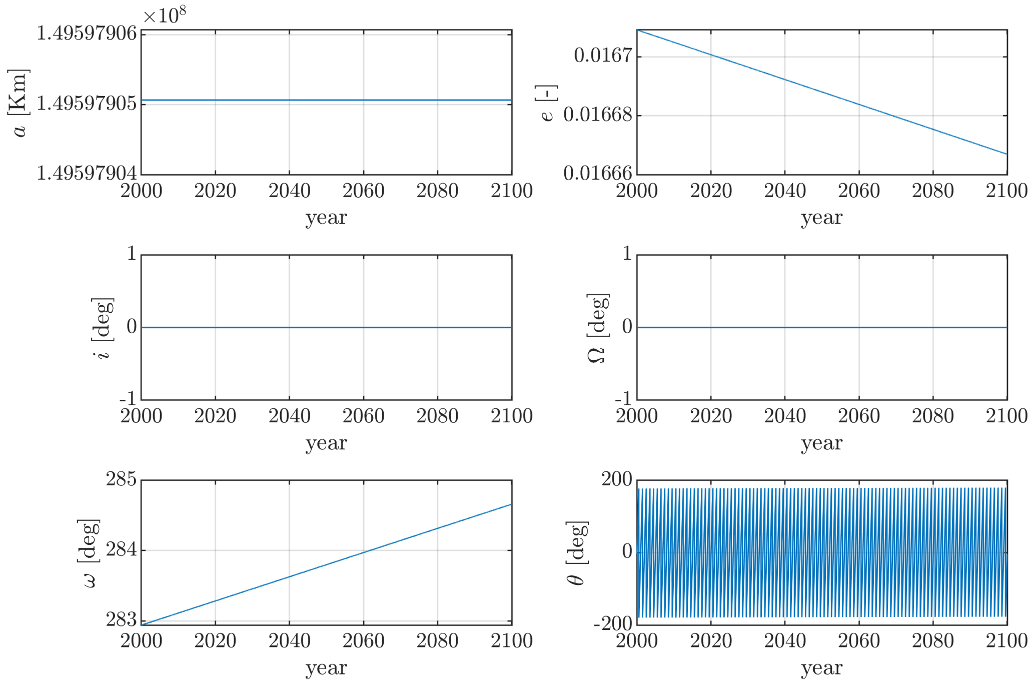

Figure 4.1: Sun ephemerides evolution in 100 years, ecliptic frame.

The Sun model is simply taken by inverting the Earth's ephemerides in its orbit around the Sun. The orbital elements thus retrieved will be referred to as Sun ephemerides and are reported in Fig. 4.1.

4.1.2. Moon model

For the Moon model on the other hand, the ephemerides are computed starting from the Vallado algorithm [33] to retrieve the position vector in the equatorial frame. The velocity vector is obtained by using a simple difference scheme to derive in time. The two vectors are rotated to the ecliptic frame and the cartesian coordinates are transformed into the Moon's orbital elements around the Earth.

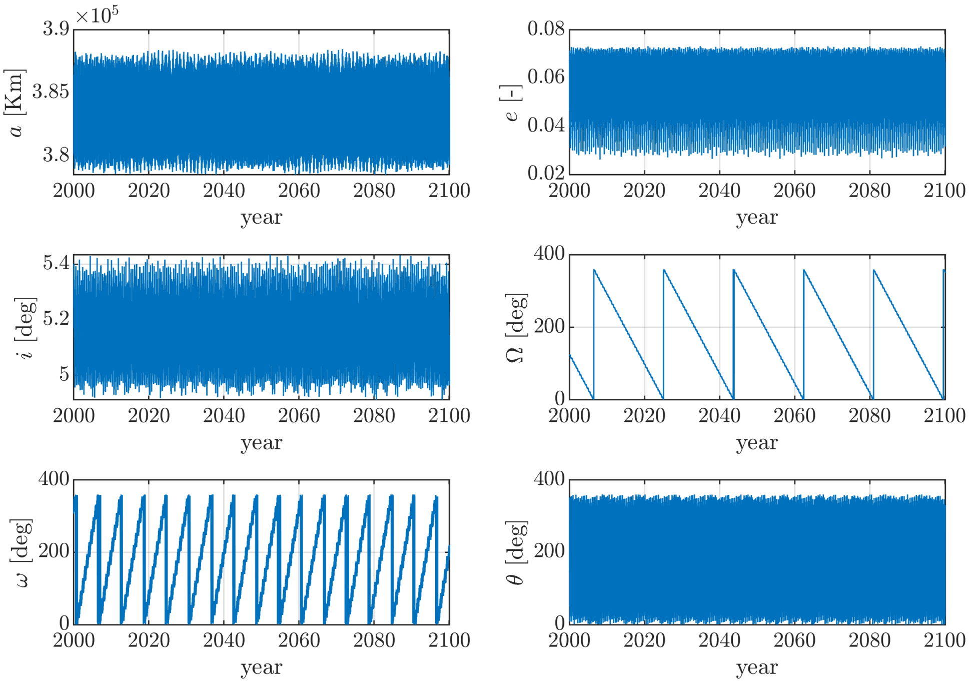

Figure 4.2: Moon ephemerides evolution in 100 years, ecliptic frame.

The Moon ephemerides evolution is reported in Fig. 4.2. It can be observed that:

- The semi-major axis $a_☾$, the eccentricity $e_☾$ and the inclination $i_☾$ in the ecliptic frame shows short-term oscillation with a limited amplitude, they can be safely neglected and considered as constant.
- Contrarily, the precession of both the RAAN $\Omega_☾$ and the argument of perigee $\omega_☾$ is cleary visible and cannot be neglected.
  With TA potential, the node elimination may cause wide errors in the propagation.

Regarding the argument of perigee, the assumption of constant Moon ephemerides in the Hamiltonian formulation for the phase space single-DoF may exacerbate the discrepancies even more.

4.2. Spacecraft orbital propagation

Since this work focuses on HEO satellites, following the work done in the thesis from Asperti [30], the models previously described are checked using the INTEGRAL spacecraft [5]. In this section, the results in both the ecliptic frame and equatorial are presented for comparison. The orbit is propagated considering the J_2 effect together with lunar and solar third-body perturbations. Different methods are used for comparison:

- Gauss planetary equation, computing the acceleration vectors induced by the disturbing forces
- Lagrange planetary equation, using SA potentials
- Lagrange planetary equation, using DA potentials
- Lagrange planetary equation, using TA potentials

4.2.1. Ecliptic frame

The initial orbital elements were taken on 22/03/2013 using the ecliptic frame. Those are reported in Table 4.1

a [km]	e [-]	i [deg]	Ω [deg]	ω [deg]	θ [deg]
87720	0.8766	65.70	254.83	279.02	188.30

Table 4.1: INTEGRAL mission orbital elements on 22/03/2013, ecliptic frame.

The results are reported in Fig. 4.3. The SA and DA methods are reliable, the resulting orbital elements evolution follows almost perfectly the Gauss scheme results. On the other hand, the TA method introduces a very strong assumption, and the propagation result differs significantly from the others. The TA orbital elements show a clear periodic behaviour since the dependence on the Moon node was filtered out.

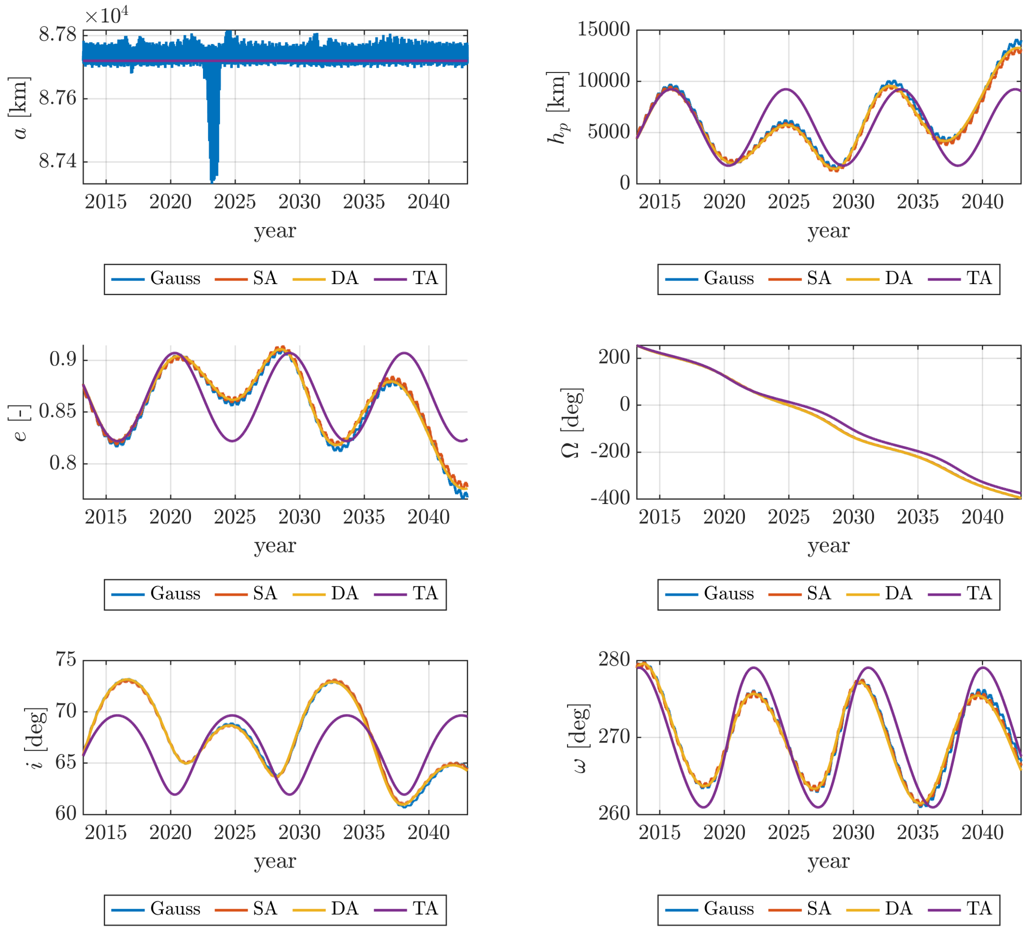

Figure 4.3: INTEGRAL orbital elements evolution in ecliptic frame using different methods (Gauss, SA, DA, TA). In order, semi-major axis a, pericentre altitude h_p, eccentricity e, RAAN Ω, inclination i, argument of pericentre ω.

4.2.2. Equatorial frame

As a matter of comparison, the propagation is carried out for the same satellite in the equatorial frame. The initial orbital elements are rotated to the new frame and are reported in Table 4.2, and the results in Fig. 4.4.

a [km]	e [-]	i [deg]	Ω [deg]	ω [deg]	θ [deg]
87720	0.8766	61.8081	266.41	253.1972	188.30

Table 4.2: INTEGRAL mission orbital elements on 22/03/2013, equatorial frame.

The same observations for the numerical accuracy of the SA, DA and TA are valid.

However, in the ecliptic frame, the result of the TA is closer to the other schemes outcomes, if compared to the results observed in the equatorial frame.

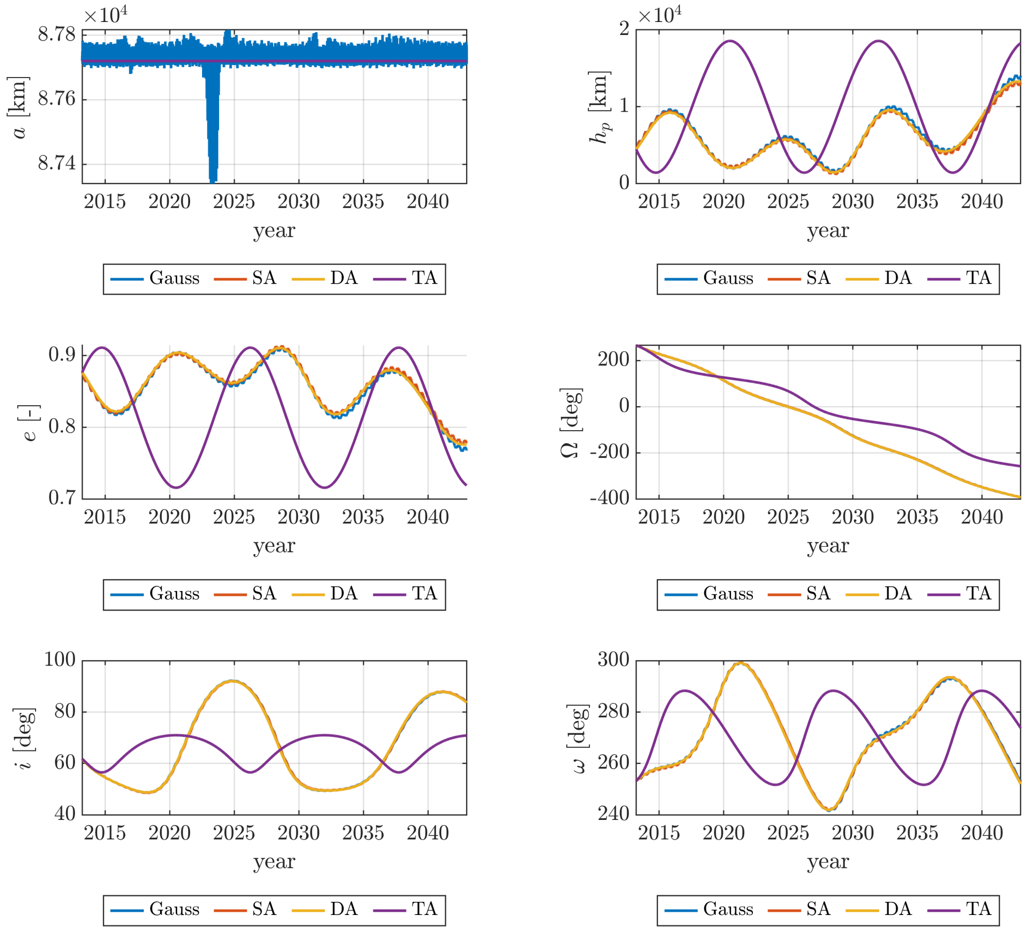

Figure 4.4: INTEGRAL orbital elements evolution in ecliptic frame using different methods (Gauss, SA, DA, TA). In order, semi-major axis a, pericentre altitude h_p, eccentricity e, RAAN Ω, inclination i, argument of pericentre ω.

Clearly, the frame selection has an impact on the discrepancies between the TA results and the real orbital evolution.

4.3. Laplace frame

Some other frames will be considered in this work, by investigating the application of the Laplace frame for the manoeuvring optimisation.

4.3.1. Definition of the Laplace frame

Following the mathematical description from Allan and Cook [39], the formulation can be used when the orbital perturbations in action are the main attractor's oblateness and an arbitrary number of third-body perturbers. Firstly, the mean motion n definition is needed:

$$n := \sqrt{\frac{\mu}{a^3}} \tag{4.1}$$

which represents the average value of the angular velocity of the satellite in its orbital motion within a period.

In such a scenario, the overall DA potential can thus be written in adimensional form dividing it by na^2. Retaining only the 2^{nd} order term found in Eq. (3.59) yields to:

$$\begin{aligned}\overline{\overline{\mathcal{R}}}^* = \frac{\overline{\overline{\mathcal{R}}}}{na^2} =& \omega_0(1-e^2)^{-3/2}\left[\frac{1}{2}\left(\hat{\mathbf{R}}\cdot\hat{\mathbf{n}}_0\right)^2-\frac{1}{6}\right]+\ldots \\ &+\sum_{j=1}^{N_p}\omega_j\left\{\frac{1}{2}\left(1-e^2\right)\left(\hat{\mathbf{R}}\cdot\hat{\mathbf{n}}_j\right)^2+e^2\left[1-\frac{5}{2}\left(\hat{\mathbf{P}}\cdot\hat{\mathbf{n}}_j\right)^2\right]\right\}\end{aligned} \tag{4.2}$$

where n is the mean motion, $\hat{\mathbf{R}}$ is the unitary versor directed along the normal to the satellite's orbital plane, n_0 is the normal to the equator, n_j is the normal to the j-th third-body's orbital plane and N_p is the number of perturbers bodies. Lastly, $\hat{\mathbf{P}}$ is the unit vector directed towards the pericentre of the spacecraft's orbit. Regarding the terms ω_0 and ω_j, they are defined as:

$$\omega_0 = \frac{3nJ_2R_p^2}{2a^2} \tag{4.3}$$

$$\omega_j = \frac{3\mu_j}{4na_j^3(1-e_j^2)^{3/2}} \tag{4.4}$$

where μ_j is the j-th third-body's gravitational parameter and a_j, e_j respectively its semi-major axis and eccentricity.

At this point, instead of expressing the equations of motion in terms of orbital elements, it is much simpler to use vectorial elements not tied to any particular frame. Those are defined as:

$$\mathbf{e} = e\hat{\mathbf{P}} \tag{4.5}$$

$$\mathbf{h} = \sqrt{1-e^2}\hat{\mathbf{R}} \tag{4.6}$$

so that the two are orthogonal and the sum of their squared magnitude is unitary:

$$\mathbf{e} \cdot \mathbf{h} = 0 \tag{4.7}$$

$$\|\mathbf{e}\|^2 + \|\mathbf{h}\|^2 = 1 \tag{4.8}$$

Using those elements the equations of motion can be written in a compact and symmetrical form:

$$\begin{cases} \dot{\mathbf{h}} = \mathbf{h} \times \dfrac{\partial \overline{\overline{\mathcal{R}}}^*}{\partial \mathbf{h}} + \mathbf{e} \times \dfrac{\partial \overline{\overline{\mathcal{R}}}^*}{\partial \mathbf{e}} \\ \dot{\mathbf{e}} = \mathbf{e} \times \dfrac{\partial \overline{\overline{\mathcal{R}}}^*}{\partial \mathbf{h}} + \mathbf{h} \times \dfrac{\partial \overline{\overline{\mathcal{R}}}^*}{\partial \mathbf{e}} \end{cases} \tag{4.9}$$

Looking at Eq. (4.2), for a circular orbit ($e = 0$) the term $\partial \overline{\overline{\mathcal{R}}}^* / \partial \mathbf{e}$ vanishes.
In such a scenario Eq. (4.6) reduces to $\mathbf{h} \equiv \hat{\mathbf{R}}$, hence its time derivative after some operations can be written as:

$$\dot{\hat{\mathbf{R}}} = -\sum_{j=0}^{N_p} \omega_j \left(\hat{\mathbf{R}} \cdot \hat{\mathbf{n}}_j\right)\left(\hat{\mathbf{n}}_j \times \hat{\mathbf{R}}\right) \tag{4.10}$$

where for $j = 0$ the J_2 effect is accounted while for $j = 1, 2$ the third-body perturbations are considered.

Please note that if there's only a single term on the right-hand side of Eq. (4.10), the normal to the satellite's orbital plane would regress solely around the present $\hat{\mathbf{n}}_j$ at a constant rate of $\omega_j \cos\alpha_j$, where α_j represents the angle between the normal to the satellite's plane and the perturber's plane. Specifically, $\alpha_j = \arccos \hat{\mathbf{R}} \cdot \hat{\mathbf{n}}_j$ given their unitary nature.

In a complex scenario involving multiple perturbations, the identification of the Laplace plane can be determined by seeking the specific orientation $\hat{\mathbf{R}}$ of the orbital plane in a circular orbit scenario where no regression is evident, denoted by $\dot{\hat{\mathbf{R}}} = 0$, thus implying $\hat{\mathbf{R}} = const.$ Derived from Eq. (4.10):

$$\sum_{j=0}^{N_p} \omega_j \left(\hat{\mathbf{R}}_{\mathcal{L}} \cdot \hat{\mathbf{n}}_j\right) \left(\hat{\mathbf{n}} j \times \hat{\mathbf{R}} \mathcal{L}\right) = 0 \tag{4.11}$$

A more concise representation is attainable by defining the symmetric tensor $\boldsymbol{\Psi}$ as:

$$\boldsymbol{\Psi} = \sum_{j=0}^{N_p} \hat{\mathbf{n}}_j \hat{\mathbf{n}}_j^T \tag{4.12}$$

This transformation yields Eq. (4.11) as:

$$\hat{\mathbf{R}} \mathcal{L}^T \boldsymbol{\Psi} \hat{\mathbf{R}} \mathcal{L} = 0 \tag{4.13}$$

Signifying an eigenvalue problem, where any eigenvector of $\boldsymbol{\Psi}$ characterizes the normal to a circular orbit devoid of any plane regression, thus remaining temporally fixed. While at least three possible eigenvectors exist, conventionally, the normal to the Laplace frame $\hat{\mathbf{R}}_{\mathcal{L}}$ corresponds to the eigenvector linked with the greatest eigenvalue λ.

4.3.2. Orbital propagation in Laplace frame

For an HEO satellite such as the one analysed in this work, the motion of the orbital plane from Eq. (4.10) is a combination of rates of procession about three different axes. The j subscript identifies in order, starting from 0, the J_2, Sun and Moon perturbations.

Furthermore, not only the lunar plane is inclined with respect to the ecliptic by roughly 5.2°, but it also shows a precessing motion with a period of more or less 18.6 years (see Fig. 4.2). In its computation, some approximations are usually made. In the following, some scenarios considering different assumptions are analysed, and the satellite's orbital elements are propagated in time in those frames, to compare the results between the TA and the DA.
Those different Laplace frame cases are:

1. Lunar orbit assumed to lay in the ecliptic
2. Moon orbital elements assumed constant (no precession considered)

3. Osculating Laplace frame (the orientation in this case is time-dependent)
4. Moon inclination and argument of pericentre averaged
5. Moon orbital elements averaged

Apart from the third case, the other scenarios deal with a simplified fixed Laplace frame. For simplicity, in the following work they will be referred to as L_i, based on their presentation here.

Lunar orbit laying in the ecliptic

As suggested by Allan and Cook [39], this Laplace frame is computed simply by considering $\hat{\mathbf{n}}_1 = \hat{\mathbf{n}}_2 = \hat{\mathbf{n}}_\odot$. Eq. (4.12) becomes:

$$\boldsymbol{\Psi} = \omega_0 \hat{\mathbf{n}}_0 \hat{\mathbf{n}}_0^T + (\omega_1 + \omega_2)\, \hat{\mathbf{n}}_\odot \hat{\mathbf{n}}_\odot^T \tag{4.14}$$

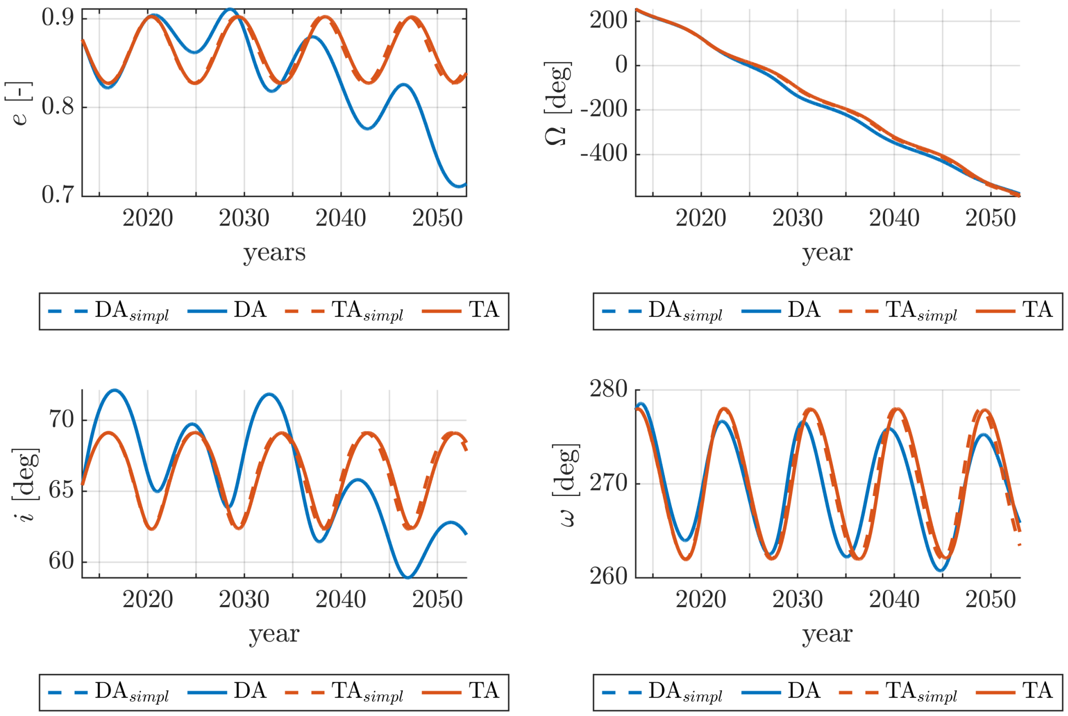

Figure 4.5: INTEGRAL orbital elements evolution in fixed L_1 frame using DA, TA, and their simplified version DA$_{simpl}$, TA$_{simpl}$. In order, eccentricity e, RAAN Ω, inclination i, argument of pericentre ω.

The orbital evolution of the satellite in this frame is reported in Fig. 4.5, considering only the DA and the TA since the accuracy of the former method has already been proved. To better comprehend the following figures, a small legend is proposed:

- DA_{simpl} is propagated maintaining in the model the assumptions made in the Laplace frame definition, for example in L_2 the Moon orbital elements are considered fixed.
- DA is the real case propagation with no added assumption apart from the ones embedded by the DA model.
- TA_{simpl} is propagated with the added assumption of fixed third-body elements, eliminating the time variable t.
- TA releases the previous assumption and works with time-varying third-bodies' ephemerides.

In this first case, the DA results are the same, since no assumption was made about the Moon's ephemerides. The two TA results show a small variation that may seem uninfluential, but the differences may prevent the result of the simplified TA from achieving the re-entry in the time-varying model. Compared to the DA, again the TA model catches only the periodic behaviour of the dynamics, and as time progresses the difference increases.

Moon orbital elements fixed

This model was implemented by Asperti [30]. The results are presented in Fig. 4.6. As established also from the first Laplace case, the TA shows a periodic result while the DA orbital elements can widely vary in time in a non-periodic fashion.

However, if the integration is carried out embedding the assumption (represented by DA_{simpl}), the results are closer to the TA due to the elimination of the Moon's precession from the DA model. The two TA results compared to each other show some minor variations.

On the other hand, again, the DA result in a real case integration differs even more from the TA with respect to the previous scenario L_1. However, note that the eccentricity with DA shows the same evolution observed in the L_1 case. This was expected, since in the absence of any assumptions that modify the problem, the evolution of the eccentricity does not depend on the chosen frame, contrarily to the Euler angles.

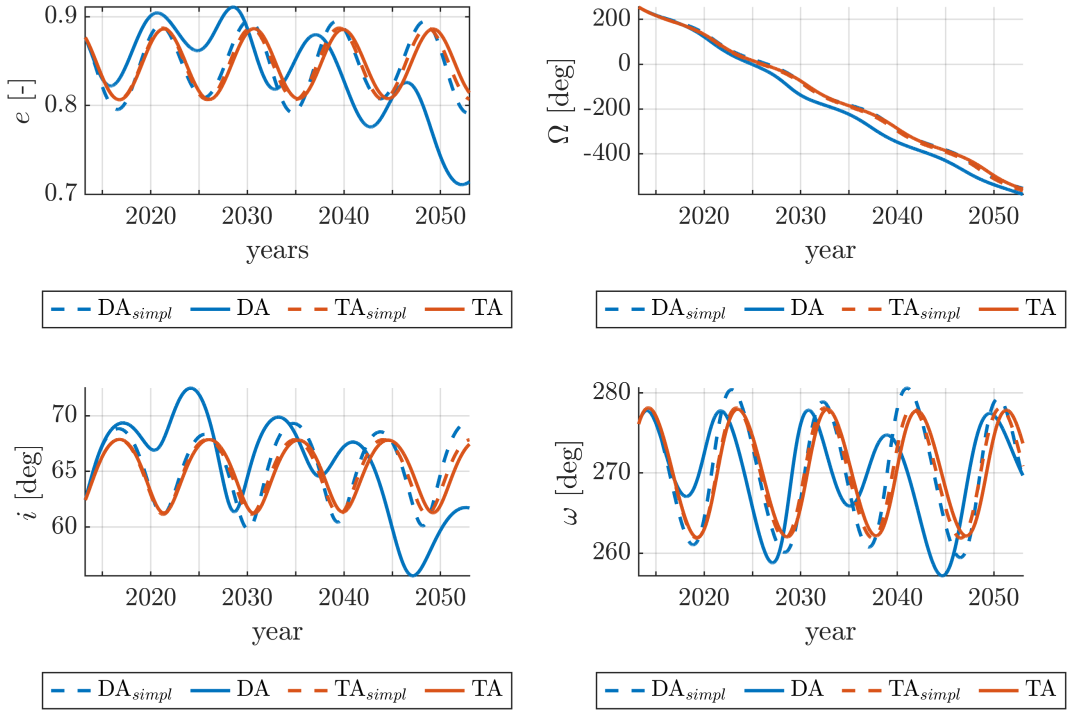

Figure 4.6: INTEGRAL orbital elements evolution in fixed L_2 frame, using DA, TA and their simplified version DA$_{simpl}$, TA$_{simpl}$. In order, eccentricity e, RAAN Ω, inclination i, argument of pericentre ω.

Osculating Laplace frame

In this scenario, the application of a time-dependent rotating Laplace frame is considered, so no additional assumptions are being made to simplify the computation. The satellite orbital elements propagation in this case requires an additional potential term, due to the rotating frame:

$$\mathcal{R}_{rot} = -\boldsymbol{\omega}\left(\mathbf{r} \times \mathbf{v}\right) \tag{4.15}$$

where $\boldsymbol{\omega}$ is the angular velocity vector of the osculating Laplace plane, while $\mathbf{r}$ and $\mathbf{v}$ are respectively the position and the velocity vectors of the satellite.

Firstly, a central difference scheme is used to compute the time derivative of the rotation matrix from the equatorial frame to the instantaneous Laplace frame:

$$\dot{\mathbf{R}}_{eq2L}(t) = \frac{\mathbf{R}_{eq2L}(t+\Delta t) - \mathbf{R}_{eq2L}(t-\Delta t)}{2\Delta t} \tag{4.16}$$

From [40], it can be shown that:

$$\boldsymbol{\Omega} = -\dot{\mathbf{R}}_{eq2L}\mathbf{R}_{eq2L} \tag{4.17}$$

with $\boldsymbol{\Omega}$ being the following matrix:

$$\boldsymbol{\Omega} = \begin{bmatrix} 0 & -\omega_z & \omega_y \\ \omega_z & 0 & -\omega_x \\ -\omega_y & \omega_x & 0 \end{bmatrix} \tag{4.18}$$

The elements of the angular rate vector $\{\omega_x, \omega_y, \omega_z\}$ are thus retrieved.

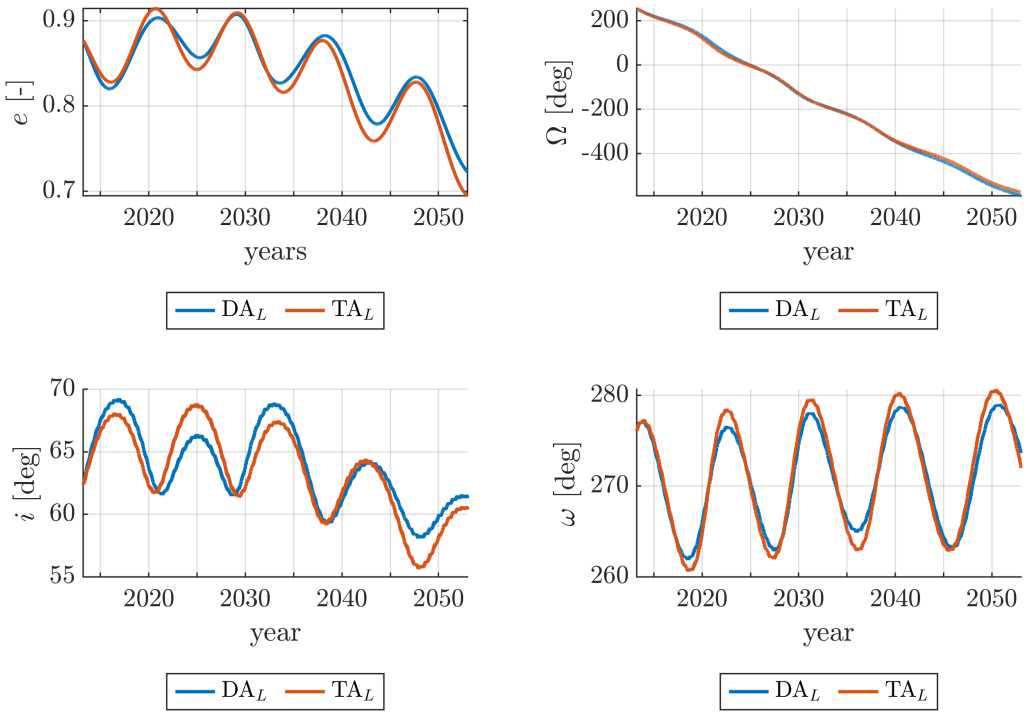

Figure 4.7: INTEGRAL orbital elements evolution in the rotating L_3 frame, using different methods (DA, TA). In order, eccentricity e, RAAN Ω, inclination i, argument of pericentre ω.

Hereafter, the osculating Laplace frame L_3 is used to propagate the satellite's orbital elements using both the DA and TA potentials. The results are shown in Fig. 4.7.

Opposed to the previous cases, only the DA and TA propagations are considered since no model assumption is made for the Moon's orbital elements, while the time-simplified TA does not suit a frame that is intrinsically varying in time.
The results shown are drastically different from the previous cases (and as it will be shown, even from the next cases). This model can capture quite closely the system's dynamics, making it a very interesting case for the optimisation procedure.

An important note is that the L3 results presented above were achieved using the TA perturber's potentials while keeping the full rotational potential, which is equivalent to the DA one as there's no reliance on the fast angles. If, however, the rotational potential in its TA version is utilized, the outcomes can be seen in Fig. 4.8.
The orbital evolution is again periodic, thus not keeping track of the real dynamics. That said, with respect to the other Laplace scenarios, the results are closer to the DA evolution.

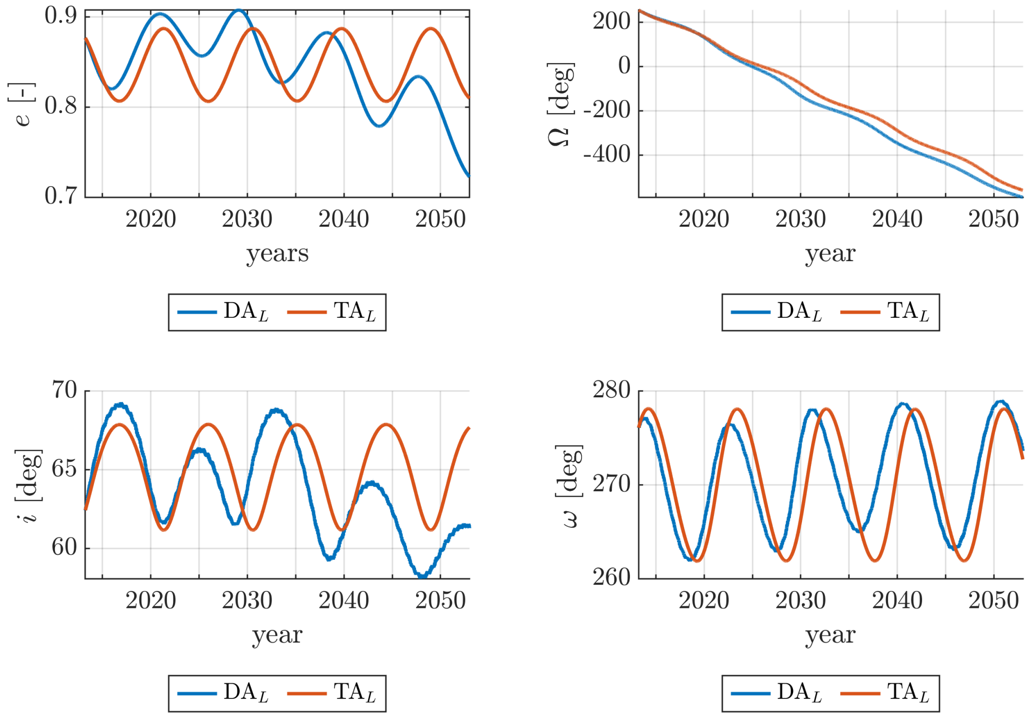

Figure 4.8: INTEGRAL orbital elements evolution in the rotating L_3 frame, using DA and TA with rotating potential $\overline{\overline{\overline{\mathcal{R}}}}_{rot}$.

Moreover, even the accuracy of the DA results in this peculiar frame should be tested. To do that, the orbit can be propagated in either the equatorial or the ecliptic frame.

The resulting cartesian coordinates can be rotated to the osculating Laplace frame, which changes in time.
The comparison is presented in Fig. 4.9.

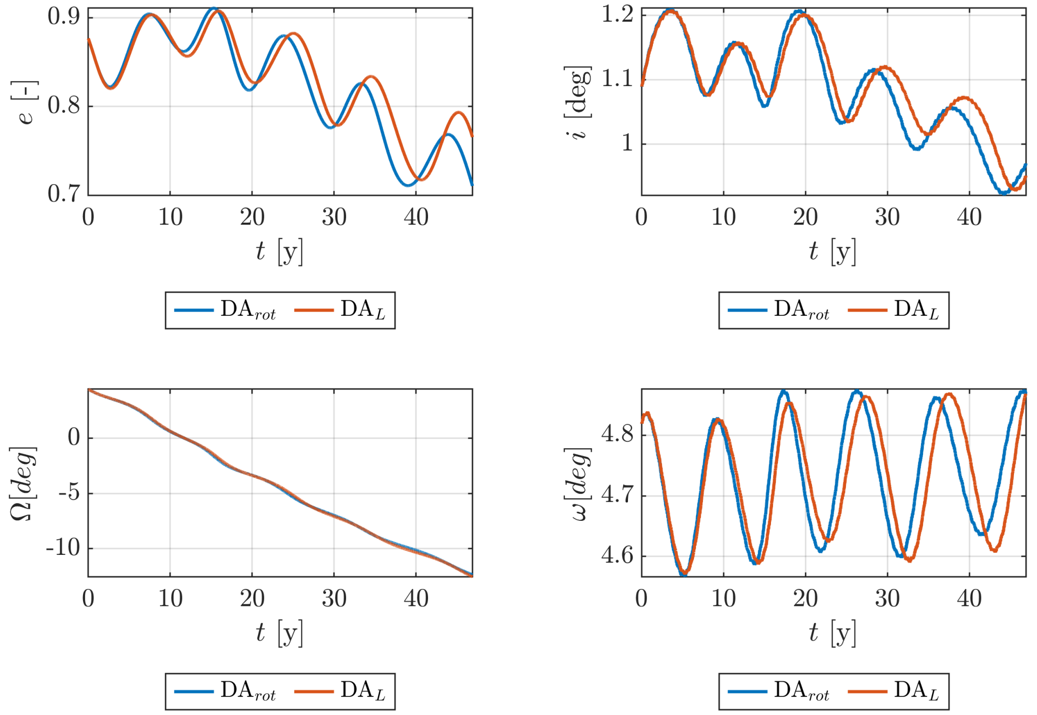

Figure 4.9: Accuracy of the rotating Laplace frame integration method proposed DA$_L$, compared with a posteriori rotation from the equatorial orbital evolution to the instantaneous rotating Laplace frame DA$_{rot}$.

It can be observed that a cumulative integration error is present, maybe due to the time derivative error given by Eq. (4.16), with Δt and the integration tolerances tuned to account for the higher computational cost with respect to the other propagation methods presented. Note that the eccentricity discrepancies were also evident by comparison with the other cases analysed since, as already mentioned, the evolution of e does not depend on the frame.
Nonetheless, the integration in the first $20 - 25$ years can be reasonably assumed as a good representation of the orbital evolution, and more importantly, the TA results are closer to the real problem dynamics despite the L_3 propagation error.

Mean lunar inclination and argument of pericentre

The fourth case analyses once again a fixed Laplace frame. The Moon's orbital elements are fixed. In particular, the Moon's inclination and argument of pericentre are set to their mean values obtained by analysing the Moon's orbital period. Values are reported in Table 4.3. Here the focus is to try to compute an "average Laplace plane" to test the orbital propagation, and since $i_{\leftmoon}$ oscillates periodically between $18-28$ degrees, its values were averaged together with $\omega_{\leftmoon}$.

Title of Table (optional)

$\bar{i}_{\leftmoon}$ [deg]	$\overline{\omega}_{\leftmoon}$ [deg]
23.70	180.00

Table 4.3: Fixed mean Moon orbital elements $\{\bar{i}_{\leftmoon}, \overline{\omega}_{\leftmoon}\}$, referred to the equatorial frame.

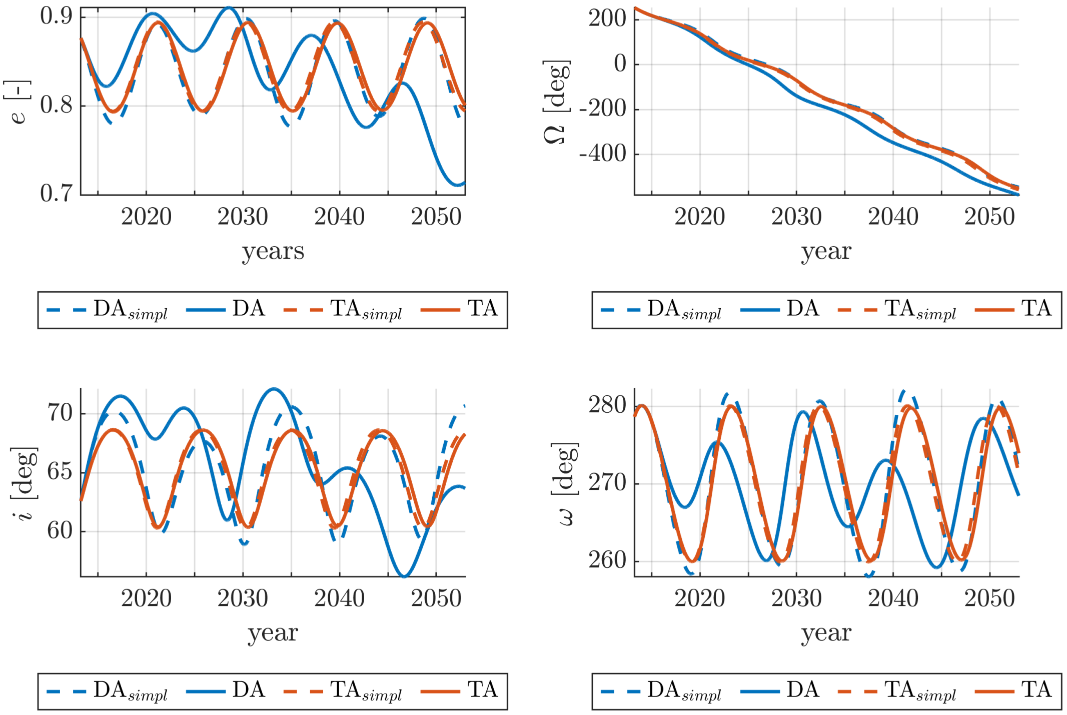

Figure 4.10: INTEGRAL orbital elements evolution in fixed average Laplace frame (case 4) using DA, TA and their simplified version DA$_{simpl}$, TA$_{simpl}$. In order, eccentricity e, RAAN Ω, inclination i, argument of pericentre ω.

Also, this time the real case scenario results are compared to the propagation embedding the assumptions in the integration procedure. In Fig. 4.10 it can be seen that even in this case discrepancies are present, but in the simplified case propagation the offset between the DA and TA is decreased with respect to the previous results.

Mean lunar orbital elements

$\bar{a}_{☾}$ [km]	$\bar{e}_{☾}$ [-]	$\bar{i}_{☾}$ [deg]	$\bar{\Omega}_{☾}$ [deg]	$\bar{\omega}_{☾}$ [deg]
383286	0.0556	23.70	180	180

Table 4.4: Fixed mean Moon orbital elements $\{\bar{a}_{☾}, \bar{e}_{☾}, \bar{i}_{☾}, \bar{\Omega}_{☾}.\bar{\omega}_{☾}\}$, referred to the equatorial frame.

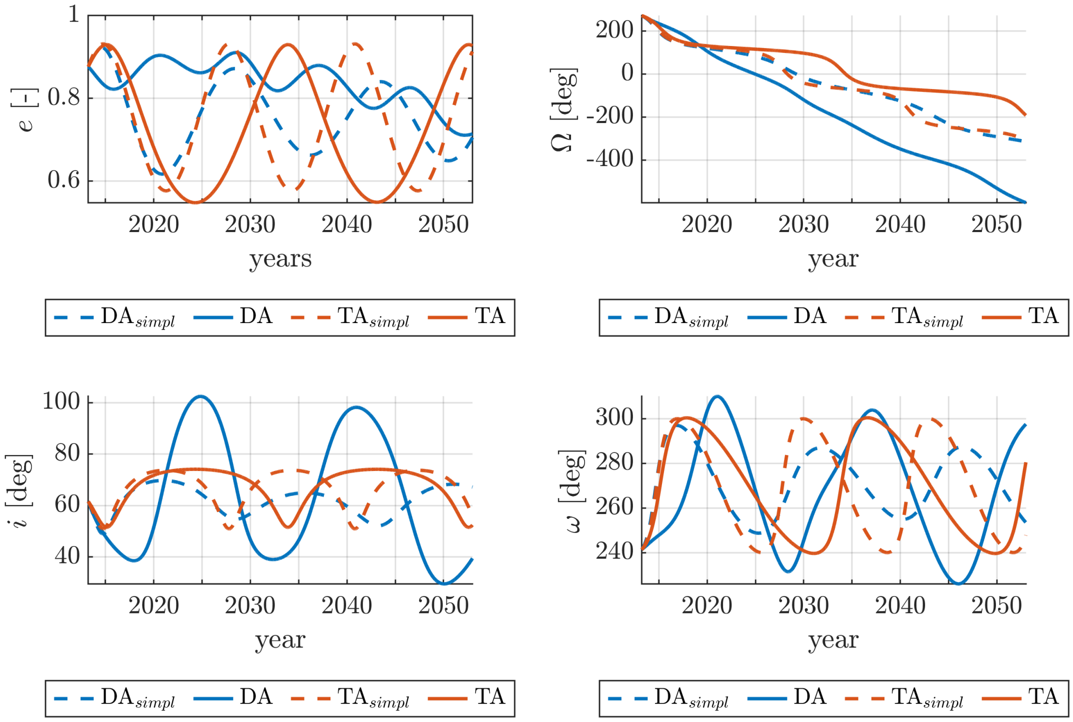

Figure 4.11: INTEGRAL orbital elements evolution in fixed Laplace frame with fully averaged Moon orbital elements (case 5) using DA, TA and their simplified version DA$_{simpl}$,TA$_{simpl}$. In order, eccentricity e, RAAN Ω, inclination i, argument of pericentre ω.

In the last case scenario, all the Moon orbital elements are set to their mean values with values shown in Table 4.4. The assumption on the fixed node in particular has a bad impact on the DA results.

It is clear from the results in Fig. 4.11, that those assumptions are not good for studying the orbital elements evolution of the system, thus not representing a model similar to the real orbit evolution. Therefore, for an "average" Laplace plane study it is better to refer to the fourth case here presented.

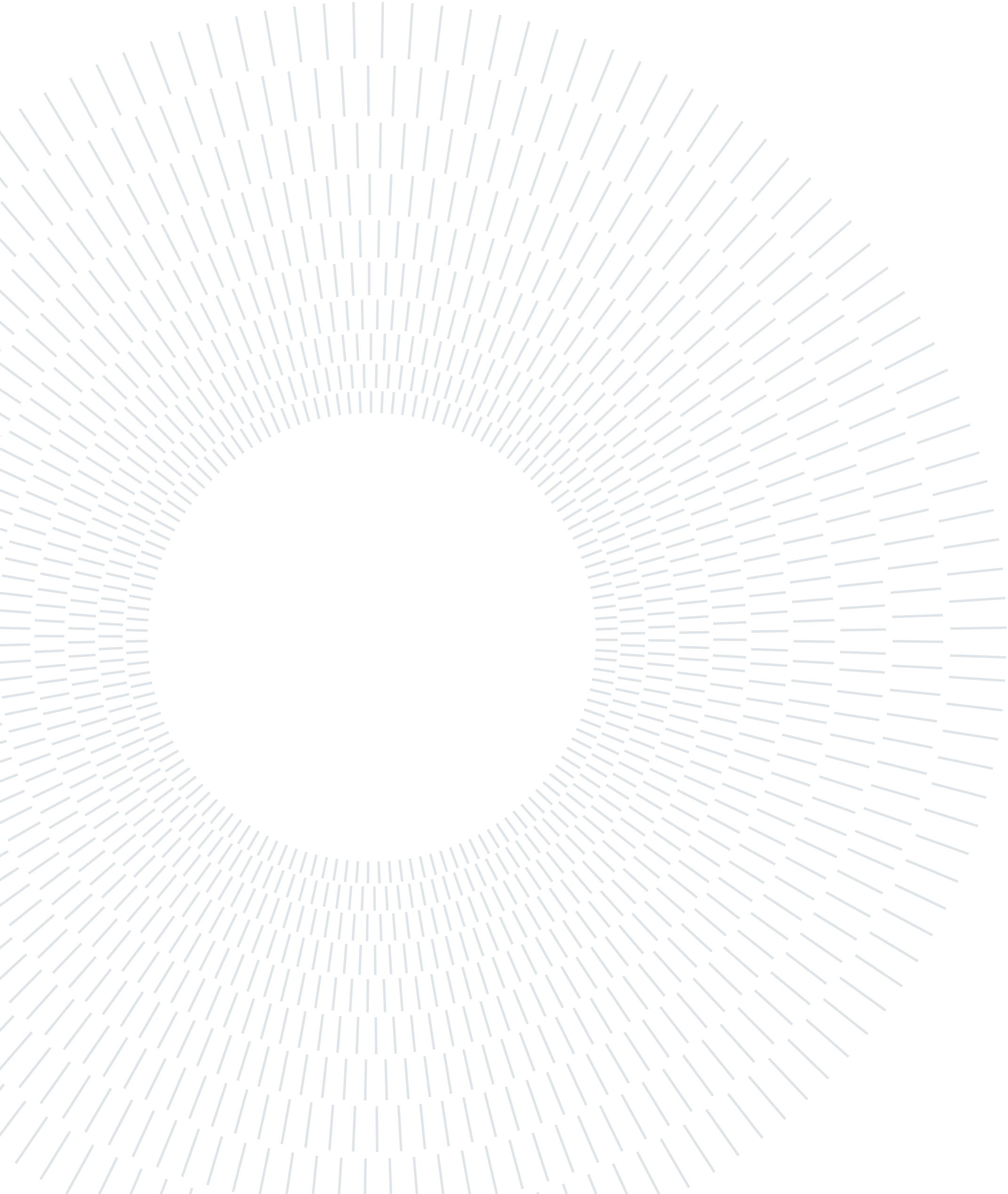

5 | Disposal manoeuvre strategy

To reduce the amount of space debris in orbit around the Earth, the Inter-Agency Space Debris Coordination Committee (IADC) issued strict regulations for debris mitigation, starting from the mandatory necessity of implying end-of-life (EoL) plans for new satellites. Two different strategies are possible

- Earth re-entry trajectory by exploiting the natural decay caused by the atmospheric drag for satellite disintegration.
- transfer to a graveyard orbit.

Earth re-entry is the preferable solution, and the IADC states that the procedure must be completed within a time limit of 25 years from the satellite decommissioning. Whenever this is not achievable, such as a GEO or MEO satellite, where the re-entry would be too expensive, the graveyard orbit solution is preferred. In both cases, any interaction with other orbiting objects must be avoided.
In the case of an HEO satellite, the eccentricity is high enough to allow the possibility of enhancing its wide orbital parameter oscillation via proper manoeuvring, favouring a natural atmospheric re-entry.

In this section the disposal manoeuvring strategy will be discussed.

Target altitude

The first thing to be set is the target altitude to achieve the orbital re-entry. Given that the atmosphere interface is set at 120 km [41][42], as suggested by Colombo et al. [38], this limit is often considered for LEO satellites or HEO missions with lower orbit energy compared to INTEGRAL. For this reason, it is better to be conservative and consider a lower target perigee altitude:

$$h_{p,min} = min \left\{ h_{p,min}\left(t\right) \right\} <= 50\text{km}$$

However, in the computation, a 2% error is allowed (therefore validating as successful a minimum perigee altitude of 51 km).

5.1. Modelling

The disposal strategy follows the approach described by Colombo et al. [38] considering a single impulsive manoeuvre (with burning time approximately zero $t_b \approx 0$). Given the initial orbital parameters before the manoeuvre is applied, the latter is described in the $\left\{\hat{\mathbf{T}}, \hat{\mathbf{N}}, \hat{\mathbf{H}}\right\}$ frame (discussed in Section 2.3.3) by the following parameters:

- the impulse magnitude Δv
- the in-plane angle
- the out-of-plane angle.

with the geometry reported in Fig. 5.1.

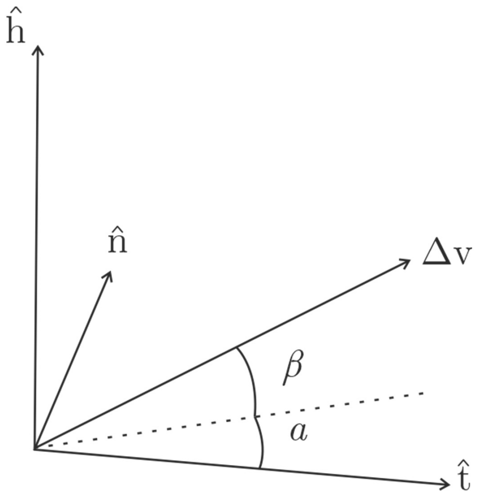

Figure 5.1: Manoeuvre parameters $\{\Delta v, \alpha, \beta\}$ in $\{\hat{\mathbf{T}}, \hat{\mathbf{N}}, \hat{\mathbf{H}}\}$ frame

5.1.1. Gauss equations for impulsive manoeuvre

The manoeuvre itself is modelled as:

$$\Delta \mathbf{v} = \Delta v \begin{bmatrix} \cos\alpha\cos\beta \\ \sin\alpha\cos\beta \\ \sin\beta \end{bmatrix} \tag{5.1}$$

While the initial orbital elements $\{a, e, i, \Omega, \omega\}$ are determined by the orbit evolution, the actual time of the manoeuvre can be optimised. That being said, the strategy that will be used consists of parsing the manoeuvring time t_m beforehand in a limited previously chosen number, hence integrating only once all the possible initial orbital parameters before the manoeuvre. In addition, due to the long-term focus, using an assumption similar to the one used in the averaging procedure, the orbital elements can be considered constant along the orbital period. This allows us to write the true anomaly θ as an optimisation parameter. Accordingly, the optimisation variables are:

$$\mathbf{x} = \{\Delta v, \alpha, \beta, \theta\}$$

After the manoeuvre, the satellite state is changed with respect to the initial one as follows:

$$\{\mathbf{x}, \mathbf{v}\}_{bm} = \{\mathbf{x}, \mathbf{v} + \Delta\mathbf{v}\}_{am}$$

were subscript bm stands for *before manoeuvre* and am means *after manoeuvre.*

Working with keplerian elements, the variation of the set $\{a, e, i, \Omega, \omega, \theta\}$ can be computed resorting to the Gauss' planetary equation described in Section 2.4.2. In finite-difference form, the following equations can be written [43]:

$$
\begin{aligned}
\Delta a &= 2\sqrt{\frac{a^3\left(1+2e\cos\theta+e^2\right)}{\mu\left(1-e^2\right)}}\cos\alpha\cos\beta\Delta v \\
\Delta e &= \sqrt{\frac{a\left(1-e^2\right)}{\mu\left(1+2e\cos\theta+e^2\right)}}\left[2\left(e+\cos\theta\right)\cos\alpha-\frac{1-e^2}{1+e\cos\theta}\sin\theta\sin\alpha\right]\cos\beta\Delta v \\
\Delta i &= \sqrt{\frac{a\left(1-e^2\right)}{\mu}}\frac{\cos\left(\omega+\theta\right)}{1+e\cos\theta}\sin\beta\Delta v \\
\Delta\Omega &= \sqrt{\frac{a\left(1-e^2\right)}{\mu}}\frac{\sin\left(\omega+\theta\right)}{\left(1+e\cos\theta\right)\sin i}\sin\beta\Delta v \\
\Delta\omega &= \left\{\frac{1}{e}\sqrt{\frac{a\left(1-e^2\right)}{\mu\left(1+2e\cos\theta+e^2\right)}}\left[2\sin\theta\cos\alpha+\left(2e+\frac{1-e^2}{1+e\cos\theta}\cos\theta\right)\cdot ....\right.\right. \\
&\qquad \left.\left. ...\cdot\sin\alpha\right]\cos\beta-\sqrt{\frac{a\left(1-e^2\right)}{\mu}}\frac{\sin\left(\omega+\theta\right)\cos i}{\left(1+e\cos\theta\right)\sin i}\sin\beta\right\}\Delta v \\
\Delta\theta &= \sqrt{\frac{\mu}{a^3\left(1-e^2\right)^3}}\left(1+e\cos\theta\right)^2-\frac{1}{e}\sqrt{\frac{a\left(1-e^2\right)}{\mu\left(1+2e\cos\theta+e^2\right)}}\left[2\sin\theta\cos\alpha+...\right. \\
&\qquad \left. ...+\left(2e+\frac{1-e^2}{1+e\cos\theta}\cos\theta\right)\sin\alpha\right]\cos\beta\Delta v
\end{aligned}
\tag{5.2}
$$

Note that in this set of equations some limitations are present:

- due to the presence of the term $\sqrt{1-e^2}$, the eccentricity value must be below 1, which is acceptable in the scenario analysed in this work.
- singularities for zero inclination and/or zero eccentricity due to the presence of the terms e and $\sin i$ at the denominator. In this work, this does not represent a problem since it deals with an orbit characterized by high eccentricity and inclination.

5.1.2. Constraints

The optimisation problem requires the definitions of some constraints to define the bounds of the problem. Given the set of optimisation variables previously mentioned:

$$\mathbf{x} = \{\Delta v, \alpha, \beta, \theta\}$$

which consists of one vectorial variable and three angles, the following reasoning can be applied to fix some bounds:

- the impulse Δv requires an adequate upper bound limit, neither too high to converge rapidly to a good solution, nor too strict, with the danger of invalidating the algorithm's possibility of finding the global minimum.
- the angles $\{\alpha, \beta, \theta\}$, on the other hand, are naturally periodic, hence their possible values can be bounded within a period.

Given those observations, the selected lower and upper bounds are reported in Table 5.1

	Lower bound	Upper bound
Δv	0	150
α	$-\pi$	π
β	$-\pi$	π
θ	$-\pi/2$	$\pi/2$

Table 5.1: Lower and upper bounds of the optimisation variables.

Nonetheless, the limitation imposed by the IADC of a maximum of 25 years to accomplish the re-entry must be respected, while aiming at the previously defined target altitude $h_{p,tar} = 50$ km

5.1.3. Cost function

In planning the manoeuvres for the entire life of the satellite, the minimization of the impulses is vital to minimize the propellant mass which has a big impact on the mission's overall cost. Here in this thesis, different optimisation strategies of the EoL Δv needed for the disposal will be analysed. Some of those consist of either local or global optimisation through the minimization of a cost function J whose formulation has to be defined.

The variables that will enter this cost function are the impulse Δv and the target altitude, inserted via penalty method. The latter is needed to drive the optimisation toward achieving successful de-orbiting while minimizing the impulse needed.

The penalty method consists of increasing the cost function value whenever the minimum

perigee altitude exceeds the target one. The increment shall be proportional to the constraint violation and to facilitate the global minimum search of gradient-based algorithms, a quadratic function is implemented. Also, the term involving the impulse is quadratic for the same reason.
The overall function is thus given by:

$$J = \lambda_v \left(\frac{\Delta v}{\sigma_v}\right)^2 + \lambda_{h_p} \max \left[\left(\frac{h_{p,min} - h_{p,tar}}{h_{p,tar}}\right), 0 \right]^2 \tag{5.3}$$

where the two terms are divided respectively by the fixed factors σ_v and $h_{p,tar}$ to obtain a dimensionless cost function. The latter was already explained thoroughly, while the former is set at $\sigma_v = 100$ m/s.
Moreover, two weighting factors λ_v and λ_{h_p} are tuned efficiently to get the best results possible. λ_{h_p} tuning in particular has already been discussed.
Those factors are summed up in Table 5.2

λ_v [-]	σ_v [m/s]	λ_{h_p} [-]	$h_{p,tar}$ [km]
1	150	100	50

Table 5.2: Weighting and reference factors fixed values.

5.2. optimisation strategies

As previously mentioned, in this thesis several strategies will be implemented and tested. Firstly, an analytical strategy based on the maximization of the Kozai parameter $\Delta\Theta$ will be described in Section 5.2.1, taking advantage of both the TA fast computation and the phase space formulation simplicity. Two different scenarios are here considered, one assuming no variations in time of the third-bodies orbital elements and the other aimed at working even in a scenario where those elements are not fixed to the initial values. The results will then be compared later in Chapter 6, considering a TA propagation where the effective time-varying ephemerides of the perturbers are considered.

The other main strategy presented consists of a hybrid optimisation trying to combine the goods of both the analytical optimisation formulation given by the phase space and the local optimisation exploiting the accuracy of the DA.

Lastly, a classic accurate global optimisation method will be implemented to compare the effectiveness of the proposed optimisation strategies.

Apart from the procedural differences between the methods, some common factors are present. For each optimisation procedure, the orbit is integrated from its initial condition in a fixed time period, and the results are parsed following the manoeuvring points t_m that are decided a priori.
This means that the optimisation gives as result the best set of variables that characterize the manoeuvre if the same is applied at that specific time instant t_m. Thereby each manoeuvring point will be associated with an optimised set, and the overall best solution will be given by the solution with the minimum Δv.

5.2.1. Phase space $-\Delta\Theta$ maximization strategy

Starting from the analytical strategies, here the TA formulation is heavily implemented. Firstly, the satellite's orbit is propagated in a given period with the TA method and the result is then parsed into a fixed amount of manoeuvring time instants t_m. Each parsed point will be passed to the optimiser to find the best possible set of variables $\{\Delta v, \alpha, \beta, \theta\}$.

This analytical strategy is based on the exploitation of the phase space representation through the Hamiltonian formulation described in Section 3.3.
As already discussed, the phase space topology depends essentially on the semi-major axis a and the Kozai parameter Θ, the latter in particular can change significantly the location of the Hamiltonian isolines, translating them upwards toward higher eccentricity values as the Kozai parameter decrements Fig. 5.2. It can be observed that a negative variation of Θ produces the effect researched for a natural de-orbit, increasing the eccentricity and thus lowering the perigee altitude.

A manoeuvre strategy maximizing the $-\Delta\Theta$ variation was proposed by Asperti [30]. Given the definition of the Kozai parameter in Eq. (3.80), its variation can be linearized as follows:

$$\Delta\Theta \approx -2e\cos i^2\Delta e - 2\left(1-e^2\right)\sin i\cos i\Delta i \tag{5.4}$$

Recalling Eq. (5.2), the orbital elements variations are linearly dependent on the impulse applied Δv, therefore also the Kozai parameter variation $\Delta\Theta$ is linear in Δv. Inserting them into Eq. (5.4) gives:

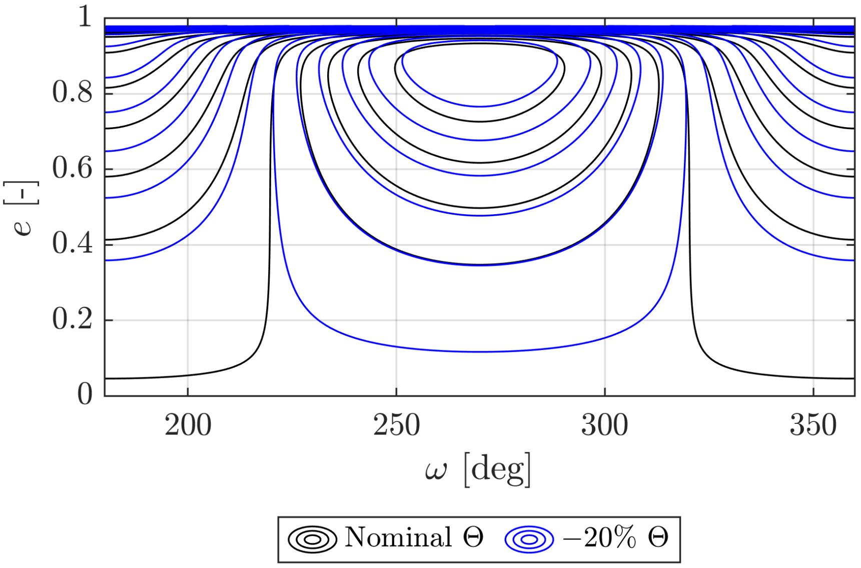

Figure 5.2: Modification of the phase space topology with a decrement of the Kozai parameter Θ

$$\Delta\Theta \approx -2\cos i\sqrt{\frac{a\left(1-e^2\right)}{\mu\left(1+2e\cos\theta+e^2\right)}}\left\{e\cos i\left[2\left(e+\cos\theta\right)\cos\alpha+\ldots\right.\right.$$

$$\left.-\frac{1-e^2}{1+e\cos\theta}\sin\theta\sin\alpha\right]\cos\beta+\left(1-e^2\right)\sin i\sqrt{1+2e\cos\theta+e^2}\cdot\ldots \tag{5.5}$$

$$\left.\cdot\frac{\cos\left(\theta+\omega\right)}{1+e\cos\theta}\sin\beta\right\}\Delta v$$

Which can be compactly rewritten by collecting all the terms depending on the optimisation angles $\{\alpha,\beta,\theta\}$ in a single function as follows:

$$\Delta\Theta \approx -2\cos i\sqrt{\frac{a\left(1-e^2\right)}{\mu}}f\left(\alpha,\beta,\theta\right)\Delta v \tag{5.6}$$

from which it is clear that maximizing $-\Delta\Theta$ is equivalent to maximising $f\left(\alpha,\beta,\theta\right)$ and Δv independently from one another, with the former defined as:

$$
\begin{aligned}
f\left(\alpha,\beta,\theta\right) :=& \frac{e\cos i}{\sqrt{1+2e\cos\theta+e^2}}\left[2\left(e+\cos\theta\right)\cos\alpha-\frac{1-e^2}{1+e\cos\theta}\sin\theta\sin\alpha\right]\cdot \ldots \\
&\cdot\cos\beta+\left(1-e^2\right)\sin i\frac{\cos\left(\theta+\omega\right)}{1+e\cos\theta}\sin\beta
\end{aligned}
\tag{5.7}
$$

Since the objective of the manoeuvre optimisation is finding the minimum Δv required to accomplish the disposal, the optimisation is first by finding the optimal set of angles that maximizes $f\left(\alpha,\beta,\theta\right)$, hence producing the maximum variation of the Kozai parameter Θ. This first part of the optimisation is carried out with MATLAB® built-in algorithm `particleswarm` setting the population size $N_{pop} = 500$.

Once the angles are retrieved, the evaluation of the minimum Δv capable of carrying out a successful re-entry of the satellite is still missing, remembering the constraint in the time limit imposed by the IADC of 25 years.

The strategy to optimise the impulse consists in comparing the Hamiltonian right after the manoeuvre given the new set of orbital elements $\{a, e, i, \Omega, \omega, \theta\}$ with the one related to the critical eccentricity, which is computed as:

$$
e_{crit} = 1 - \frac{h_{p,tar} + R_{\oplus}}{a} \tag{5.8}
$$

where the target altitude is set $h_{p,tar} = 50km$ as previously discussed and $R_{\oplus}$ is the Earth radius.

Two different methods will be presented, one which assumes the Hamiltonian autonomous ($\partial\mathcal{H}/\partial t = 0$) and a second one trying to consider the time variation of the Moon orbital elements, but still avoiding the orbit integration. In both cases, the TA potentials expressions are considered in the Hamiltonian evaluation

Autonomous Hamiltonian case

If the time dependence of the Hamiltonian is neglected (no variation of the third-body orbital elements), the Hamiltonian and the Kozai parameter after the manoeuvre ($\mathcal{H}_{am}$, Θ_{am}) would remain constant while the values of eccentricity e and argument of perigee ω vary.

The value of the critical inclination is a function of both Θ and e, as from Eq. (3.80) it is possible to write:

$$i_{crit} = \arccos \sqrt{\frac{\Theta}{1 - e_{crit}^2}} \tag{5.9}$$

Therefore by imposing the value of the Hamiltonian after the manoeuvre equal to the critical Hamiltonian (both now depend on the optimisation variable Δv since the manoeuvre is still not fully determined) as follows:

$$\mathcal{H}_{am} \left(\Delta v, e, \omega\right) = \mathcal{H}_{am,crit} \left(\Delta v, e_{crit}, \omega_{crit}\right) = \mathcal{H}_{am} \left(\Delta v\right) \tag{5.10}$$

with $\omega_{crit} = 3\pi/2$ since from the phase space diagrams it's the point where the maximum eccentricity is reached. The only unknown is thus the impulse Δv which can be finally computed with a zero search algorithm of the following function:

$$g(\Delta v) = \mathcal{H}_{am}(\Delta v) - \mathcal{H}_{am,crit}(\Delta v). \tag{5.11}$$

The advantages of such a method consist of an analytical optimisation of the manoeuvre variables, significantly reducing the computational time, at the cost of losing fidelity with the real-case scenario due to the numerous assumptions made in its formulation.

Time-dependent Hamiltonian

In this thesis another approach will be carried out following the same key points aforementioned, still considering the TA formulation, but without adding the assumption of non-varying third-body orbital elements.

In such a case, after the manoeuvre, the Hamiltonian will also show an implicit dependence in time $\mathcal{H}_{am} \left(\Delta v, e, \omega, t\right)$. Consequently, the Hamiltonian right after the manoeuvre at instant t_m may be different from the Hamiltonian in the following time instants, such that Eq. (5.10) is no more valid, meaning that another route shall be taken for the Δv optimisation.

Recalling Eq. (3.78), it is clear that not all the terms are time-varying, so they can be divided into time-independent term and time varying-term, the latter being principally the third-body perturbation potential, due to the oscillation of the orbital elements of the Moon.

Once the angles are optimised with the maximum $-\Delta\Theta$ approach, given the manoeuvring time instant t_m, the Hamiltonian dependence on time is treated by translating the post-manoeuvre orbital elements into successive time instants $t_i = t_m + i\Delta t$ parsed in a

25 years period, thus creating a vector of Hamiltonians whose orbital parameters of the satellite is kept constant at $\{e_{am}, i_{am}, 3\pi/2\}$ while the orbital elements of the third-body perturber are changing in time. This vector will be referred to as $\mathbf{H}$ and the i-th element is represented by $\mathcal{H}_i(\Delta v)$, computed at the time instant t_i.
This vector is then compared to another Hamiltonian vector where the critical orbital elements are computed using Eqs. (5.8),(5.9) are considered. The overall set of orbital elements is thus fixed as $\{e_{crit}, i_{crit}, 3\pi/2\}$ and is again translated to successive parsed time instants after t_m. Following the same nomenclature, this vector is called $\mathbf{H}_{crit}$ and its i-th element compute at t_i is $\mathcal{H}_{i,crit}(\Delta v)$
Note that some assumptions were made in the described strategy to avoid the propagation of the orbit which would nullify the TA formulation advantages. Even in the autonomous $\mathcal{H}(e, \omega)$ scenario the eccentricity and argument of perigee evolves in time, not remaining fixed, while the overall Hamiltonian does not change. Moreover, the time variation of the third-body orbital elements would induce an additional variation in the satellite's orbital elements.

Some optimisation functions were tested using either a zero search algorithm or through a minimization by using a squared version of the optimisation function. Some are here reported:

$$\begin{aligned} g_1(\Delta v) &= \text{sum}\left(\mathbf{H}_{crit}(\Delta v) - \mathbf{H}(\Delta v)\right) \\ g_2(\Delta v) &= \text{mean}\left(\mathbf{H}_{crit}(\Delta v) - \mathbf{H}(\Delta v)\right) \\ g(\Delta v) &= \max\left(\mathbf{H}(\Delta v) - \mathbf{H}_{crit}(\Delta v)\right) \end{aligned} \tag{5.12}$$

The one that gives the best results is the following function, utilizing a zero search algorithm:

$$\text{fun}(\Delta v) = \max\left(\mathbf{H}_{crit}(\Delta v) - \mathbf{H}(\Delta v)\right) \tag{5.13}$$

Note that if the order of the two terms is reversed, the result of the optimisation would change for the worse. This way, we are imposing that, at least, the values of the critical Hamiltonians are characterized by a slightly higher value than the actual one. This situation may correspond to an actual Hamiltonian at a slightly higher eccentricity with respect to the critical one, thus granting better results with respect to the case with the neglected variation of the third bodies' ephemerides where simply the nominal and critical Hamiltonian are imposed equal solely at the at t_m point. This imposition could not be made with a time-varying Hamiltonian.

5.2.2. Hybrid optimisation

Contrarily to the previous analytical strategies, here the DA computation is implemented for the preliminary orbital propagation due to its accuracy. Once again, the results are parsed in manoeuvring time instants t_m and then each single point is optimised through the hybrid algorithm.

The optimisation procedure itself aims at combining the low computational cost of the analytical method with the accuracy of the DA local optimisation, applying the former to get results that are later used as initial guesses for the DA optimisation.
Firstly, the Kozai parameter $\Delta\Theta$ maximization strategy is implemented to obtain the set of angles $\{\alpha, \beta, \theta\}$. Then the Δv optimisation is performed to get the last variable, but actually, this passage can be skipped if the magnitude of the potential optimum Δv is roughly known.
In fact, in the results obtained with this method, the angle guesses were sufficient to get some interesting results that will be presented later in Chapter 6.

The second part of the optimisation, as anticipated, consists of local optimisation, with the previous results inserted in the initial guess vector:

$$\mathbf{x}_{guess} = \begin{bmatrix} \Delta v \\ \alpha \\ \beta \\ \theta \end{bmatrix}$$

Clearly, the lower and upper bounds are restricted, especially in the case of the angle, while the impulse Δv bounds can be kept unvaried with respect to the values in Table 5.1.
The new angles constraints are centred around the guess values, with lower and upper bounds respectively shifted from the centre as $\mp\delta$. The shift parameter was tuned at a value $\delta = 5^\circ$ after some trial and error.

The local optimisation is then carried out using the MATLAB® built-in algorithm `fmincon`, utilizing the DA version of perturbing potentials in the Lagrange equations.

5.2.3. Global optimisation

The global optimisation procedure is well-known and is characterized by a high result fidelity. Its results will be used as a comparison to test the previously described optimisation algorithms.

Starting from the initial orbital parameters, the satellite orbit is integrated into a fixed period, and the resulting orbital evolution is parsed at the manoeuvring points t_m.
Subsequently, the MATLAB® built-in algorithm `particleswarm` is used, wih a population size of $N_{pop} = 100$. Inside the fitness function used for the operation, the orbit is propagated and from the results, the cost function from Eq. 5.3 is evaluated.
Since the integration is carried out at each tentative solution, the biggest drawback of the global optimisation algorithm is its heavy computational costs. Even with a lower population size, the time needed for the optimisation process is sensibly higher than the ones needed for the proposed analytical and hybrid algorithms.

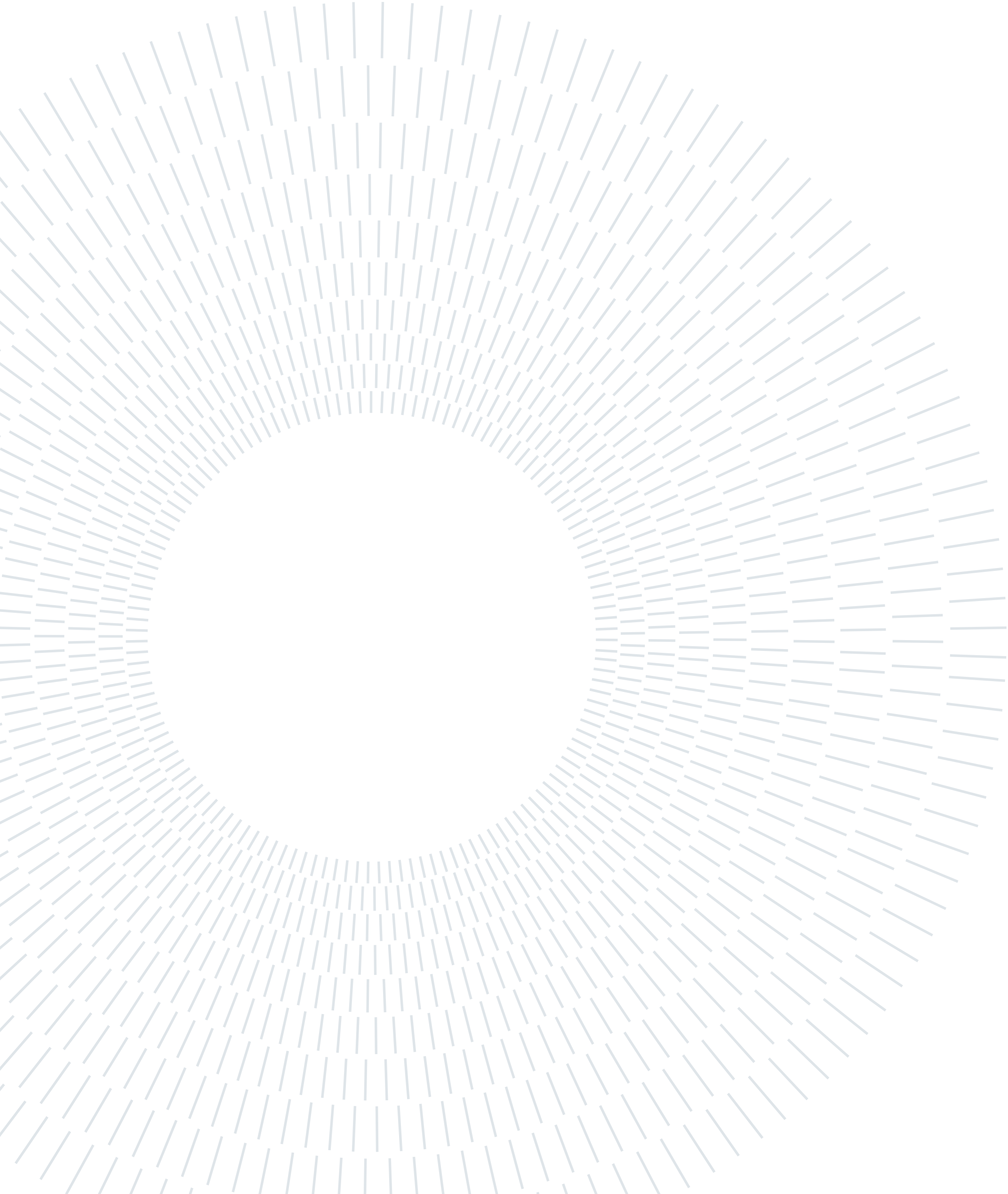

6 Case study

In chapter 5 several optimisation methods to plan EoL disposal manoeuvres were discussed, and some comparisons between the different strategies were pointed out.
In this chapter, the numerical results will be analysed in detail, applying the optimisation procedures to the test orbit and studying the effect of the suggested output manoeuvre on the satellite evolution.

6.1. Disposal optimisation mission definition

Given the scope of this thesis, an HEO satellite shall be selected for the computation, and the framework of the simulation must be defined. As already stated in Chapter 5, due to the structure of the disposal optimisation strategies under study, the manoeuvring time t_m must be defined before the computation together with the constraints of the problem.

6.1.1. INTEGRAL mission

For this purpose, once again the ESA Observatory INTEGRAL is chosen as a case study. The mission was selected in June 1993 as the next medium-size scientific mission within ESA's "Horizon 2000" program. Led by ESA, Russia and NASA contributed to the mission, respectively by providing the launcher and the ground support via Deep Space Network.
Integral was launched on 17 October 2002, its mission being the fine spectroscopy and fine imaging of celestial gamma-ray sources. To grant a long period of observation with a constant background away from trapped radiation, the spacecraft was inserted in a Highly Elliptic Orbit. [5]
INTEGRAL is now on its eleventh mission extension, with the currently planned end of the mission being December 2024, while a series of manoeuvres were executed in early 2015 to ensure compliant disposal at re-entry in early 2029. [44]
In this work, INTEGRAL will be used as a test bench to check the results of the proposed disposal optimisation strategies.

Starting on 22/03/2013, the orbital evolution was already presented in Chapter 4, comparing the results of the different propagation methods. From the results, it is clear why INTEGRAL targeted a re-entry in 2029, since the eccentricity reached its peak in that period. In fact, the minimum perigee altitude h_p is expressed as:

$$h_p = r_p - R_E = a\,(1 - e) - R_E \tag{6.1}$$

since the semi-major axis is constant, the only varying element is the eccentricity, the higher the eccentricity increments, the lower the perigee altitude.

6.1.2. optimisation framework

Given the observations made from the INTEGRAL orbital evolution, the time window for the orbital integration and the initial orbital integration is chosen starting on 22/03/2013 and propagated until 9 years later. In this period, the manoeuvring time instants t_m are parsed in 30 equispaced points.

Since the optimisation algorithms will be carried out considering several different reference frames, the overall initial conditions are reported in Table 6.1. From now on, the case scenarios of the Laplace frame defined in Section 4.3.2 will be referred to as L_i, where L stands for Laplace, and i defines the case scenario in the order they were described.

Frame	a [km]	e [-]	i [deg]	Ω [deg]	ω [deg]	θ [deg]
Ecliptic	87720	0.8766	65.70	254.83	279.02	188.30
L_1	87720	0.8766	65.43	255.30	277.90	188.30
L_2	87720	0.8766	62.43	255.12	276.11	188.30
L_3	87720	0.8766	62.43	255.12	276.11	188.30
L_4	87720	0.8766	62.60	253.78	278.63	188.30
L_5	87720	0.8766	61.62	272.04	241.36	188.30

Table 6.1: INTEGRAL mission orbital elements on 22/03/2013, various frames. L_i stands for the i-th case scenario considered for the Laplace frame from Section 4.3.2.

Note that the initial orbital parameters in Laplace frame cases 2 and 3 are the same, since at time $t = 0$ of the integration the second Laplace frame case is computed in the same manner as the rotating Laplace frame.

Regarding the optimisation setup, neither linear nor non-linear constraints are set. The only limitations are given to the variables domain, reassumed in Table 6.2

	Lower bound	Upper bound
Δv	0	150
α	$-\pi$	π
β	$-\pi$	π
θ	$-\pi/2$	$\pi/2$

Table 6.2: Lower and upper bounds of optimisation variables.

6.2. Results

In the following, the results of the optimisation will be reported and will be checked in a high-fidelity propagation if assumptions were made in the strategy definition. This is needed to check the consistency of the result in the actual satellite EoL disposal.
Starting with section 6.2.1, the global optimisation results are evaluated to serve as the benchmark for the other design strategies. In section 6.2.2 the analytical strategies are carried out and compared between each other and to the high-fidelity results given by the global optimisation.
Lastly, the hybrid approach results are computed, trying to merge the goods of the semi-analytical methods with the analytical ones, assuming the latter ones as a guess solution for local optimisation.

6.2.1. Global optimisation results

Being the benchmark for the following algorithms, in this method the orbital evolution is propagated from the initial conditions with the accurate results of the DA integration. Only the ecliptic frame will be considered in this section since given the integrating scheme, the optimal result of the global optimisation should not change with the reference frame, given that no additional assumptions are considered.
The results of the orbital evolution are parsed on 30 points in correspondence with each manoeuvring time instant t_m. Each of these parsed manoeuvre points is then passed to the global optimisation, implementing the cost function described in Eq. (5.3).

The resulting optimised manoeuvring sets $\{\Delta v, \alpha, \beta, \Theta\}$, shown in Fig. 6.1, are applied at the corresponding t_m and the results are reported in terms of minimum perigee altitude $t_{p,min}$ in Fig. (6.2). The orbital propagation is terminated if the target altitude $h_{tar} = 50$

km is achieved, with a tolerated 2% error, which in this case holds for all the resulting manoeuvres due to the aforementioned characteristics of the global optimisation.

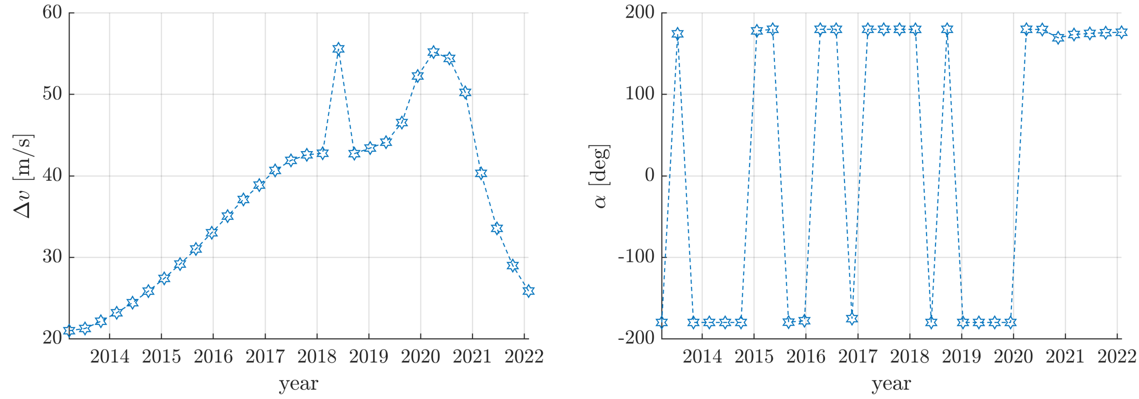

(a) Impulse magnitude Δv (b) In-plane firing angle α

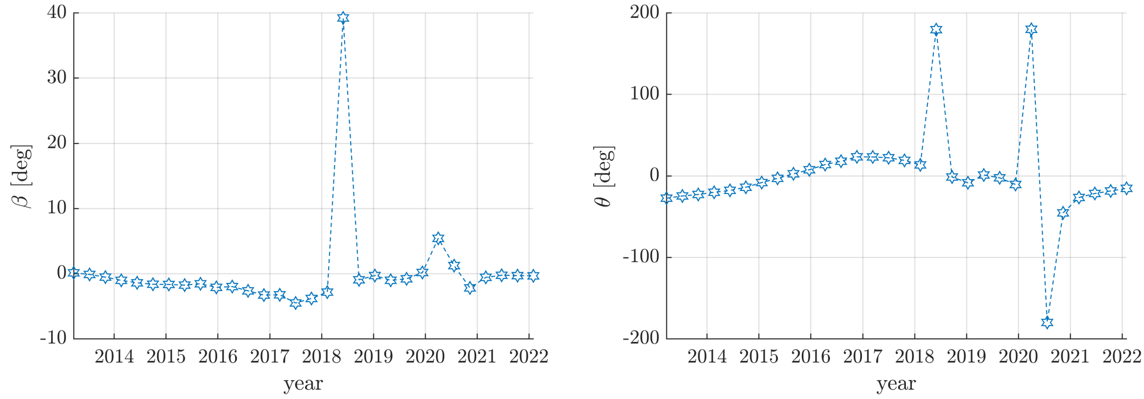

(c) Out-of-plane firing angle β (d) True anomaly at manoeuvring point θ

Figure 6.1: optimised sets of manoeuvre paramaters for each manoeuvring point t_m. Found with global optimisation using DA in ecliptic frame.

From the plots, the minimum is found in the very first manoeuvring point, while as expected the global optimiser tends to target the re-entry in 2029 due to the favourable conditions reached by the INTEGRAL satellite at that time.

The best results found by the global optimisation method are reported in Table 6.3. Note the computational time for the overall optimisation process $t_{comp} = 11$ h.

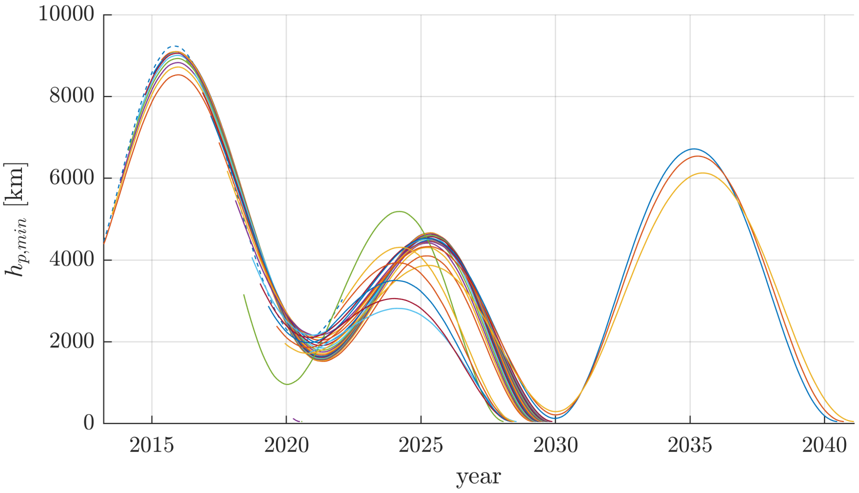

Figure 6.2: $h_{p,min}$ evolution applying the optimised manoeuvres from the global optimisation to the satellite at the corresponding t_m. to the satellite at the corresponding t_m. Propagation with DA in ecliptic frame.

t_m	Δv [m/s]	α [deg]	β [deg]	θ [deg]	t_{comp} [s]
21/03/2013	20.98	-180.00	0.12	-27.39	39554.98

Table 6.3: Best set of manoeuvre parameters. Found with global optimisation using DA in ecliptic frame.

,

6.2.2. Analytical max $(-\Delta\Theta)$ strategy results

For the analytical optimisation strategies, the orbital is propagated using the TA scheme. This is already an initial font of error remembering the results of the TA compared to the other schemes in Chapter 5, as it was observed that depending on the frames, the error may be greater or smaller, but is always present. Nonetheless, talking about reference frames, the analytical strategy is carried out using the different case scenarios of the Laplace frame described in section 4.3.2.
As before, after the TA propagation, the results are parsed in correspondence with the manoeuvring time instants t_m and are then optimised one-by-one, with the strategy that itself separates the optimisation of the angles $\{\alpha, \beta, \theta\}$ from the impulse Δv minimization.

In Section 5.2.1 two different strategies were discussed, one assuming the Hamiltonian as constant and the other considering the variation in time of the Moon orbital elements. Both of them will here be applied and compared in an environment where the assumption of time independence of the third-bodies ephemerides is dropped.

Autonomous Hamiltonian

Given the assumption $\partial\mathcal{H}/\partial t = 0$, the same is applied for the initial orbital propagation, thus neglecting the orbital variation of the Sun and the Moon, which are fixed to their initial values on 22/03/2013, the same date considered as the initial condition for the INTEGRAL satellite.

After optimising the angles through the $\max - \Delta\Theta$ method, a zero search is carried out for the Δv evaluation.

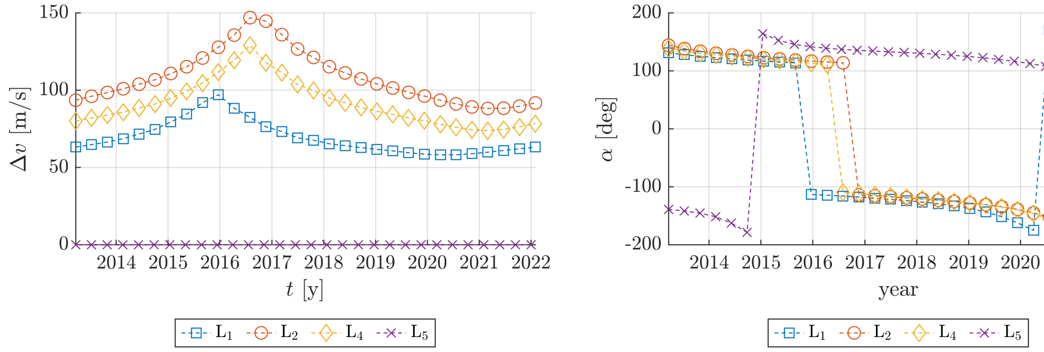

(a) Impulse magnitude Δv (b) In-plane firing angle α

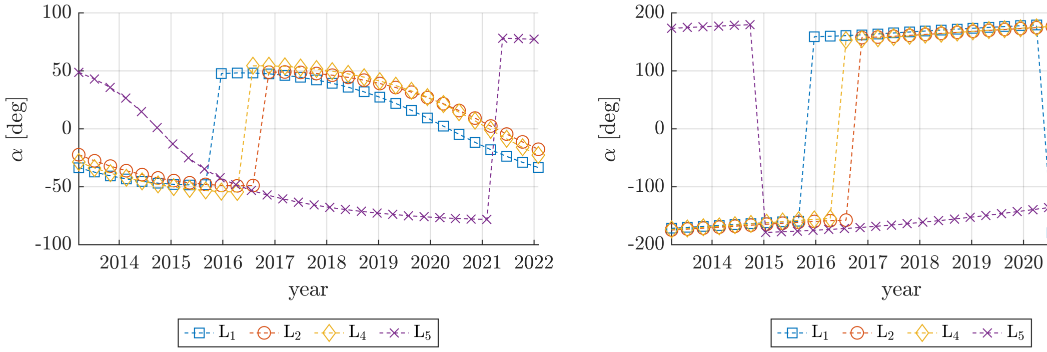

(c) Out-of-plane firing angle β (d) True anomaly at manoeuvring point θ

Figure 6.3: optimised sets of manoeuvre paramaters for each manoeuvring point t_m, found with Analytical autonomous $\mathcal{H}$ optimisation using TA in different Laplace frames case scenarios L_i.

The resulting optimised manoeuvres presented in Fig. 6.3 are thus applied to the satellite and propagated in the simplified framework described by the Laplace frame in use, considering the third-body ephemerides constant. The effect on the satellite's orbital evolution can be found in Fig. 6.4, depending on the various Laplace frames. Note that the rotating Laplace frame L_3 was not considered, since for its nature the Hamiltonian is intrinsically time-dependent for the presence of the rotation term.

The firing angles and the true anomaly are similar case by case, except for L_5, which is clearly not suitable for the manoeuvre design, as it can be seen from the results of Δv, where the output of the impulse is null. This is caused by the excessive simplification of the problem which causes the case scenario disconnection from reality, with the triple averaging propagation suggesting the atmosphere re-entry without any manoeuvring.

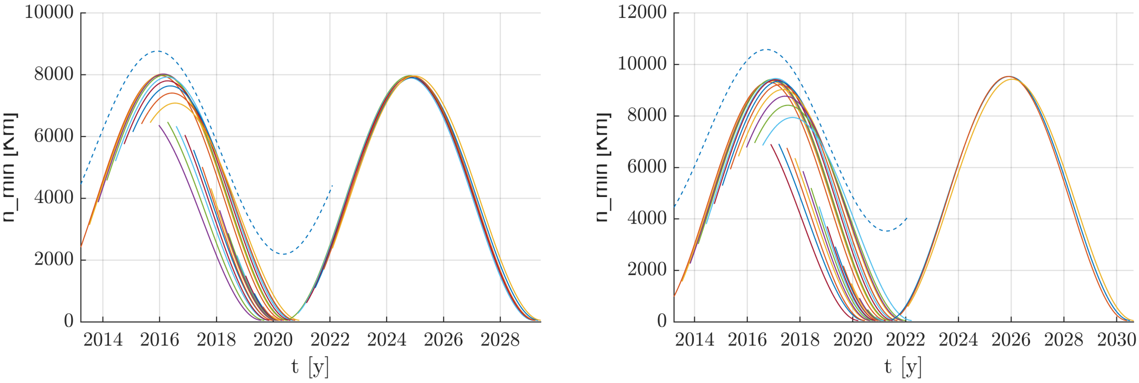

(a) Case L_1 (b) Case L_2

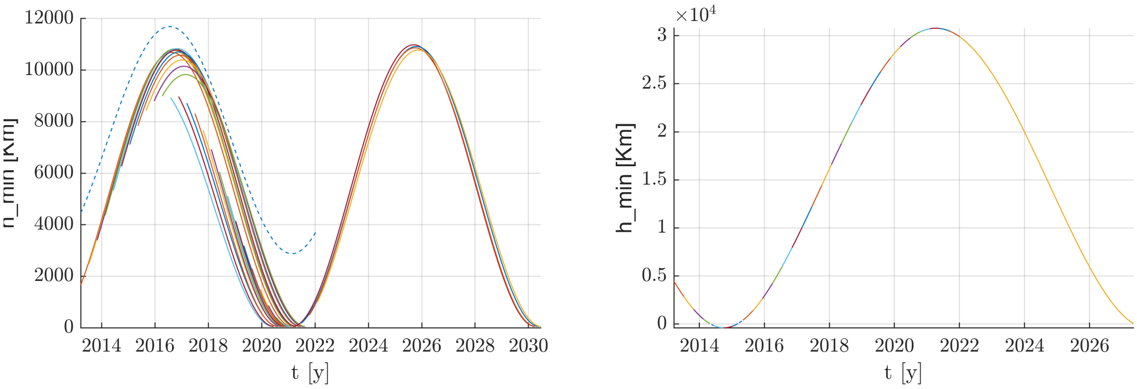

(c) Case L_4 (d) Case L_5

Figure 6.4: $h_{p,min}$ evolution applying the optimised manoeuvres from the Analytical autonomous $\mathcal{H}$ to the satellite at the corresponding t_m. Propagation with TA in different Laplace frames case scenarios L_i.

From the orbital propagation after the manoeuvre, the results are nice, but it must be remembered that those are propagated with TA and with the time-dependence neglected,

hence the results must be checked. Looking at case L_5, the TA sees an impact on the Earth without any manoeuvre needed, which is obviously false.
The found optimum set of manoeuvre parameters is reassumed in Table 6.4, with reported also the manoeuvring date.

	t_m	Δv_{opt} [m/s]	α_{opt} [deg]	β_{opt} [deg]	θ_{opt} [deg]	t_{comp} [s]
L_1	01/04/20	58.00	-172.92	3.64	179.27	109.29
L_2	22/06/21	88.27	174.59	-2.90	-179.35	117.85
L_4	02/03/21	73.95	178.46	-0.85	-179.83	156.35

Table 6.4: Best set of manoeuvre parameters found with Analytical optimisation with autonomous $\mathcal{H}$, using TA in different Laplace frames case scenarios L_i.

,

The difference with respect to the global optimisation solution is visible, both in terms of impulse magnitude and the date of manoeuvring, which was to be applied as early as 2013.

Time-dependent Hamiltonian

Differently from the previous case, the initial condition of INTEGRAL is simply propagated within the assumptions of its Laplace frame definition, with no additional simplification to the ephemerides of the third bodies.
The significant change is given by the Δv optimisation, which is carried out with a zero search algorithm of the following function:

$$\text{fun}(\Delta v) = \max\left(\mathbf{H}_{crit}(\Delta v) - \mathbf{H}(\Delta v)\right) \tag{6.2}$$

For this optimisation algorithm, the results are no longer computed into L_5 since the last result showed how its representation of the satellite dynamics is misleading. Instead, here the optimal sets are computed also within the rotating L_3 frame.

The resulting optimal set of manoeuvres reported in Fig. 6.5 are then applied to the satellite and propagated with the TA scheme and compared with the autonomous Hamiltonian manoeuvres, also propagated in a frame with varying ephemerides, in Fig. 6.6.

The results in L_3, the results are peculiar. A couple of optimised manoeuvres do not reach the target, while those with successful disposal differ from the other results.

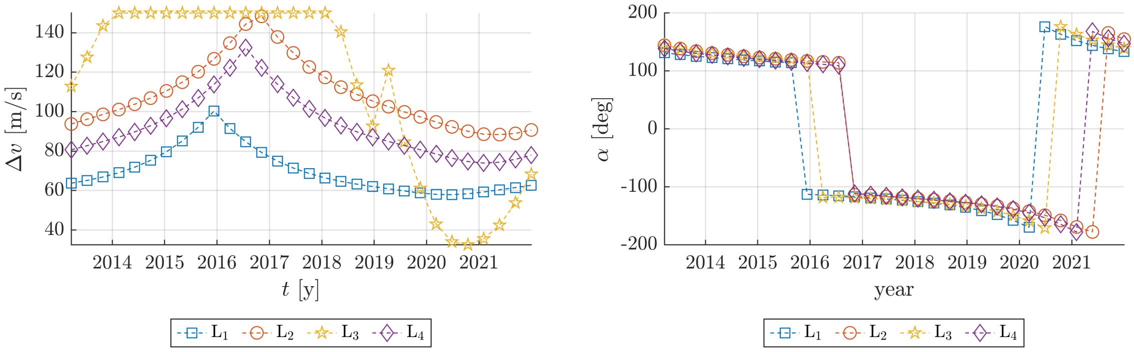

(a) Impulse magnitude Δv

(b) In-plane firing angle α

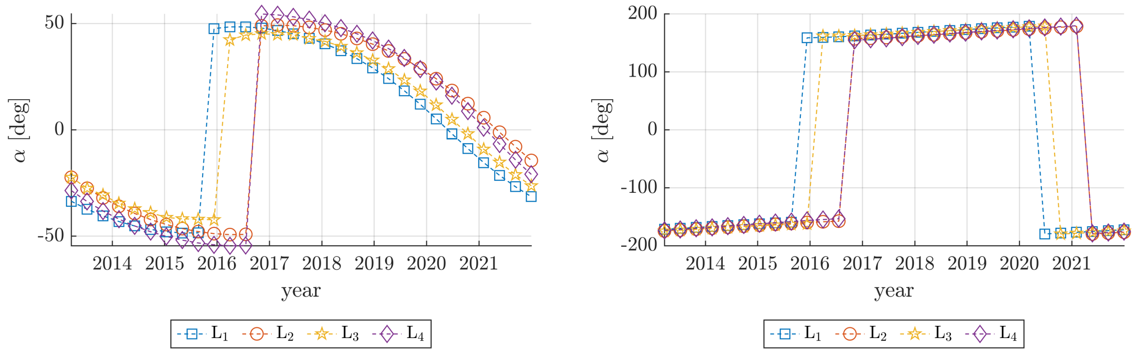

(c) Out-of-plane firing angle β

(d) True anomaly at manoeuvring point θ

Figure 6.5: optimised sets of manoeuvre paramaters for each manoeuvring point t_m. Found with Analytical time-varying $\mathcal{H}$ optimisation using TA in different Laplace frames case scenarios L_i.

At first, the algorithm gives as best impulse for the disposal the maximum equivalent to the constraint, but looking at the slope of the $h_{p,min}$ curve, it is clear not an optimal solution. After 2018 instead, the impulse magnitude decrements, with the minimum found more or less in correspondence to the other L_i scenarios, even giving the best result among all the inspected cases. That said, while the best solution has a minimum reached altitude $h_{p,min}^{opt} = 47.11$ km, some other found impulses are still overestimated looking at the propagation, with an altitude right after the manoeuvre at an impact condition.
On the other hand, the results from the other Laplace frame scenarios show some minor adjustments to the impulses with respect to the previous analytic design strategy, to account for the added complexity of the system's dynamics. Propagating with TA, while in L_1 only a few results do not reach the target altitude, in L_2 and L_4 the disposal is successful, even if once again the results must be checked with the DA orbital propaga-

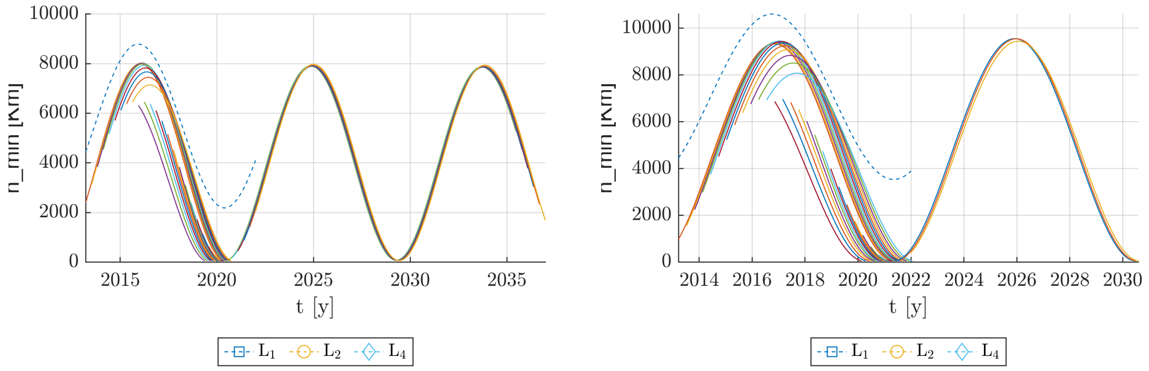

(a) Case L_1 (b) Case L_2

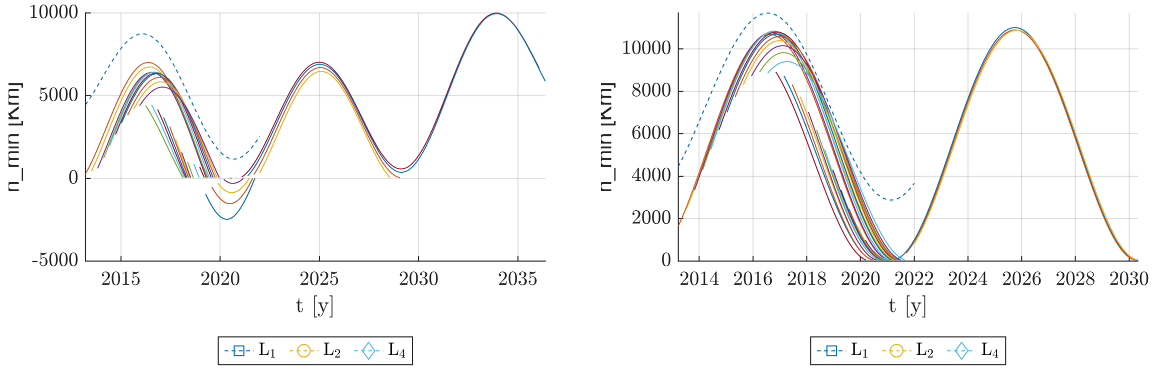

(c) Case L_3 (d) Case L_4

Figure 6.6: $h_{p,min}$ evolution applying the optimised manoeuvres from the Analytical time-varying $\mathcal{H}$ to the satellite at the corresponding t_m. Propagation with TA in different Laplace frames case scenarios L_i.

tion. Note that the time period where all the analytical results tend to find the optimal manoeuvres is more or less the time in which the argument of perigee is $\omega_{☾} \approx 180°$.

The optimal sets among the proposed manoeuvres are reported in Table 6.5 together with the L_i scenario considered.

One important note is that the L3 results reported are obtained within employing TA potentials but maintaining the full rotational potential, which is equal to the DA one since no dependence on the fast angles is present.
If the TA version of the rotational potential is used instead, the results in Fig. 6.7

	t_m	Δv_{opt} [m/s]	α_{opt} [deg]	β_{opt} [deg]	θ_{opt} [deg]	t_{comp} [s]
L_1	26/06/20	57.93	176.64	-1.85	-179.63	422.42
L_2	24/05/21	88.38	-177.92	-1.11	-179.75	397.31
L_3	15/10/20	32.54	176.48	-1.84	-179.68	898.93
L_4	02/02/21	73.95	-178.03	1.09	-179.78	462.14

Table 6.5: Best set of manoeuvre parameters found with Analytical optimisation with time-dependent $\mathcal{H}$, using TA in different Laplace frames case scenarios L_i.

,

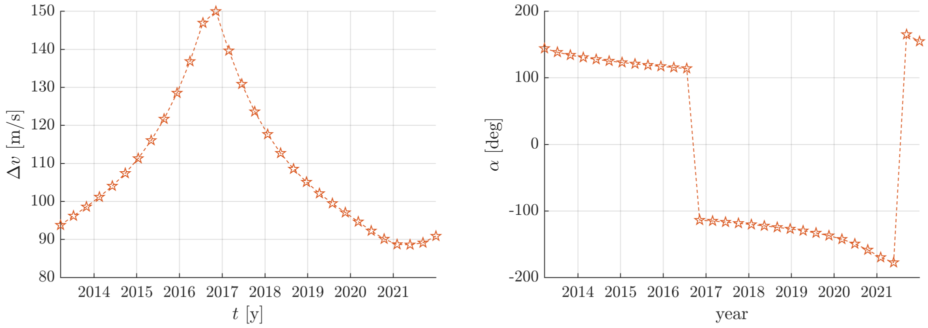

(a) Impulse magnitude Δv (b) In-plane firing angle α

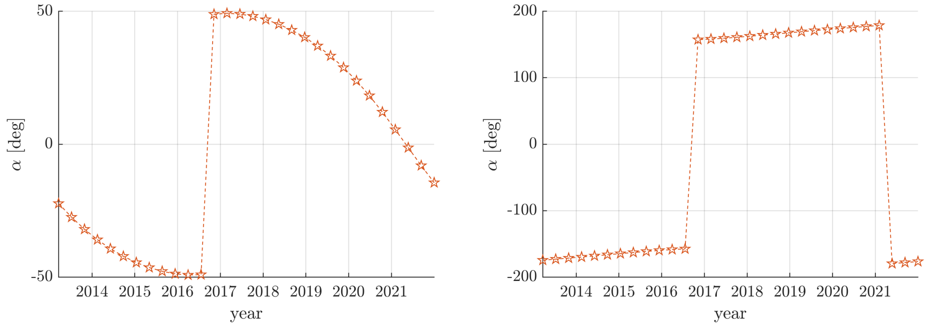

(c) Out-of-plane firing angle β (d) True anomaly at manoeuvring point θ

Figure 6.7: optimised sets of manoeuvre paramaters for each manoeuvring point t_m. Found with Analytical time-varying $\mathcal{H}$ optimisation using TA $\overline{\overline{\overline{R}}}_{rot}$ in L_3.

Lastly, as a matter of comparison, the results from the autonomous Hamiltonian propagated with time-varying ephemerides of the third bodies are reported in Fig. 6.8, where the red markers represent an unsuccessful re-entry ($h_{p,min} > h_{p,tar}$). Here a large amount of optimum manoeuvres does not reach the target, so even if the magnitude of the impulse found by the time-varying Hamiltonian did not change much from the previous strategy, the results are different.

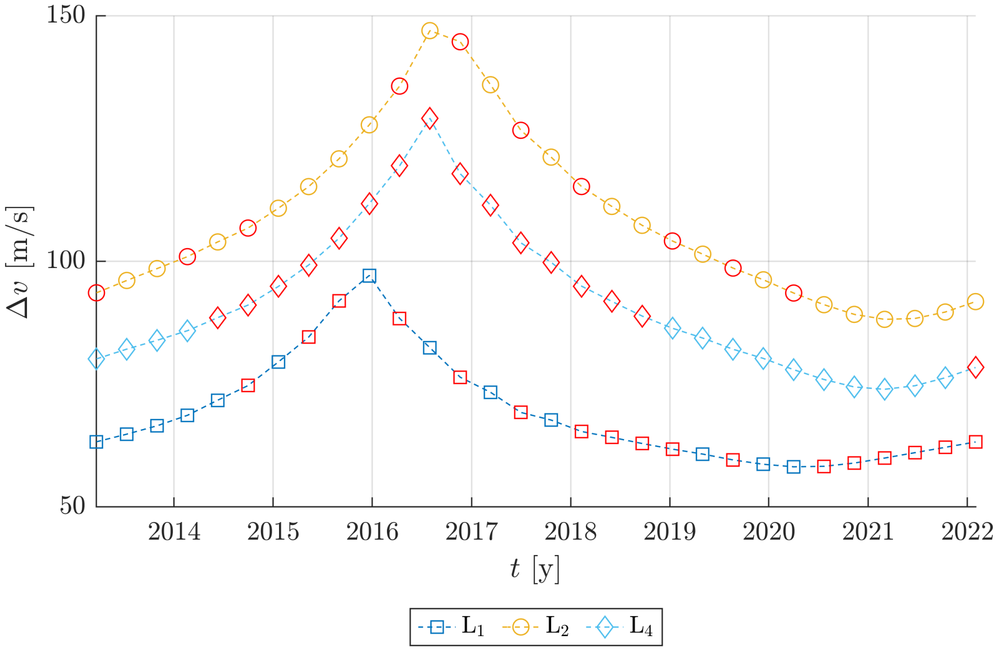

Figure 6.8: Analytical autonomous $\mathcal{H}$ solution propagated with TA considering time-varying third-bodies' orbital elements. Different Laplace frames L_i are considered. Red markers represents a failed re-entry ($h_{p,min} > h_{p,tar}$).

Analytic resulting manoeuvres check

Given the optimised set of manoeuvre parameters, resulting from the analytic design strategy considering the time dependence of the Hamiltonian, their validity in the real-case scenario needs to be checked.

Since the optimisation strategy is supposed to take place at the time of the initial orbital condition, in the case considered on 22/03/2013, to design the EoL disposal, the validity test will be carried out with a DA orbital propagation from the initial condition for the 9 years considered for the application of the manoeuvre.

The DA-integrated orbital elements are then parsed in the same way as before, into the manoeuvring points t_m.

At each parsed manoeuvring point, the corresponding impulse is applied to the satellite. Subsequently, the orbital state is again propagated with the DA potentials for 25 years to verify if the satellite would eventually reach the target altitude.

The propagation is carried out into the ecliptic frame without any added assumptions to the dynamics, apart from the long-term evaluation filtering on the fast angles inherent to the DA technique.

The results of this procedure are reported in Fig. 6.9, with a red marker if the target is not respected.

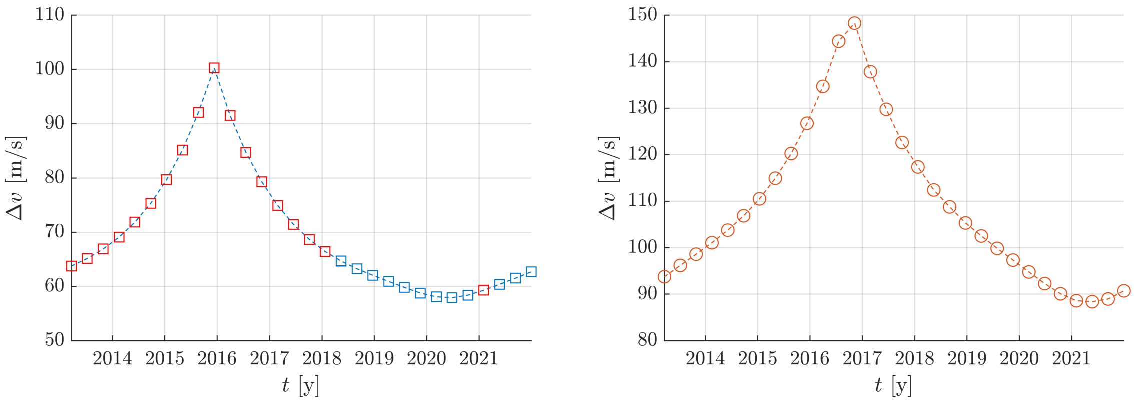

(a) Case L_1 (b) Case L_2

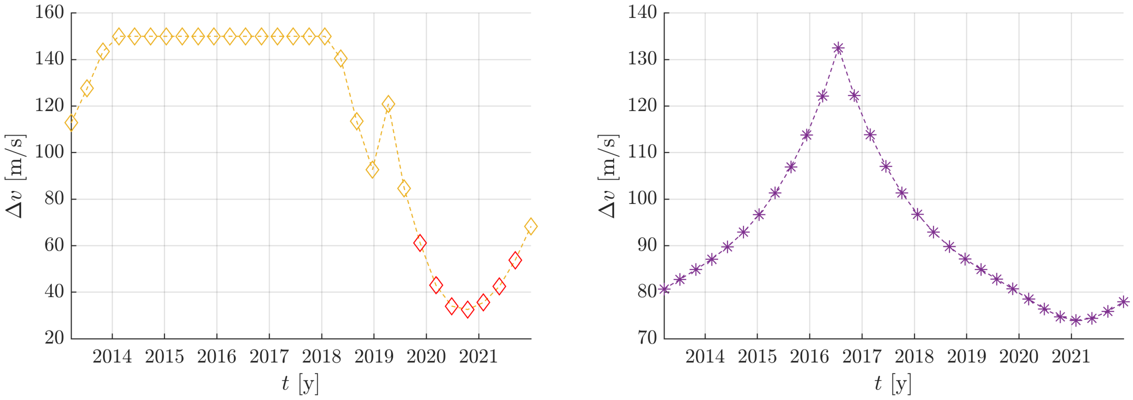

(c) Case L_3 (d) Case L_4

Figure 6.9: Analytic time-varying $\mathcal{H}$ optimisation check with DA. The red marker represents a failed re-entry ($h_{p,min} > h_{p,tar}$).

It can be observed that, for the L_1 case considered, the optimum set found re-entry is satisfied, while the worst results are obtained within the first half of the manoeuvring point, where the optimised manoeuvres do not reach the disposal target.

The rotating Laplace frame L_3, on the contrary, satisfies the target requirement with the first results characterised by a noticeable impulse overestimation, while the optimum set does not bring to an effective real case re-entry. Therefore, given the issues in the application of the analytical time-dependent design to the L_3 case, a proper re-design of the optimising function from Eq. 6.2 focusing on the rotating Laplace frame scenario may give better results.

On the other hand, cases L_2 and L_4 show some interesting results. All the manoeuvring sets correspond to a successful re-entry in the real case propagation with DA, with the "average" Laplace plane showing generally better results.

6.2.3. Hybrid strategy results

Finally, the hybrid disposal optimisation strategy is analysed. Here, contrarily to the analytic computation scenario, the initial conditions evolution is carried out with the DA technique and subsequently parsed in the manoeuvring points t_m.

Exploiting the phase space formulation, the analytical $\max(-\Delta\Theta)$ design strategy with time-dependent Hamiltonian is used for the computation of the angles $\{\alpha, \beta, \theta\}$. Those are used as initial guesses for the local optimisation together with a guess value that can be either found with the analytical strategy or if the magnitude is more or less it can be simply fixed with this knowledge.
Local optimisation, on the other hand, is executed by integrating the DA method without imposing additional assumptions, even those utilized in defining the Laplace frame. This method of integration was previously employed in Section 4.3.2. As anticipated, it was observed that by releasing all assumptions, the eccentricity remains constant between different frames.

When comparing the resulting orbital propagation after optimising and applying the impulse within this assumption-free propagation framework, the outcomes depicted in Fig. 6.10 are obtained. L_3 is not considered since its computational cost for the DA propagation is sensibly more expensive than the others, nullifying the advantages of the design strategy.
As anticipated, the minimum Δv remains consistent across all considered frames, validating the method's independence from the chosen frame.
The minimum impulse is found at $\Delta v \approx 40$ m/s in all the frames considered, with a computational time clearly higher with respect to the analytical ones, but lower with respect to the global one.

Note that even with L_5 the results are now consistent with the real case, due to its dynamics not being any more related to its particular frame definition. While the others' results are more or less comparable with one another in all the time domains, here the impulses show a different optimisation development, starting from higher values and then decreasing towards the 40 m/s value. This is related to the different suggested angles for the manoeuvres, as shown in Fig. 6.11. Conversely, after 2020, the set of manoeuvring angles is re-aligned to the other frames' results, thus reaching a similar optimum Δv.

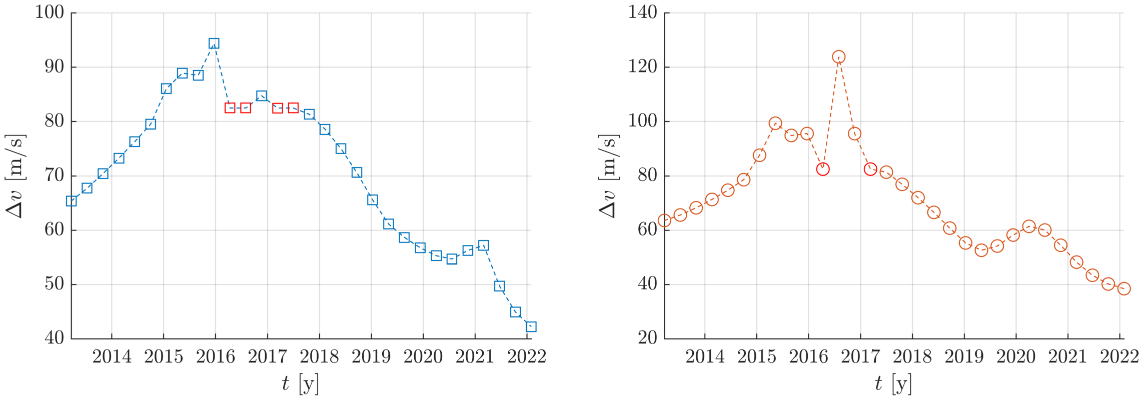

(a) Frame L_1

(b) Frame L_2

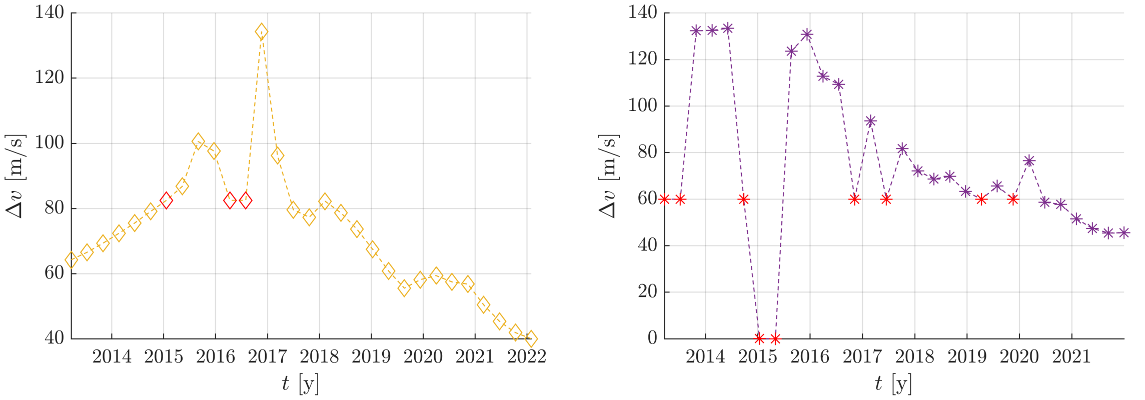

(c) Frame L_4

(d) Frame L_5

Figure 6.10: optimised impulse magnitude Δv for each manoeuvring point t_m, found with Hybrid optimisation using DA in different Laplace frames propagated without any additional assumption L_i.

	t_m	Δv_{opt} [m/s]	α_{opt} [deg]	β_{opt} [deg]	θ_{opt} [deg]	t_{comp}
L_1	31/01/22	42.23	132.72	-29.83	-173.03	6101.59
L_2	31/01/22	38.45	122.12	41.03	-69.95	7034.62
L_4	31/01/22	40.00	2.19	-0.59	-2.99	7001.60
L_5	11/12/21	45.50	133.09	-75.16	-173.44	9113.63

Table 6.6: Best set of manoeuvre parameters found with Hybrid optimisation, using DA in different Laplace frames case scenarios L_i.

,

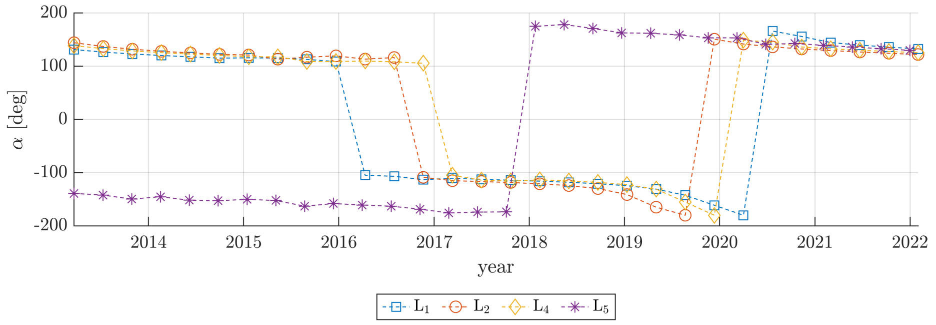

(a) In-plane firing angle α

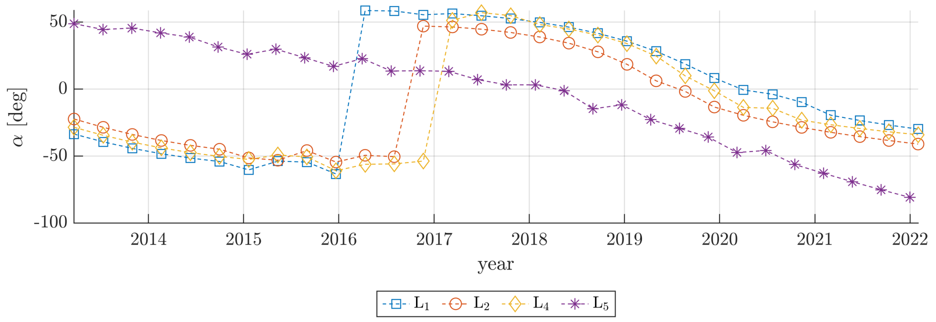

(b) Out-of-plane firing angle β

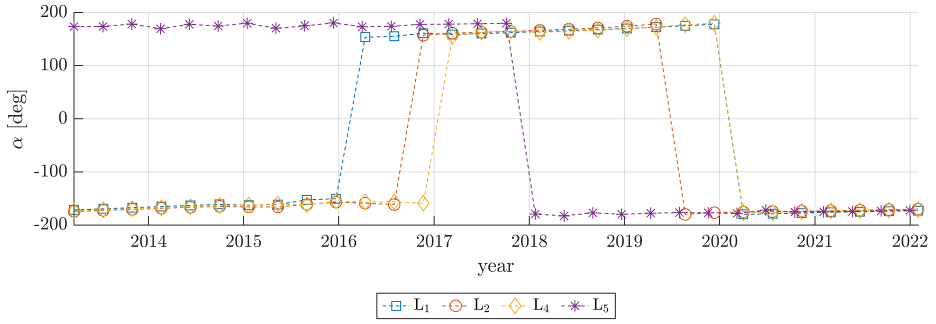

(c) True anomaly at manoeuvring point θ

Figure 6.11: optimised set of manoeuvring angles $\{\alpha, \beta, \theta\}$ for each manoeuvring point t_m, found with Hybrid optimisation using DA in different Laplace frames propagated without any additional assumption L_i.

7 | Conclusion

The objective of this thesis was to explore the implementation of an analytical end-of-life disposal strategy. This aimed at reducing computational costs and equipping spacecraft with the capability to autonomously plan manoeuvres, ensuring compliance with the IADC guidelines concerning space debris.

Following the results obtained in previous works, the dynamical model was therefore reduced by means of triple-averaged perturbing potentials, which were exploited both for a low-cost propagation method and used within the Hamiltonian formulation to define the manoeuvre optimisation strategy.
Differently from those works, This thesis introduces an approach that takes into account the time variation of the orbital elements of third bodies, by explicitly outlining the time variation inside a vector of Hamiltonians at different time instants. Even this way, some simplifications were necessary. The orbital elements variation of the satellite itself was kept constant since their variation can be computed only by integrating the dynamics.
Applying the optimisation scheme to the INTEGRAL satellite as a case study, and considering different Laplace frames scenarios, it was shown that the optimisation algorithm was capable of re-adjusting the set of manoeuvre parameters to account for the variation of the third-bodies' ephemerides, as the target re-entry was easily reached within the TA formulation of the dynamics.
Nonetheless, the consideration of the time variation allowed the exploitation of the rotating Laplace frame. Even if some issues were found in the optimisation result within this frame, the orbital propagation in L_3 highlighted interesting results.
All the results found with the proposed optimisation design were then checked. This was done by applying the manoeuvres within a DA model representing the real case dynamics, with no more assumptions than the filtered effect of the fast angles. The results highlighted that, even if overestimated, the optimisation manoeuvres were capable of reaching the target altitude. for the fixed L_1 frame, 12 out of 30 manoeuvring points were successful, including the best solution found. Regarding the rotating L_3, only 7 points were not re-entering, but it must be considered that the first half of the optimised manoeuvres are noticeably overestimated, and in 14 sets, the impulse was the maximum allowed by

optimisation constraint, while the overall best manoeuvring set failed the re-entry condition. Nonetheless, cases L_2 and L_4 were very positive in terms of actual re-entry, with all points reaching the target. This highlights the actual possibility for autonomous in-space manoeuvring by the satellite, without needing the ground station support, at the cost of a sub-optimal manoeuvre requiring higher impulse compared to the best possible solution.

Furthermore, a hybrid optimisation method was proposed, trying to combine the set of optimised angles through the exploitation of the maximum variation of the negative Kozai parameter $-\Delta\Theta$ with a local optimiser. The design consisted of propagating with the DA potentials the orbital elements from the initial conditions, then analytically computing the best set of manoeuvring angles in parsed time instants (each one optimised independently), and finally proceeding with the local optimisation using the DA integration once again.
The results demonstrated effective performance in identifying successful re-entry manoeuvres, albeit requiring higher impulses compared to the benchmark solution from global optimisation. However, this was achieved with a reduced computational cost.
In addition, as was expected, the results more or less converged to the same manoeuvre, highlighting an independence from the Laplace frame considered which was not the case in the analytical results.

Also, the optimised manoeuvres within different frames converged to similar solutions, showing they didn't rely on the specific Laplace frame used. In this sense, the behaviour of the hybrid algorithm is different from the analytic solution, as was expected.

In light of the obtained results, future work may focus on the exploitation of the rotating Laplace frame, looking for a best-suited analytical optimisation function for that particular case which may give better results.

Bibliography

[1] D. J. Kessler and B. G. Cour-Palais. Collision frequency of artificial satellites: The creation of a debris belt. *Journal of Geophysical Research: Space Physics*, 83(A6): 2637–2646, 1978. doi: https://doi.org/10.1029/JA083iA06p02637.

[2] D.J. Kessler, N.L. Johnson, J.-C Liou, and M. Matney. The kessler syndrome: Implications to future space operations. *Advances in the Astronautical Sciences*, 137:47–62, 01 2010.

[3] ESA Space Debris Office. ESA's annual space environment report, 2023. URL `https://www.sdo.esoc.esa.int/environment_report/Space_Environment_Report_latest.pdf`.

[4] IADC. IADC space debris mitigation guidelines, 2020. URL `https://orbitaldebris.jsc.nasa.gov/library/iadc-space-debris-guidelines-revision-2.pdf`.

[5] C. Winkler. The INTEGRAL mission. *Experimental Astronomy*, 6(4):71–76, December 1995. ISSN 1572-9508. doi: 10.1007/BF00419260. URL `https://doi.org/10.1007/BF00419260`.

[6] M.L. Lidov. The evolution of orbits of artificial satellites of planets under the action of gravitational perturbations of external bodies. *Planetary and Space Science*, 9(10):719–759, 1962. ISSN 0032-0633. URL `https://doi.org/10.1016/0032-0633(62)90129-0`.

[7] Y. Kozai. Secular perturbations of asteroids with high inclination and eccentricity. *The Astronomical Journal*, 67:591–598, November 1962. doi: 10.1086/108790.

[8] B. Kaufman. Variation of parameters and the long-term behavior of planetary orbiters. In *Astrodynamics Conference*, 1970. doi: 10.2514/6.1970-1055.

[9] B. Kaufman and R. Dasenbrock. Higher Order Theory for Long-Term Behavior of Earth and Lunar Orbiters. In *Astrodynamics Conference*. The American Institute of Aeronautics and Astronautics;, 1972.

[10] ESA. Space debris mitigation: the case for a code of conduct, 2005. URL `https://www.esa.int/Enabling_Support/Operations/Space_debris_mitigation_the_case_for_a_code_of_conduct`.

[11] N. Delsate, P. Robutel, A. Lemaître, and T. Carletti. Frozen Orbits at high eccentricity and inclination: Application to Mercury orbiter. *Celestial Mechanics & Dynamical Astronomy*, 108, March 2010. doi: 10.1007/s10569-010-9306-2.

[12] E. Tresaco, J. Carvalho, and A. Elipe. Frozen Orbits for a Solar Sail Around Mercury. *Journal of Guidance Control and Dynamics*, 39, February 2016. doi: 10.2514/1.G001510.

[13] D.J. Scheeres, M.D. Guman, and B.F. Villac. Stability Analysis of Planetary Satellite Orbiters: Application to the Europa Orbiter. *Journal of Guidance, Control, and Dynamics*, 24(4):778–787, 2001. doi: 10.2514/2.4778. URL `https://doi.org/10.2514/2.4778`.

[14] M. Lara and J.F. San Juan. Dynamic Behavior of an Orbiter around Europa. *Journal of Guidance, Control, and Dynamics*, 28(2):291–297, 2005. doi: 10.2514/1.5686. URL `https://doi.org/10.2514/1.5686`.

[15] J. Carvalho, D. Mourão, A. Elipe, R. Vilhena de Moraes, and A. Prado. Frozen orbits around Europa. *International Journal of Bifurcation and Chaos in Applied Sciences and Engineering*, 22, October 2012. doi: 10.1142/S0218127412502409.

[16] D. Folta and D. Quinn. Lunar Frozen Orbits. In *AIAA/AAS Astrodynamics Specialist Conference and Exhibit*, 2006. doi: 10.2514/6.2006-6749. URL `https://arc.aiaa.org/doi/abs/10.2514/6.2006-6749`.

[17] A. Abad, A. Elipe, and E. Tresaco. Analytical Model to Find Frozen Orbits for a Lunar Orbiter. *Journal of Guidance Control and Dynamics*, 32:888–898, May 2009. doi: 10.2514/1.38350.

[18] H. Lévy, É. Joffre, S. Lizy-Destrez, and M. Zamaro. STORM: A semi-analytical orbit propagator for assessing the compliance with Mars Planetary Protection Requirements. *Acta Astronautica*, 190:118–133, 2022. ISSN 0094-5765. doi: https://doi.org/10.1016/j.actaastro.2021.09.027.

[19] F. Deleflie, A. Rossi, C. Portmann, G. Métris, and F. Barlier. Semi-analytical investigations of the long term evolution of the eccentricity of Galileo and GPS-like orbits. *Advances in Space Research*, 47:811–821, March 2011. doi: 10.1016/j.asr.2010.11.038.

[20] J. Radtke, R. Domínguez-González, S. Flegel, N. Sánchez-Ortiz, and K. Merz. Impact of eccentricity build-up and graveyard disposal Strategies on MEO navigation constellations. *Advances in Space Research*, 56:2626–2644, December 2015. doi: 10.1016/j.asr.2015.10.015.

[21] D.J. Gondelach, R. Armellin, and A. Wittig. On the predictability and robustness of Galileo disposal orbits. *Celestial Mechanics and Dynamical Astronomy*, 131(12): 60, November 2019. ISSN 1572-9478. doi: 10.1007/s10569-019-9938-9. URL `https://doi.org/10.1007/s10569-019-9938-9`.

[22] J. Daquin, E. Legnaro, I. Gkolias, and C. Efthymiopoulos. A deep dive into the $2g + h$ resonance: separatrices, manifolds and phase space structure of navigation satellites. *Celestial Mechanics and Dynamical Astronomy*, 134(1):6, January 2022. ISSN 1572-9478. doi: 10.1007/s10569-021-10060-6. URL `https://doi.org/10.1007/s10569-021-10060-6`.

[23] M. M. Pellegrino, D.J. Scheeres, and B.J. Streetman. Characterizing doubly-averaged dynamical models in medium earth orbit. *Acta Astronautica*, 194: 126–144, 2022. ISSN 0094-5765. doi: https://doi.org/10.1016/j.actaastro.2021.12.057.

[24] A.J. Rosengren, D.J. Scheeres, and J.W. McMahon. The classical laplace plane as a stable disposal orbit for geostationary satellites. *Advances in Space Research*, 53(8): 1219–1228, 2014. ISSN 0273-1177. doi: https://doi.org/10.1016/j.asr.2014.01.034.

[25] I. Gkolias and C. Colombo. Towards a sustainable exploitation of the geosynchronous orbital region. *Celestial Mechanics and Dynamical Astronomy*, 131 (4):19, 2019. ISSN 1572-9478. doi: 10.1007/s10569-019-9895-3. URL `https://doi.org/10.1007/s10569-019-9895-3`.

[26] J. Carvalho, R. Moraes, and A. Prado. Analysis of the orbital evolution of space debris using a solar sail and natural forces. *Advances in Space Research*, 70, April 2022. doi: 10.1016/j.asr.2022.04.014.

[27] A. Pinardell Pons and R. Noomen. Ariane 5 gto debris mitigation using natural perturbations. *Advances in Space Research*, 63(7):1992–2002, 2019. ISSN 0273-1177. doi: https://doi.org/10.1016/j.asr.2018.12.001.

[28] C. Colombo, E.M. Alessi, and M. Landgraf. End-of life disposal of spacecraft in highly elliptical orbits by means of luni-solar perturbations and moon resonances. *Earth*, 3(2):2–2, 2013.

[29] C. Colombo. Long-Term Evolution of Highly-Elliptical Orbits: Luni-Solar Perturbation Effects for Stability and Re-entry. *Frontiers in Astronomy and Space Sciences*, 6, July 2019. doi: 10.3389/fspas.2019.00034.

[30] M. Asperti. Analytical design of end-of-life disposal manoeuvres in the perturbed phase space. Master's thesis, Politecnico di Milano, 2021. Faculty of Industrial Engineering, Department of Aerospace Science and Technologies, Master in Space Engineering, Supervisor: Colombo, C. Co-supervisor: X. Lu and I. Gkolias.

[31] F. Scala. Analytical design of end-of-life disposal manoeuvres for highly elliptical orbits under the influence of the third body's attraction and planet's oblateness. Master's thesis, Politecnico di Milano, 2018. Faculty of Industrial Engineering, Department of Aerospace Science and Technologies, Master in Space Engineering, Supervisor: C. Colombo, Co-supervisor: I. Gkolias.

[32] M. Valtonen and H. Karttunen. *The Three-Body Problem.* Cambridge University Press, 2006. doi: 10.1017/CBO9780511616006.

[33] D.A. Vallado and W.D. McClain. *Fundamentals of Astrodynamics and Applications.* Fundamentals of Astrodynamics and Applications. Microcosm Press, 2001. ISBN 9781881883128.

[34] P.E. El'iasberg. *Introduction to the Theory of Flight of Artificial Earth Satellites.* Mechanics of space flight. Israel Progr.for Scientific Transl., 1967.

[35] H.D. Curtis. *Orbital Mechanics for Engineering Students.* Aerospace Engineering. Elsevier Science, 2013. ISBN 978-0-08-097748-5.

[36] L. Blitzer. Handbook of orbital perturbations. *University of Arizona*, page 36, 1970.

[37] C.D. Murray and S.F. Dermott. The Disturbing Function. In *Solar System Dynamics*, pages 225–273. Cambridge University Press, 2000. doi: 10.1017/CBO9781139174817.007.

[38] C. Colombo, F. Letizia, E.M. Alessi, and M. Landgraf. End-of-life Earth re-entry for highly elliptical orbits: the INTEGRAL mission. In *Advances in the Astronautical Sciences*, volume 152, January 2014.

[39] R. R. Allan, G. E. Cook, and Michael James Lighthill. The long-period motion of the plane of a distant circular orbit. *Proceedings of the Royal Society of London. Series A. Mathematical and Physical Sciences*, 280(1380):97–109, 1964. doi: 10.1098/rspa.1964.0133.

[40] J.R. Wertz. *Spacecraft Attitude Determination and Control.* Astrophysics and Space Science Library. Springer Netherlands, 1978. ISBN 9789027709592.

[41] E. de Pasquale, L. Francillout, J.J. Wasbauer, J. Hatton, J. Albers, and D. Steele. ATV jules verne reentry observation: Mission design and trajectory analysis. In *2009 IEEE Aerospace conference*, pages 1–16, 2009. doi: 10.1109/AERO.2009.4839703.

[42] P.C. Austin, D.S. Lee, and J.P. Fine. Introduction to the analysis of survival data in the presence of competing risks. *Circulation*, 133(6):601–609, 2016. doi: 10.1161.115.017719.

[43] C. Colombo. *Optimal trajectory design for interception and deflection of Near Earth Objects.* PhD thesis, University of Glasgow, 2010.

[44] ESA. Integral operations. URL `https://www.esa.int/Enabling_Support/Operations/Integral_operations`.

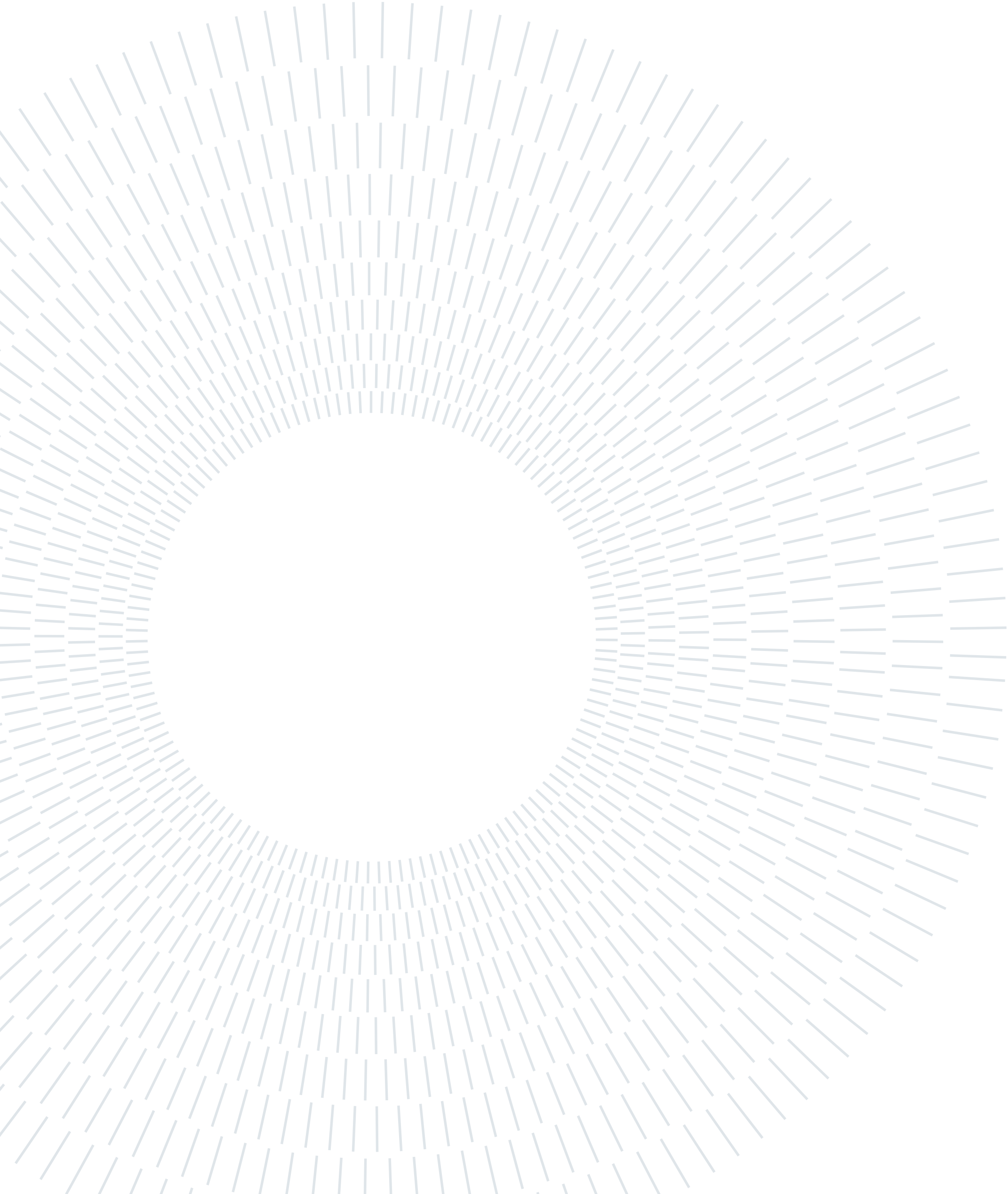

A| Appendix A

A.1. Integration of the TA terms for $\overline{\overline{\overline{\mathcal{R}}}}_{3b,3}$

$$\begin{aligned}\frac{1}{2\pi}\int_0^{2\pi}\alpha^3 d\Omega = {} & \frac{1}{256}\sin i\sin i_{3b}\sin\omega\big[6\big(34+6\cos 2i+5\cos 2(i-i_{3b})+14\cos 2i_{3b}\\ & +5\cos 2(i+i_{3b})+4\big(3+5\cos 2i_{3b}\big)\cos 2\omega\sin^2 i\big)\sin\omega_{3b}\\ & +8\big(7+5\cos 2i+10\cos 2\omega\sin^2 i\big)\sin^2 i_{3b}\sin 3\omega_{3b}\big]\end{aligned} \tag{A.1}$$

$$\begin{aligned}\frac{1}{2\pi}\int_0^{2\pi}\beta\gamma\xi d\Omega = {} & \frac{1}{128}\left[-16\cos\omega\cos\omega_{3b}\sin 2i\sin 2i_{3b}+\right.\\ & \sin i\left[-\left(10+7\cos 2(i-\omega)+7\cos 2(i+\omega)-6\cos 2\omega_{3b}+\right.\right.\\ & 2\cos 2i\{7+15\cos 2\omega_{3b}\}-2\cos 2\omega\{7+30\cos 2\omega_{3b}\sin^2 i\}\big)\sin i_{3b}\\ & +4\cos^2 2\omega_{3b}\left(-1+5\cos 2i-10\cos 2\omega\sin^2 i\right)\sin 3i_{3b}\big]\sin\omega\sin\omega_{3b}\big]\end{aligned} \tag{A.2}$$

$$\frac{1}{2\pi}\int_0^{2\pi}\alpha d\Omega = \sin i\sin i_{3b}\sin\omega\sin\omega_{3b} \tag{A.3}$$

$$\begin{aligned}\frac{1}{2\pi}\int_0^{2\pi}\alpha\beta^2 d\Omega = {} & \frac{1}{128}\big(32\cos\omega\cos\omega_{3b}\sin 2i\sin 2i_{3b}+\\ & \sin i\big(54-7\cos 2(i-\omega)-7\cos 2(i+\omega)+6\cos 2\omega_{3b}-\\ & 2\cos 2i\big(7+15\cos 2\omega_{3b}\big)+2\cos 2\omega\big(7+30\cos 2\omega_{3b}\sin^2 i\big)\big)\sin i_{3b}+\\ & 4\cos^2\omega_{3b}\big(-1+5\cos 2i-10\cos 2\omega\sin^2 i\big)\sin 3i_{3b}\big)\sin\omega\sin\omega_{3b}\end{aligned} \tag{A.4}$$

$$\begin{aligned}\frac{1}{2\pi}\int_0^{2\pi}\alpha\gamma^2 d\Omega = {} & \frac{1}{128}\sin i\sin i_{3b}\sin\omega\big(34+6\cos 2i+5\cos 2(i-i_{3b})+14\cos 2i_{3b}+\\ & 5\cos 2(i+i_{3b})+4\big(3+5\cos 2i_{3b}\big)\cos 2\omega\sin^2 i\big)\sin\omega_{3b}-\\ & 4\big(7+5\cos 2i+10\cos 2\omega\sin^2 i\big)\sin^2 i_{3b}\sin 3\omega_{3b}\end{aligned} \tag{A.5}$$

$$\frac{1}{2\pi}\int_0^{2\pi}\alpha\xi^2 d\Omega = \frac{1}{128}\sin i\sin i_{3b}\sin\omega\big(22+18\cos 2i+15\cos 2(i-i_{3b})-6\cos 2i_{3b}+ \\ 15\cos 2(i+i_{3b})-12\big(3+5\cos 2i_{3b}\big)\cos 2\omega\sin^2 i\big)\sin\omega_{3b}+ \\ 4\Big(-1+5\cos 2i-10\cos 2\omega\sin^2 i\Big)\sin^2 i_{3b}\sin 3\omega_{3b} \tag{A.6}$$

A.2. Integration of the TA terms for $\overline{\overline{\overline{\mathcal{R}}}}_{3b,4}$

$$\frac{1}{2\pi}\int_0^{2\pi} 1 d\Omega = 1 \tag{A.7}$$

$$
\begin{aligned}
&\frac{1}{2\pi}\int_0^{2\pi}(\beta^2+\xi^2)\beta^2 d\Omega = \frac{1}{32768}\big[9156 + 1232\cos 2i + 108\cos 4i + 120\cos 2(i-2i_{3b})+\\
&120\cos 4i - 2i_{3b} + 1824\cos 2(i-i_{3b}) + 210\cos 4(i-i_{3b}) + 1232\cos 2i_{3b} + 108\cos 4i_{3b}+\\
&1824\cos 2(i+i_{3b}) + 210\cos 4(i+i_{3b}) + 120\cos 2(2i+i_{3b}) + 120\cos 2(i+2i_{3b})-\\
&72\cos 2(i-2\omega) + 72\cos 4i - 2\omega - 80\cos 2(i-i_{3b}-2\omega)+\\
&120\cos 2(i_{3b}-2\omega) - 80\cos 2(i+i_{3b}-2\omega) + 20\cos 2(2i+i_{3b}-2\omega)-\\
&140\cos 2(i+2i_{3b}-2\omega) - 120\cos 4i_{3b} - 2\omega + 140\cos 4(i+i_{3b}) - 2\omega+\\
&544\cos 2(i-\omega) + 18\cos 4(i-\omega) - 80\cos 2(i-2i_{3b}-\omega)+\\
&832\cos 2(i-i_{3b}-\omega) + 35\cos 4(i-i_{3b}-\omega) - 1824\cos 2(i_{3b}-\omega)+\\
&210\cos 4(i_{3b}-\omega) + 832\cos 2(i+i_{3b}-\omega) + 35\cos 4(i+i_{3b}-\omega)+\\
&80\cos 2(2i+i_{3b}-\omega) - 80\cos 2(i+2i_{3b}-\omega) - 1232\cos 2\omega+\\
&108\cos 4\omega + 544\cos 2(i+\omega) + 18\cos 4(i+\omega) + 72\cos 2(2i+\omega)-\\
&80\cos 2(i-2i_{3b}+\omega) + 140\cos 2(2i-2i_{3b}+\omega) + 832\cos 2(i-i_{3b}+\omega)+\\
&35\cos 4(i-i_{3b}+\omega) + 80\cos 2(2i-i_{3b}+\omega) - 1824\cos 2(i_{3b}+\omega)+\\
&210\cos 4(i_{3b}+\omega) + 832\cos 2(i+i_{3b}+\omega) + 35\cos 4(i+i_{3b}+\omega)+\\
&80\cos 2(2i+i_{3b}+\omega) - 120\cos 2(2i_{3b}+\omega) - 80\cos 2(i+2i_{3b}+\omega)-\\
&72\cos 2(i+2\omega) - 140\cos 2(i-2i_{3b}+2\omega) - 80\cos 2(i-i_{3b}+2\omega)+\\
&120\cos 2(i_{3b}+2\omega) - 80\cos 2(i+i_{3b}+2\omega) + 20\cos 2(2i+i_{3b}+2\omega)+\\
&140\cos 4(i+i_{3b}) + 2\omega + 20\cos 4i - 2i_{3b} + 4\omega - 140\cos 2(i-2(i_{3b}+\omega))+\\
&80\cos 4i - 2(i_{3b}+\omega) - 140\cos 2(i+2(i_{3b}+\omega)) + 140\cos 4i - 2(2i_{3b}+\omega)+\\
&20\cos 4i - 2(i_{3b}+2\omega)-\\
&4\cos 2\omega_{3b}\Big(12\Big(43 + 9\cos 2i_{3b} + 4\cos 2i\Big(31 + 5\cos 2i_{3b}\Big)+\\
&5\cos 4i\Big(5 + 7\cos 2i_{3b}\Big)\Big) - 64\Big(59 + 25\cos 2i_{3b}+\\
&5\cos 2i\Big(5 + 7\cos 2i_{3b}\Big)\Big)\cos 2\omega\sin^2 i+\\
&160\Big(5 + 7\cos 2i_{3b}\Big)\cos 4\omega\sin^4 i\Big)\sin^2 i_{3b}\big]
\end{aligned}
\tag{A.8}
$$

$$
\begin{aligned}
&\frac{1}{2\pi}\int_0^{2\pi}(\beta^2+\xi^2)\xi^2 d\Omega = \frac{1}{32768}\Big[9156 + 1232\cos 2i + 108\cos 4i + 120\cos 2(i-2i_{3b}) + 120\cos 4(i-2i_{3b})+\\
&1824\cos 2(i-i_{3b}) + 210\cos 4(i-i_{3b}) + 1232\cos 2i_{3b} + 108\cos 4i_{3b} + 1824\cos 2(i+i_{3b})+\\
&210\cos 4(i+i_{3b}) + 120\cos 2(2i+i_{3b}) + 120\cos 2(i+2i_{3b}) - 72\cos 2(i-2\omega)+\\
&72\cos 4i - 2\omega - 80\cos 2(i-i_{3b}-2\omega) + 120\cos 2(i_{3b}-2\omega)-\\
&80\cos 2(i+i_{3b}-2\omega) + 20\cos 2(2i+i_{3b}-2\omega) - 140\cos 2(i+2i_{3b}-2\omega)-\\
&120\cos 4i_{3b} - 2\omega + 140\cos 4(i+i_{3b}) - 2\omega + 544\cos 2(i-\omega)+\\
&18\cos 4(i-\omega) - 80\cos 2(i-2i_{3b}-\omega) + 832\cos 2(i-i_{3b}-\omega)+\\
&35\cos 4(i-i_{3b}-\omega) - 1824\cos 2(i_{3b}-\omega) + 210\cos 4(i_{3b}-\omega)+\\
&832\cos 2(i+i_{3b}-\omega) + 35\cos 4(i+i_{3b}-\omega) + 80\cos 2(2i+i_{3b}-\omega)-\\
&80\cos 2(i+2i_{3b}-\omega) - 1232\cos 2\omega + 108\cos 4\omega + 544\cos 2(i+\omega)+\\
&18\cos 4(i+\omega) + 72\cos 2(2i+\omega) - 80\cos 2(i-2i_{3b}+\omega)+\\
&140\cos 2(2i-2i_{3b}+\omega) + 832\cos 2(i-i_{3b}+\omega)+\\
&35\cos 4(i-i_{3b}+\omega) + 80\cos 2(2i-i_{3b}+\omega) - 1824\cos 2(i_{3b}+\omega)+\\
&210\cos 4(i_{3b}+\omega) + 832\cos 2(i+i_{3b}+\omega)+\\
&35\cos 4(i+i_{3b}+\omega) + 80\cos 2(2i+i_{3b}+\omega) - 120\cos 2(2i_{3b}+\omega)-\\
&80\cos 2(i+2i_{3b}+\omega) - 72\cos 2(i+2\omega) - 140\cos 2(i-2i_{3b}+2\omega)-\\
&80\cos 2(i-i_{3b}+2\omega) + 120\cos 2(i_{3b}+2\omega) - 80\cos 2(i+i_{3b}+2\omega)+\\
&20\cos 2(2i+i_{3b}+2\omega) + 140\cos 4(i+i_{3b}) + 20\cos 4i - 2i_{3b} + 4\omega-\\
&140\cos 4(i+i_{3b}) + 20\cos 4i - 2i_{3b} + 4\omega - 140\cos 2(i-2(i_{3b}+\omega))+\\
&80\cos 4i - 2(i_{3b}+\omega) - 140\cos 2(i+2(i_{3b}+\omega))+\\
&140\cos 4i - 2(2i_{3b}+\omega) + 20\cos 4i - 2(i_{3b}+2\omega)+\\
&4\cos 2\omega_{3b}\big(12\big(43 + 9\cos 2i_{3b} + 4\cos 2i\big(31 + 5\cos 2i_{3b}+\\
&5\cos 4i\big(5+7\cos 2i_{3b}\big)\big)\big)-\\
&64\big(59 + 25\cos 2i_{3b} + 5\cos 2i\big(5+7\cos 2i_{3b}\big)\big)\cos 2\omega\sin i^2+\\
&160\big(5+7\cos 2i_{3b}\big)\cos 4\omega\sin i^4\big)\sin i_{3b}^2\Big]
\end{aligned}
\tag{A.9}
$$

$$
\begin{aligned}
&\frac{1}{2\pi}\int_0^{2\pi}\beta^2 d\Omega = \frac{1}{128}\Big(44 + 4\cos 2i + 6\cos 2(i-i3b) + 4\cos 2i3b + 6\cos 2(i+i3b)\\
&+ 2\cos 2(i-\omega) + 3\cos 2(i-i3b-\omega) - 6\cos 2(i3b-\omega) + 3\cos 2(i+i3b-\omega)\\
&- 4\cos 2\omega + 2\cos 2(i+\omega) + 3\cos 2(i-i3b+\omega) - 6\cos 2(i3b+\omega)\\
&+ 3\cos 2(i+i3b+\omega) - 8\cos 2\omega 3b\Big(1 + 3\cos 2i - 6\cos 2\omega\sin^2 i\Big)\sin^2 i3b\Big)
\end{aligned}
\tag{A.10}
$$

$$\begin{aligned}
&\frac{1}{2\pi}\int_0^{2\pi}\xi^2 d\Omega = \frac{1}{128}\biggl(44 + 4\cos 2i + 6\cos 2(i - i3b) + 4\cos 2i3b + 6\cos 2(i + i3b) \\
&+ 2\cos 2(i-\omega) + 3\cos 2(i - i3b - \omega) - 6\cos 2(i3b - \omega) + 3\cos 2(i + i3b - \omega) \\
&- 4\cos 2\omega + 2\cos 2(i+\omega) + 3\cos 2(i - i3b + \omega) - 6\cos 2(i3b + \omega) \\
&+ 3\cos 2(i + i3b + \omega) + 8\cos 2\omega 3b\Bigl(1 + 3\cos 2i - 6\cos 2\omega \sin^2 i\Bigr)\sin^2 i3b\biggr)
\end{aligned} \tag{A.11}$$

$$\begin{aligned}
&\frac{1}{2\pi}\int_0^{2\pi}(\alpha^2+\gamma^2)\alpha^2 d\Omega = \frac{1}{32768}\biggl(9156 + 1232\cos 2i + 108\cos 4i + 120\cos 2(i - 2i3b) + 120\cos 4i - 2i \\
&+ 1824\cos 2(i - i3b) + 210\cos 4(i - i3b) + 1232\cos 2i3b + 108\cos 4i3b + 1824\cos 2(i + i3b) \\
&+ 210\cos 4(i + i3b) + 120\cos 2(2i + i3b) + 120\cos 2(i + 2i3b) - 72\cos 2(i - 2\omega) \\
&- 72\cos 4i - 2\omega - 80\cos 2(i - i3b - 2\omega) + 120\cos 2(i3b - 2\omega) \\
&- 80\cos 2(i + i3b - 2\omega) + 20\cos 2(2i + i3b - 2\omega) - 140\cos 2(i + 2i3b - 2\omega) \\
&+ 120\cos 4i3b - 2\omega - 140\cos 4(i + i3b) - 2\omega - 544\cos 2(i - \omega) + 18\cos 4(i - \omega) \\
&+ 80\cos 2(i - 2i3b - \omega) - 832\cos 2(i - i3b - \omega) + 35\cos 4(i - i3b - \omega) \\
&+ 1824\cos 2(i3b - \omega) + 210\cos 4(i3b - \omega) - 832\cos 2(i + i3b - \omega) \\
&+ 35\cos 4(i + i3b - \omega) - 80\cos 2(2i + i3b - \omega) + 80\cos 2(i + 2i3b - \omega) \\
&+ 1232\cos 2\omega + 108\cos 4\omega - 544\cos 2(i + \omega) + 18\cos 4(i + \omega) \\
&- 72\cos 2(2i + \omega) + 80\cos 2(i - 2i3b + \omega) - 140\cos 2(2i - 2i3b + \omega) \\
&- 832\cos 2(i - i3b + \omega) + 35\cos 4(i - i3b + \omega) - 80\cos 2(2i - i3b + \omega) \\
&+ 1824\cos 2(i3b + \omega) + 210\cos 4(i3b + \omega) - 832\cos 2(i + i3b + \omega) \\
&+ 35\cos 4(i + i3b + \omega) - 80\cos 2(2i + i3b + \omega) + 120\cos 2(2i3b + \omega) \\
&+ 80\cos 2(i + 2i3b + \omega) - 72\cos 2(i + 2\omega) - 140\cos 2(i - 2i3b + 2\omega) \\
&- 80\cos 2(i - i3b + 2\omega) + 120\cos 2(i3b + 2\omega) - 80\cos 2(i + i3b + 2\omega) \\
&+ 20\cos 2(2i + i3b + 2\omega) - 140\cos 4(i + i3b) + 2\omega + 20\cos 4i - 2i3b + 4\omega \\
&- 140\cos 2(i - 2(i3b + \omega)) - 80\cos 4i - 2(i3b + \omega) - 140\cos 2(i + 2(i3b + \omega)) \\
&- 140\cos 4i - 2(2i3b + \omega) + 20\cos 4i - 2(i3b + 2\omega) \\
&+ 16\cos 2\omega 3b\Bigl(3(43 + 9\cos 2i3b + 4\cos 2i(31 + 5\cos 2i3b) \\
&+ 5\cos 4i(5 + 7\cos 2i3b)) + 16(59 + 25\cos 2i3b + 5\cos 2i(5 + 7\cos 2i3b))\cos 2\omega\sin^2 i \\
&+ 40(5 + 7\cos 2i3b)\cos 4\omega\sin^4 i\Bigr)\sin^2 i3b\biggr)
\end{aligned} \tag{A.12}$$

$$
\begin{split}
\frac{1}{2\pi}\int_0^{2\pi}(\alpha^2+\gamma^2)\gamma^2 d\Omega = \frac{1}{32768}\Big(&1232\cos 2i + 108\cos 4i + 120\cos 2(i-2i3b) + 120\cos 4i - 2i3b\\
&+ 1824\cos 2(i-i3b) + 210\cos 4(i-i3b) + 1232\cos 2i3b + 108\cos 4i3b + 1824\cos 2(i+i3b)\\
&+ 210\cos 4(i+i3b) + 120\cos 2(2i+i3b) + 120\cos 2(i+2i3b) - 72\cos 2(i-2\omega)\\
&- 72\cos 4i - 2\omega - 80\cos 2(i-i3b-2\omega) + 120\cos 2(i3b-2\omega)\\
&- 80\cos 2(i+i3b-2\omega) + 20\cos 2(2i+i3b-2\omega) - 140\cos 2(i+2i3b-2\omega)\\
&+ 120\cos 4i3b - 2\omega - 140\cos 4(i+i3b) - 2\omega - 544\cos 2(i-\omega) + 18\cos 4(i-\omega)\\
&+ 80\cos 2(i-2i3b-\omega) - 832\cos 2(i-i3b-\omega) + 35\cos 4(i-i3b-\omega)\\
&+ 1824\cos 2(i3b-\omega) + 210\cos 4(i3b-\omega) - 832\cos 2(i+i3b-\omega)\\
&+ 35\cos 4(i+i3b-\omega) - 80\cos 2(2i+i3b-\omega) + 80\cos 2(i+2i3b-\omega)\\
&+ 1232\cos 2\omega + 108\cos 4\omega - 544\cos 2(i+\omega) + 18\cos 4(i+\omega)\\
&- 72\cos 2(2i+\omega) + 80\cos 2(i-2i3b+\omega) - 140\cos 2(2i-2i3b+\omega)\\
&- 832\cos 2(i-i3b+\omega) + 35\cos 4(i-i3b+\omega) - 80\cos 2(2i-i3b+\omega)\\
&+ 1824\cos 2(i3b+\omega) + 210\cos 4(i3b+\omega) - 832\cos 2(i+i3b+\omega)\\
&+ 35\cos 4(i+i3b+\omega) - 16\cos 2\omega 3b(372\cos 2i + 75\cos 4i\\
&+ 3(9+20\cos 2i+35\cos 4i)\cos 2i3b + 16(59+25\cos 2i3b+5\cos 2i(5+7\cos 2i3b))\\
&\cdot \cos 2\omega\sin^2 i + 40(5+7\cos 2i3b)\cos 4\omega\sin^4 i)\sin^2 i3b\\
&- 4(-2289 + 35\cos 4i - 4i3b - 2\omega + 20\cos 2(2i+i3b+\omega)\\
&- 30\cos 2(2i3b+\omega) - 20\cos 2(i+2i3b+\omega) + 18\cos 2(i+2\omega)\\
&+ 35\cos 2(i-2i3b+2\omega) + 20\cos 2(i-i3b+2\omega) - 30\cos 2(i3b+2\omega)\\
&+ 20\cos 2(i+i3b+2\omega) - 5\cos 2(2i+i3b+2\omega) + 35\cos 4(i+i3b) + 2\omega\\
&- 5\cos 4i - 2i3b + 4\omega + 35\cos 2(i-2(i3b+\omega)) + 20\cos 4i - 2(i3b+\omega)\\
&+ 35\cos 2(i+2(i3b+\omega)) - 5\cos 4i - 2(2i3b+\omega) + 516\cos 2\omega 3b\sin i3b^2)\Big)
\end{split}
\tag{A.13}
$$

$$
\begin{split}
\frac{1}{2\pi}\int_0^{2\pi}\alpha^2 d\Omega = \frac{1}{128}\Big(&44 + 4\cos 2i + 6\cos 2(i-i3b) + 4\cos 2i3b + 6\cos 2(i+i3b)\\
&- 2\cos 2(i-\omega) - 3\cos 2(i-i3b-\omega) + 6\cos 2(i3b-\omega)\\
&- 3\cos 2(i+i3b-\omega) + 4\cos 2\omega - 2\cos 2(i+\omega)\\
&- 3\cos 2(i-i3b+\omega) + 6\cos 2(i3b+\omega) - 3\cos 2(i+i3b+\omega)\\
&+ 8\cos 2\omega 3b\Big(1 + 3\cos 2i + 6\cos 2\omega\sin^2 i\Big)\sin^2 i3b\Big)
\end{split}
\tag{A.14}
$$

$$
\begin{aligned}
&\frac{1}{2\pi}\int_0^{2\pi}\gamma^2 d\Omega = \frac{1}{128}\Big(44 + 4\cos 2i + 6\cos 2(i - i3b) + 4\cos 2i3b + 6\cos 2(i + i3b)\\
&- 2\cos 2(i - \omega) - 3\cos 2(i - i3b - \omega) + 6\cos 2(i3b - \omega)\\
&- 3\cos 2(i + i3b - \omega) + 4\cos 2\omega - 2\cos 2(i + \omega)\\
&- 3\cos 2(i - i3b + \omega) + 6\cos 2(i3b + \omega) - 3\cos 2(i + i3b + \omega)\\
&- 8\cos 2\omega 3b\Big(1 + 3\cos 2i + 6\cos 2\omega\sin^2 i\Big)\sin^2 i3b\Big)
\end{aligned}
\tag{A.15}
$$

$$
\begin{aligned}
&\frac{1}{2\pi}\int_0^{2\pi}\alpha^2\beta^2 d\Omega = \frac{1}{131072}\Big(19436 + 5872\cos 2i + 36\cos 4i + 40\cos 2(i - 2i3b) + 40\cos 4i - 2i3b\\
&+ 8800\cos 2(i - i3b) + 70\cos 4(i - i3b) + 5872\cos 2i3b + 36\cos 4i3b + 8800\cos 2(i + i3b)\\
&+ 70\cos 4(i + i3b) + 40\cos 2(2i + i3b) + 40\cos 2(i + 2i3b) + 72\cos 2(i - 2\omega)\\
&+ 80\cos 2(i - i3b - 2\omega) - 120\cos 2(i3b - 2\omega) + 80\cos 2(i + i3b - 2\omega)\\
&- 20\cos 2(2i + i3b - 2\omega) + 140\cos 2(i + 2i3b - 2\omega) - 18\cos 4(i - \omega)\\
&- 35\cos 4(i - i3b - \omega) - 210\cos 4(i3b - \omega) - 35\cos 4(i + i3b - \omega)\\
&- 108\cos 4\omega - 18\cos 4(i + \omega) - 35\cos 4(i - i3b + \omega)\\
&- 210\cos 4(i3b + \omega) - 35\cos 4(i + i3b + \omega) + 72\cos 2(i + 2\omega)\\
&+ 140\cos 2(i - 2i3b + 2\omega) + 80\cos 2(i - i3b + 2\omega) - 120\cos 2(i3b + 2\omega)\\
&+ 80\cos 2(i + i3b + 2\omega) - 20\cos 2(2i + i3b + 2\omega) - 20\cos 4i - 2i3b + 4\omega\\
&+ 140\cos 2(i - 2(i3b + \omega)) + 140\cos 2(i + 2(i3b + \omega))\\
&- 20\cos 4i - 2(i3b + 2\omega) + 32768\cos 2\omega\cos 2\omega 3b\sin^2 i\sin^2 i3b\\
&- 32\cos 4\omega 3b(9 + 20\cos 2i + 35\cos 4i - 280\cos 4\omega\sin^4 i)\sin^4 i3b\\
&+ 81920\cos i\cos i3b\sin^2 i\sin^2 i3b\sin 2\omega\sin 2\omega 3b\Big)
\end{aligned}
\tag{A.16}
$$

$$
\begin{aligned}
&\frac{1}{2\pi}\int_0^{2\pi}\alpha^2\xi^2 d\Omega = \frac{1}{65536}\Big(4578 + 616\cos 2i + 54\cos 4i + 60\cos 2(i - 2i3b) + 60\cos 4i - 2i3b\\
&+ 912\cos 2(i - i3b) + 105\cos 4(i - i3b) + 616\cos 2i3b + 54\cos 4i3b + 912\cos 2(i + i3b)\\
&+ 105\cos 4(i + i3b) + 60\cos 2(2i + i3b) + 60\cos 2(i + 2i3b) - 432\cos 4\omega\sin^4 i\\
&- 960\cos 2i3b\cos 4\omega\sin^4 i - 1680\cos 4i3b\cos 4\omega\sin^4 i\\
&+ 32\cos 2\omega 3b\Big(43 + 9\cos 2i3b + 4\cos 2i(31 + 5\cos 2i3b)\\
&+ 5\cos 4i(5 + 7\cos 2i3b) - 40(5 + 7\cos 2i3b)\cos 4\omega\sin^4 i\Big)\sin^2 i3b\\
&+ 16\cos 4\omega 3b\Big(9 + 20\cos 2i + 35\cos 4i - 280\cos 4\omega\sin^4 i\Big)\sin^4 i3b\Big)
\end{aligned}
\tag{A.17}
$$

$$
\begin{aligned}
\frac{1}{2\pi}\int_0^{2\pi} \alpha\beta\xi\gamma d\Omega = \frac{1}{131072}\Big(&36\cos 4i + 40\cos 2(i - 2i3b) + 40\cos 4i - 2i3b - 3488\cos 2(i - i3b) \\
&+ 70\cos 4(i - i3b) - 2320\cos 2i3b + 36\cos 4i3b - 3488\cos 2(i + i3b) + 70\cos 4(i + i3b) \\
&+ 40\cos 2(2i + i3b) + 40\cos 2(i + 2i3b) + 72\cos 2(i - 2\omega) + 80\cos 2(i - i3b - 2\omega) \\
&- 120\cos 2(i3b - 2\omega) + 80\cos 2(i + i3b - 2\omega) - 20\cos 2(2i + i3b - 2\omega) \\
&+ 140\cos 2(i + 2i3b - 2\omega) - 18\cos 4(i - \omega) - 35\cos 4(i - i3b - \omega) \\
&- 210\cos 4(i3b - \omega) - 35\cos 4(i + i3b - \omega) - 108\cos 4\omega - 18\cos 4(i + \omega) \\
&- 35\cos 4(i - i3b + \omega) - 210\cos 4(i3b + \omega) - 35\cos 4(i + i3b + \omega) \\
&+ 72\cos 2(i + 2\omega) - 20(257 - 7\cos 2(i - 2i3b + 2\omega) - 4\cos 2(i - i3b + 2\omega) \\
&+ 6\cos 2(i3b + 2\omega) - 4\cos 2(i + i3b + 2\omega) + \cos 2(2i + i3b + 2\omega) \\
&+ \cos 4i - 2i3b + 4\omega - 7\cos 2(i - 2(i3b + \omega)) - 7\cos 2(i + 2(i3b + \omega)) \\
&+ \cos 4i - 2(i3b + 2\omega)) - 288\cos 4\omega 3b \sin^4 i3b \\
&+ 80(-29\cos 2i - 2\cos 4\omega 3b(4\cos 2i + 7(\cos 4i - 8\cos 4\omega \sin^4 i))\sin^4 i3b)\Big)
\end{aligned}
\tag{A.18}
$$

$$
\begin{aligned}
\frac{1}{2\pi}\int_0^{2\pi} \gamma^2\beta^2 d\Omega = \frac{1}{65536}\Big(&4578 + 616\cos 2i + 54\cos 4i + 60\cos 2(i - 2i3b) + 60\cos 4i - 2i3b \\
&+ 912\cos 2(i - i3b) + 105\cos 4(i - i3b) + 616\cos 2i3b + 54\cos 4i3b + 912\cos 2(i + i3b) \\
&+ 105\cos 4(i + i3b) + 60\cos 2(2i + i3b) + 60\cos 2(i + 2i3b) - 432\cos 4\omega \sin^4 i \\
&- 960\cos 2i3b\cos 4\omega \sin^4 i - 1680\cos 4i3b\cos 4\omega\sin^4 i \\
&- 32\cos 2\omega 3b\Big(43 + 9\cos 2i3b + 4\cos 2i(31 + 5\cos 2i3b) \\
&+ 5\cos 4i(5 + 7\cos 2i3b) - 40(5 + 7\cos 2i3b)\cos 4\omega\sin^4 i\Big)\sin^2 i3b \\
&+ 16\cos 4\omega 3b\Big(9 + 20\cos 2i + 35\cos 4i - 280\cos 4\omega \sin^4 i\Big)\sin^4 i3b\Big)
\end{aligned}
\tag{A.19}
$$

$$
\begin{aligned}
\frac{1}{2\pi}\int_0^{2\pi}\gamma^2\xi^2 d\Omega = \frac{1}{131072}\Big(&19436 + 5872\cos 2i + 36\cos 4i + 40\cos 2(i - 2i3b) + 40\cos 4i - 2i3b \\
&+ 8800\cos 2(i - i3b) + 70\cos 4(i - i3b) + 5872\cos 2i3b + 36\cos 4i3b + 8800\cos 2(i + i3b) \\
&+ 70\cos 4(i + i3b) + 40\cos 2(2i + i3b) + 40\cos 2(i + 2i3b) + 72\cos 2(i - 2\omega) \\
&+ 80\cos 2(i - i3b - 2\omega) - 120\cos 2(i3b - 2\omega) + 80\cos 2(i + i3b - 2\omega) \\
&- 20\cos 2(2i + i3b - 2\omega) + 140\cos 2(i + 2i3b - 2\omega) - 18\cos 4(i - \omega) \\
&- 35\cos 4(i - i3b - \omega) - 210\cos 4(i3b - \omega) - 35\cos 4(i + i3b - \omega) \\
&- 108\cos 4\omega - 18\cos 4(i + \omega) - 35\cos 4(i - i3b + \omega) \\
&- 210\cos 4(i3b + \omega) - 35\cos 4(i + i3b + \omega) + 72\cos 2(i + 2\omega) \\
&+ 140\cos 2(i - 2i3b + 2\omega) + 80\cos 2(i - i3b + 2\omega) - 120\cos 2(i3b + 2\omega) \\
&+ 80\cos 2(i + i3b + 2\omega) - 20\cos 2(2i + i3b + 2\omega) - 20\cos 4i - 2i3b + 4\omega \\
&+ 140\cos 2(i - 2(i3b + \omega)) + 140\cos 2(i + 2(i3b + \omega)) \\
&- 20\cos 4i - 2(i3b + 2\omega) - 32768\cos 2\omega\cos 2\omega 3b\sin^2 i\sin^2 i3b \\
&- 32\cos 4\omega 3b\Big(9 + 20\cos 2i + 35\cos 4i - 280\cos 4\omega\sin^4 i\Big)\sin^4 i3b \\
&- 81920\cos i\cos i3b\sin^2 i\sin^2 i3b\sin 2\omega\sin 2\omega 3b\Big)
\end{aligned}
\tag{A.20}
$$

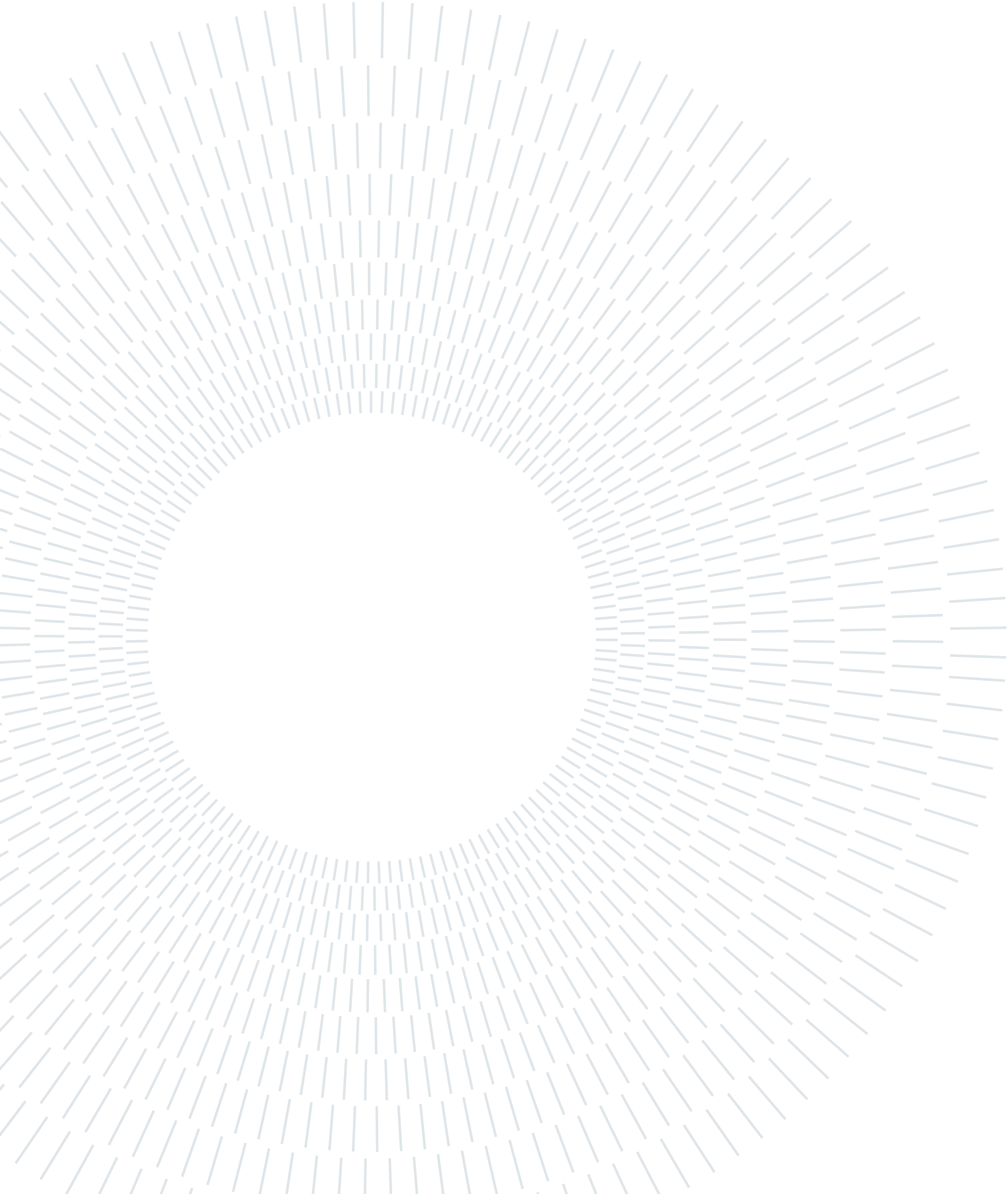

B | Acknowledgements

Prima di tutto, desidero ringraziare la Professoressa Camilla Colombo, sia per il suo ruolo di insegnante, capace di stimolare la curiosità e l'operatività dei suoi studenti, sia come relatrice, per avermi guidato in questo percorso. Vorrei anche esprimere la mia gratitudine a Xiaodong Lu per i suoi preziosi suggerimenti e consigli.

Un grazie speciale va alla mia famiglia, mio fratello Luca e i miei genitori, Luciene e Simone, che mi hanno sostenuto fino a questo traguardo, supportandomi in ogni mia scelta. Grazie per aver sempre avuto fiducia in me. Spero che questo sia un traguardo anche per voi.

Em particular, gostaria de agradecer à minha mãe: obrigado por todos os esforços que fizeste por mim quando estávamos sozinhos e por todo o resto do meu caminho até hoje. Se sou o homem que sou, devo isso a ti. Não poderia desejar uma mãe melhor.

Ringrazio la seconda famiglia, quella del Martinitt che mi ha accolto a Milano, nessuno escluso. Si può dire sia stata una scuola di vita. Ce lo siamo goduti quel campus. Menzione speciale a Mimmo, sulla cui presenza si può sempre contare.

Alla macha gang, presenti e passati, grazie per le discussioni e per i sorrisi scambiati insieme.

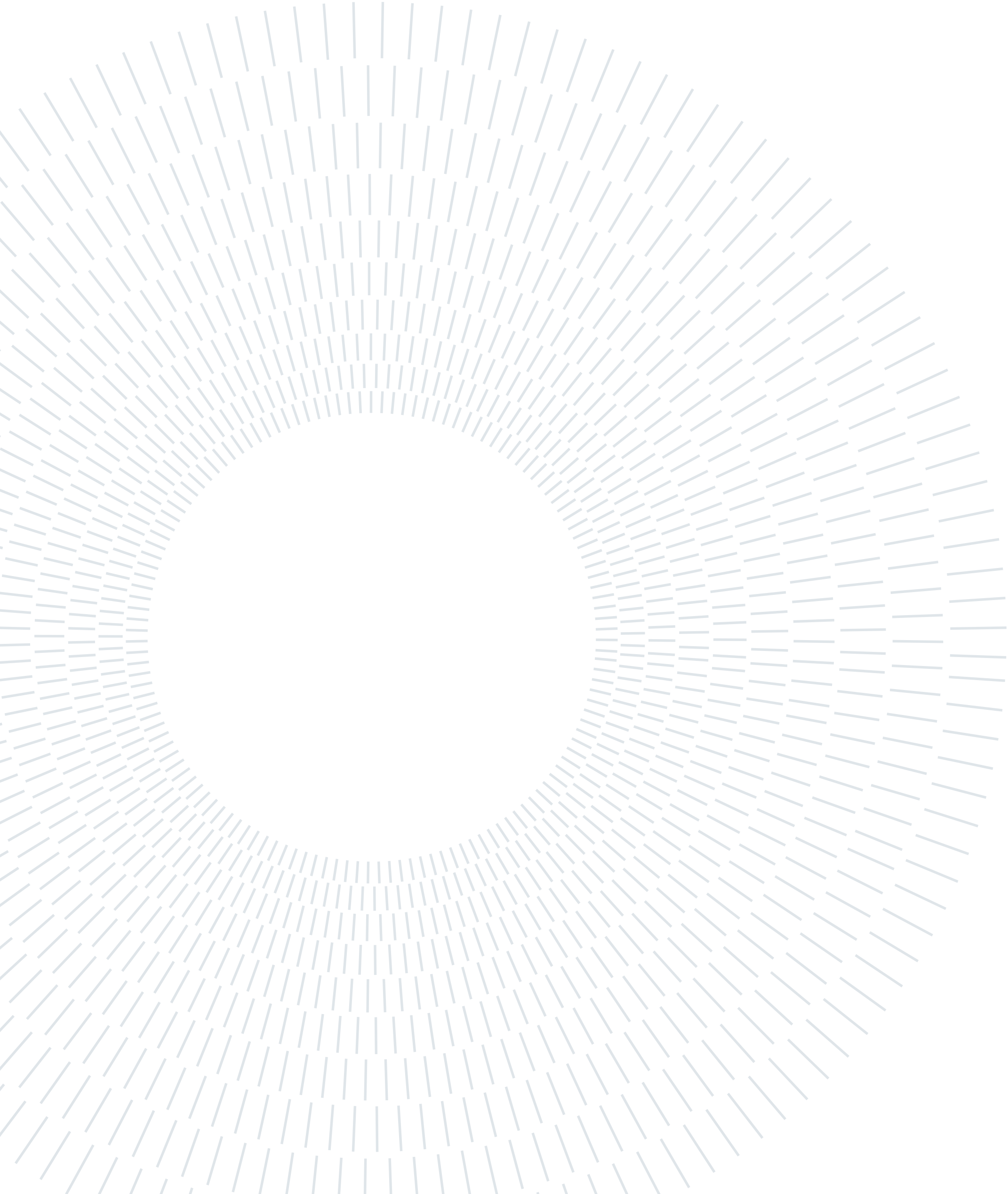E in ultimo desidero ringraziare Claudia, per avermi incoraggiato e spronato a migliorare. Per avermi dato la spinta che mi serviva per arrivare fino a qui. Grazie della tua presenza al mio fianco, nei momenti di gioia e in quelli di sconforto, e di avermi sorretto in questi ultimi. Grazie per il tuo amore.